8-9-2014

GAS-PHASE, CATALYTIC HYDRODEOXYGENATION OF PROPANOIC ACID OVER SUPPORTED GROUP VIII NOBLE METALS

Yuliana K. Lugo José
University of South Carolina - Columbia

GAS-PHASE, CATALYTIC HYDRODEOXYGENATION OF PROPANOIC ACID OVER SUPPORTED GROUP VIII NOBLE METALS

by

Yuliana K. Lugo José

Bachelor of Science
University of Puerto Rico at Mayaguez, 2008

Submitted in Partial Fulfillment of the Requirements

For the Degree of Doctor of Philosophy in

Chemical Engineering

College of Engineering and Computing

University of South Carolina

2014

Accepted by:

Christopher T. Williams, Major Professor

John Monnier, Committee Member

Andreas Heyden, Committee Member

Donna Chen, Committee Member

Francis Gadala Maria, Committee Member

John W. Weidner, Committee Member

Lacy Ford, Vice Provost and Dean of Graduate Studies

DEDICATION

This work is dedicated to my father Ramón R. Lugo Bretón (1957-2014), may his soul rest in peace for all eternity. I thank my father for all his advice, his wisdom and love he gave to all of us. It is dedicated to a man with integrity, passionate about the world he lived in, who fought intensely the battle of cancer until the end. I thank him for keeping me strong and advising me to continue my PhD studies despite his sickness. I love you dad, till we meet again…

ACKNOWLEDGEMENTS

First and foremost, I want to thank my GOD for giving me strength, knowledge, hope and health to continue to achieve my dreams despite all the difficulties. I want to thank my family, especially my father, Ramón Lugo Bretón, my mother, Sonia José de Lugo, my sister, Yadhira Lugo José and my boyfriend, Raúl C. Alvarado, I love them with all my heart. I wanted to thank them for giving me strength to keep going despite the distance that separate us. I wish to give special acknowledgment to my advisor Dr. Christopher T. Williams, for all his great advice, patient and understanding. I will always appreciate his confidence and trust he gave to me. Additionally, my most sincere gratitude to Dr. John Monnier for the countless hours of teaching and intensive coach, to ensure that I ended a respected scientist. Thank you for facilitating me the use of the reactor equipment and helping me design the new reactor. I wish to thank Dr. Andreas Heyden, for all the good collaboration to ensure high-quality research. His enthusiasm and dedication toward our research field deserves all the respect.

Thanks to my Ph.D advisory committee: Dr Donna Chen, Dr. Francis Gadala Maria and Dr. John W. Weidner for all the guidance and precious time to successfully complete my Ph.D. Moreover, I wish to thank the financial support provided to me during my PhD studies from the National Science Foundation (NSF) grant number CHE-1153012, the Alfred P. Sloan Foundation Program from National Action Council for Minorities in

Engineering (NACME), Inc., and the Southeastern Alliance for Graduate Education and the Professoriate (SEAGEP).

My honest appreciation to the chemical engineering department staff including: Marcia Rowen, Loretta L. Hardcastle, Vernon Dorrell, Kay P. Dorrell and Brian Loggans, for always having a smile and assisting me gracefully. Special thanks to Carol Stork for helping me with the reactor troubleshooting and always be there when I needed counseling. Special thanks to Sandra Knotts for her patience in working with me with the reactor's administrative issues. Thanks to Dr. John R. Regalbuto for their helpful and insightful conversations.

Finally, I want to express my gratitude to my dear friends and colleagues in the department and outside including: Sina Behtash, Saeed Abbaspour, Irmydel Lugo, Veronica Rodriguez, Aixa del Valle, Abraham Rodriguez, Artem Vityuk, You Jung, and John Tengco. Thanks for all the sincere friendship and guidance during my PhD proces

ABSTRACT

Recent advances for the deoxygenation of biomass, have demonstrated that hydrodeoxygenation (HDO) is one of the most promising route for the upgrading pyrolysis bio-oils. Catalytic hydrodeoxygenation of pyrolysis bio-oil have shown to be an efficient and economical process, since the raw materials consist mainly of waste. Propanoic Acid (PAc) is considered as one of the main constituents of pyrolysis bio-oils. However, these carboxylic acids are extremely corrosive and difficult to deoxygenate. Therefore, much effort have been given to the development of novel catalytic techniques, to improve the activity, stability and selectivity for the HDO of carboxylic acids.

This dissertation explores the use of supported group VIII noble metals for the HDO of PAc. The reactions were evaluated in a conventional continuous plug-flow reactor operated between 200-400ºC under atmospheric pressure with concentrations of 1.2% PAc/20%H_2/balance He. The first part of this work consisted on the synthesis, characterization and evaluation of SiO_2 supported catalysts (M = Pd, Pt, Rh, Ru, Ni). The activity and kinetics involving the reaction rate orders with respect to PAc and H_2 and activation energies were discussed in detail. The reaction activity based on the TOF follows the sequence: Pd > Ru > Pt > Rh > Ni. The reaction over Pd, Pt and Rh catalysts proceeds mainly via decarbonylation (DCN) and decarboxylation (DCX) pathways at each reaction temperature. For Ru and Ni catalysts, while decarbonylation and decarboxylation pathway

were predominant at lower temperatures (e.g., 200-250ºC), at higher temperatures (>300 ºC) the formation of diethyl ketone was observed. Additionally, the kinetics of Pd over different supports (carbon, SiO_2 and TiO_2) were examined. The activity based on the TOF decreases in the following order: Pd/SiO_2 > Pd/TiO_2 > Pd/C. The reaction orders in acid and H_2 were found to be approximately 0.5 and zero, respectively, regardless of the support. The apparent activation energies studied in a temperature range of 200-240 ºC, were 16.7 ± 0.6, 19.3 ± 1.6 and 11.7 ± 0.7 kcal/mole for Pd/C, Pd/TiO_2 and Pd/SiO_2 catalysts, respectively.

Secondly, the effects of metal nanoparticle size ranging between 1.9 to 12.4 nm for over Pd/SiO_2 under differential conversion catalysts was investigated. The particle sizes were determined by chemisorption (O_2-H_2 titration), XRD and STEM. While the catalytic TOF remained constant between 3.0-12.4 nm it decreased by a factor of 2-3 with decreasing particle size down to 1.9 nm. The reaction rate is therefore considered to be largely structure-insensitive over the range studied. The reaction rate orders with respect to PAc (~0.5) and H_2 (~0), and the apparent activation energy (~12 Kcal/mole), were found to be the same for both 2.0 and 12.4 nm particle sizes. In contrast, the reaction rate order with respect to PAc (~1.0) and H_2 (~0.3) was different for hydrogenation to produce EtCHO. These differences are explained by a change in the rate-determining step for the HDO of propanoic acid.

Furthermore, a deuterium isotopic substitution of PAc to study a kinetic isotope effect (KIE) and elucidate the reaction mechanism was explored. A combined experimental and computational kinetic isotope effect (KIE) study was performed for the catalytic hydrodeoxygenation (HDO) of deuterium-labeled propanoic acid (PAc-2, 2-D2) over Pd

catalyst. For the experimental study, the kinetics were measured in a plug flow reactor over a 5 wt% Pd/C catalyst (as described in the first part) under differential conversion. Different experimental KIE values for the high ($k_H/k_D = 1.16 \pm 0.07$) and low ($k_H/k_D = 1.62 \pm 0.05$) partial pressures of hydrogen were observed. Density functional theory calculations were performed to obtain the reaction parameters of the elementary steps involved in the HDO of PAc on Pd (111), and a microkinetic model was developed to estimate the KIE for the low hydrogen partial pressure case from first principles. The computed result (k_H/k_D = 1.49) is in good agreement with the experiment. In addition, the product distribution showed to be C_2H_6 and CO suggesting decarbonylation (DCN) is the main reaction pathway. Strong evidence is provided for the proposed mechanism for the formation of C_2H_6 on Pd(111).

The catalytic activity and selectivity trend over carbon supported over group VIII noble metals (M = Pt, Rh, Ru, Ir, Ni, Ag, Au and Cu) was also explored. The catalysts exhibited mainly selectivity toward methane and C2 hydrocarbons, showing strong overall preference for decarbonylation (DCN) versus hydrogenation. The catalytic activity at 200ºC in terms of TOF decreased in the sequence Rh≥ Pt > Ir > ~Ru ~Ni, with no measurable activity found for Au, Ag, and Cu. A reaction rate order of ~0.5 and 0 with respect to PAc and H_2, respectively, was found for all catalyst, except Ni/C. The latter exhibited a reaction rate order roughly of 0.2 and -0.2 with respect to PAc and H_2, respectively. Comparison with previous studies on the HDO of PAc over 5wt% Pd/C is reported.

TABLE OF CONTENTS

DEDICATION iii

ACKNOWLEDGEMENTS iv

ABSTRACT vi

LIST OF TABLES xi

LIST OF FIGURES xiv

LIST OF ABBREVIATIONS xix

CHAPTER 1 INTRODUCTION 1

1.1 OVERVIEW 1

1.2 BACKGROUND AND CURRENT STATE OF KNOWLEDGE 4

CHAPTER 2 EXPERIMENTAL TECHNIQUES 29

2.1 LIST OF CHEMICAL MATERIALS 29

2.2 CATALYST PREPARATION 32

2.3 CATALYST CHARACTERIZATION 38

2.4 CATALYST EVALUATION 51

CHAPTER 3 GAS-PHASE, CATALYTIC HYDRODEOXYGENATION OF PROPANOIC ACID, OVER SUPPORTED GROUP VIII NOBLE METALS: METAL AND SUPPORT EFFECTS 57

3.1 INTRODUCTION 57

3.2 EXPERIMENTAL METHODS 59

3.3 RESULTS AND DISCUSSION 62

3.4 CONCLUSION 83

CHAPTER 4 HYDRODEOXYGENATION OF PROPANOIC ACID, OVER SUPPORTED PALLADIUM CATALYST: EFFECT OF PD PARTICLE SIZE 84

4.1 INTRODUCTION 84

4.2 EXPERIMENTAL METHODS 86

4.3 Results and Discussion 89

4.4 Conclusion 101

Chapter 5 Unraveling the Mechanism of Propanoic Acid Hydrodeoxygenation Using Deuterium Kinetic Isotope Effects 103

5.1 Introduction 103

5.2 Experimental Methods 105

5.3 Results and Discussion 107

5.4 Conclusion 116

Chapter 6 Gas-Phase, Catalytic Hydrodeoxygenation of Propanoic Acid, Over Carbon Supported Transition State Metals: Metal Activity And Selectivity Trends 118

6.1 Introduction 118

6.2 Experimental Methods 119

6.3 Results and Discussion 122

6.4 Conclusion 131

Chapter 7 Conclusion and Proposed Future Work 132

7.1 Conclusion 132

7.2 Proposed future work 135

References 137

Appendix A: Supplementary information for chapter 2 154

Appendix B: Supplementary information for chapter 3 160

Appendix C: Supplementary information for chapter 4 164

Appendix D: Supplementary information for chapter 5 171

Appendix E: Reactor design and set-up 180

LIST OF TABLES

Table 1.1: Atomic composition of common biomass feedstock and fuels. 7

Table 1.2: Comparison of the chemical composition between the conventional oil and bio-oil. 9

Table 1.3: Properties of bio-Oils and upgraded bio-oils. 11

Table 2.1: Liquid chemicals utilized for the HDO of PAc. a n-propyl propionate purchased from Sigma- Aldrich 29

Table 2.2: Gases utilized for the HDO of PAca14 liter disposable (Matheson Tri-gas). . 30

Table 2.3: Commercial and provided catalyst tested. 30

Table 2.4: List of type of support and the physical properties (γ-Al_2O_3 powder and carbon were tested with BET). 31

Table 2.5: Precursors (salts) utilized for the catalyst screening (soluble in water except, Pd (II) chloride (PdCl2) which is soluble in dilute mineral acids, aqueous metal halides. Additional metal complexes for strong electrostatic adsorption are summarized in chapter 3 (section 3.2) 31

Table 2.6: Calcination and reduction temperature of the synthesized catalyst. a catalyst reduced in the TPR. b correspond to nitrate hydrate and chloride based metal salts. All catalysts were cooled down in a He flow. 34

Table 2.7: Stoichiometry factors for the chemisorption methods analyzed. 41

Table 2.8: Catalyst analyzed by chemisorption and the dispersion and physical properties. 42

Table 3.1: Physical and chemical properties of M/SiO_2.*Pd/SiO_2 synthesized by SEA. . 60

Table 3.2: Kinetic data for the screened catalysts in the HDO of PAc at 200 ºC and 1 atm. ~1.0 % PAc, 20% H2/He, catalyst mass 100-300 mg , total flow 50 sccm. Pd* was measured at a total flow 200 sccm. 72

Table 3.3: Kinetic data for the HDO of PAc over supported Pd catalyst. Reaction conditions: 200 ºC and 1 atm, XPAc = 0.01, 20% H_2/balance He, catalyst weight: Pd/C - 200 mg, Pd/SiO_2 and Pd/TiO_2 – 100 mg..... 76

Table 4.1: Physical properties of support SiO_2 Aerosil heat treatment. 86

Table 4.2: Physical properties of Pd/SiO_2 a Determined by chemisorption, O_2-H_2 titration. [b] Catalysts were reduced in-situ at 350ºC, for 2 hours at 5ºC/min, unless otherwise noted. [b] TEM results in parenthesis indicate the particle size obtained after the reaction..... 87

Table 4.2: Kinetic data for the screened catalysts in the HDO of PAc at 200 ºC and 1 atm. ~1.0 % PAc, 20% H2/He, catalyst mass 200 mg , total flow 200 sccm. Van Hardeveld and Hartog statistics on Pd(111) and Pd(100) fraction for the Pd, f.c.c Cubo-Octahedron-corners truncated at (100). 96

Table 5.1: Deuterium isotope effect for PAc HDO over 5wt% Pd/C, 16.9%, 6.8nm. Reaction conditions: 200ºC and 1 atm, Total flow: 50 sccm. <5% conversion, 100% selectivity C_2H_6. a Rxn rate - μmol/min·gcat. Rxn 1- CH_3CH_2COOH/H_2, Rxn 2= CH_3CD_2COOH/H_2. 109

Table 5.2: Comparison of KIE values based on experimental, calculated and theoretical approach. * based on the Upper Limit for the Primary Kinetic Isotope Effect calculations. 114

Table 5.3: Distribution of CH_3CH_2D and CH_3CH_3 during the HDO of labeled PAc a using the m/e = 31 intensity, the other two m/e intenstities arising from CH_3CH_2D were calculated using the published fragmentation pattern of Amenomiya and Pottie. 116

Table 6.1: Physical and chemical properties of M/carbon. [a] Dispersion and particle size obtained by chemisorption (O_2-H_2 titration). – dispersion and particle size not obtained. 121

Table 6.2: Reaction rate conditions observed at 200ºC and 1 atm pressure. Conversions and preferred reaction pathways are (1-2%) and DCN, respectively, for all catalysts. Reaction conditions: 1.2% PAc, 20% H_2/balance He. Total flow = 50sccm. Au, Ag and Cu showed no activity at 200ºC..... 129

Table A.1: Calibration parameters (retention time and response factor) based on the FID and TCD columns. 159

Table B.1: Methanation over Ru/SiO_2. 1% CO, 20% H_2, balance Helium. Total flow = 50 sccm, 1 atm pressure. 163

Table B.2: Methanation over Ni/SiO_2. 1% CO, 20% H_2, balance Helium. Total flow = 50 sccm, 1 atm pressure. 163

Table C.1: Comparison of particle size Pd/SiO_2 over three different methods. b and a denotes before and after the reaction. 169

Table D.1: Fragmentation pattern comparison between experimental and theoretical, taking as reference the published work from Amenominya and Pottier. 173

Table E.1: Cost of reactor's equipment 185

LIST OF FIGURES

Figure 1.1: Schematic of biomass processing cycle. 2

Figure 1.2: Hydrodeoxygenation of the basic building block of biomass to renewable hydrocarbon fuels..... 7

Figure 1.3: Plot of maximum selectivity as a function of increasing (not on scale) metal–oxygen bond strength. Above each bar is given the temperature (ºC) at which this selectivity is reached. 21

Figure 1.4: Reaction mechanism for the ketonization of acetic acid. 22

Figure 1.5: Schematic representation of reaction steps in the selective hydrogenation of carboxylic acid to the corresponding aldehyde. 24

Figure 1.6: Structure of metal carboxylates according to the type of metal–ligand interaction. (I) Ionic or uncoordinated form, (II) unidentate coordination, (III) bidentate chelating coordination, (IV) bidentate bridging coordination. 27

Figure 1.7: Surface decomposition on Pd catalyst of α-β-carbon. 28

Figure 1.8: Proposed elementary mechanism for the HYS of acetic acid to ethanol over Pd(111), based on DFT-calculated overall surface reaction energies. 28

Figure 2.1: Procedure for the preparation of catalyst by incipient and wet impregnation method..... 33

Figure 2.2: Example of a mechanism for Pt amine complexes electrostatic adsorption[87].36

Figure 2.3: pH shift survey for 2.3wt% Pd/TiO_2. 36

Figure 2.4: Uptake survey for 4wt% Pd/SiO_2. 37

Figure 2.5: Uptake survey for 2.3wt% Pd/TiO_2. 37

Figure 2.6: Pulse chemisorption adsorbed peak as a function of the injection number.... 39

Figure 2.7: Hydrogen spillover over supported Mx..... 40

Figure 2.8: Experimental setup for the FT-IR spectroscopy of PAc over Pd/SiO_2 and SiO_2. 48

Figure 2.9: Diagram of programmed pulsed of PAc and He. 49

Figure 2.10: USC Antoine's estimation for the concentration of propanoic acid in the reaction system..... 54

Figure 2.11: Schematic of the gas-phase plug-flow reactor system coupled with a GC system and a residual gas analyzer. 54

Figure 2.12: Picture of the continuous plug-flow reactor system. 55

Figure 2.13: Programmed temperature ramp for the gas chromatography. 56

Figure 3.1: Conversion and selectivity for a) Silica Star and b) Aerosil 300 SiO_2 supports; c) 1.1wt% Pd/Silica Star and d) 4.0wt% Pd/Aerosil 300. C2 denotes the sum of ethylene and ethane. EtCHO and DEK refer to propionaldehyde and diethyl ketone, respectively. Mass of catalyst (100-300 mg); feed composition 1% PAc, 20% H_2, balance He. Total flow rates for 1.1wt% and 4wt% Pd/SiO_2 were 50 and 200 sccm, respectively..... 66

Figure 3.2: Conversion and selectivity for a) Pt and b) Rh supported on SiO2 Star. C2 and C3 denote ethane and propane, respectively. Mass of catalyst (200-300 mg); feed composition 1% PAc, 20% H_2, balance He; total flow rate 50 sccm. 68

Figure 3.3: Conversion and selectivity for a) Ru and b) Ni over SiO_2 Star. C2 denotes as the sum of ethylene and ethane C3 denote as propane. EtCHO and DEK denote propionaldehyde and diethyl-ketone respectively. Mass of catalyst (200-300 mg); feed composition 1% PAc, 20% H_2, balance He; total flow rate 50 sccm. 70

Figure 3.4: Conversion and selectivity for a) carbon and b) TiO_2. C2 denotes as the sum of ethylene and ethane. DEK denote as diethyl-ketone. Mass of catalyst (200-300 mg); feed composition 1% PAc, 20% H_2, balance He; total flow rate 50 sccm. 73

Figure 3.5: Conversion and selectivity for a) Pd/C and b) Pd/TiO_2. C2 denotes as the sum of ethylene and ethane. Ester denotes as propyl-propionate. Mass of catalyst (100-200 mg); feed composition 1% PAc, 20% H_2, balance He; total flow rate 50 sccm. 75

Scheme 3.1: Illustration of plausible reaction pathways for the HDO of PAc over Pd over SiO_2, C and TiO_2. 78

Figure 3.6: Power rate law for the kinetic dependencies of PAc and H_2 for PAc conversion at 200 ºC and 1 atm pressure. (■) 4.0wt% Pd/Aerosil 300, (♦) 2.3wt% Pd/TiO_2, (▲) 5wt% Pd/C, reactor conditions: 20% H_2/balance, total flow: Pd/C - 50 sccm, Pd/SiO_2- 200 sccm, Pd/TiO_2 - 150 sccm. For hydrogen kinetics ~ 1.0% PAc balances He. 80

Figure 4.1: Histogram showing the particle size distribution of Pd-2 (2nm A-B before and after reaction), Pd-6 (C-3.8nm before and D-3.8nm after reaction, 1% of particles around 20nm) and Pd-10 (E-12.4 nm before and F-12.4nm after reaction, 2-4% particle around 30nm). 93

Scheme 4.1: Reaction pathway for the decarbonylation/hydrogenation of PAc over Pd/SiO_2. 94

Figure 4.2: TOF_{C2H6} (squares) and TOF_{EtCHO} (diamonds) as a function of particle size for the series of Pd/SiO_2 catalysts for the HDO of PAc at 200 ºC and 1 atm.Reactor conditions: ~1.0 % PAc, 20% H_2/He, catalyst mass 200 mg , total flow 200 sccm. The solid lines are the least squares fits of the data. See text for details. 98

Figure 4.3: Power rate law dependencies of TOF_{C2H6} (squares) and TOF_{EtCHO} (diamonds) on PAc (filled symbols) and H_2 (open symbols) at 200 ºC and 1 atm total pressure for Pd-2-2nm (red symbols) and Pd-10-12.4nm (black symbols).Reactor conditions: 20% H_2/balance, total flow 200 sccm. For hydrogen kinetics ~ 1.0% PAc balanced with He. 100

Figure 4.4: Arrhenius plots based on the total TOF of Pd-10 (12.4nm).Reactor conditions: 1 atm total pressure, ~ 1.0% Pac, 20% H_2, balanced He, total flow 200 sccm. 101

Figure 5.1: Steady-state measurements for the reaction rate of the labeled/unlabeled PAc HDO.~1.2% PAc, 20% H_2/balance He. C-H and C-D denotes unlabeled and labeled reaction rate, respectively. 110

Figure 5.2: Steady-state measurements for the reaction rate of the labeled/unlabeled PAc HDO.~1.2% PAc, 5% H_2/balance He. C-H and C-D denotes unlabeled and labeled reaction rate, respectively. 111

Figure 6.1: Conversion of PAc based on product formed (%) as a function of temperature. Reaction conditions: 1.2% PAc, 20% H_2/balance He. Total flow = 50sccm. 123

Figure 6.2: Product distribution of all catalysts between 200-400ºC. C1 denotes methane, C2 denotes ethylene and ethane, C3 denotes propane and EtCHO denotes propionaldehyde..... 127

Figure 6.3: Reaction rate order with respect to PAc(black symbols) and H2(red symbols) for: (▲)Pd, (*)Pt, (●)Rh, (♦)Ru, Ni(◊) and (■)Ir. Reaction conditions: 200ºC and 1atm, total flow = 50 sccm. Mass catalyst = 0.20g. 131

Figure A.1: FTIR adsorption for 1.86wt% Pd/SiO_2, 0.10% PAc, 20% Hydrogen, balance Helium Total flow rate = 50 sccm. 155

Figure A.2: FTIR adsorption for SiO2, 0.10% PAc, 20% Hydrogen, balance Helium Total flow rate = 50 sccm. 155

Figure A.3: Calibration curves for PAc, EtCHO, 1-propanol, DEK, ethane, methane, CO2 and CO. 158

Figure B.1: Ni/SiO_2 2p XPS spectra as received and pre-treated, 100% H_2 for 2 hours up to 400 ºC. 161

Figure B.2: TPR spectra for 1.6 wt% Ru, and 1.8 wt% Ni over SiO_2 (mass = 0.10 g) 1% H_2/Ar, total flow = 50 sccm, at 5 ºC /min. 162

Figure C.1: TOF vs. different mesh sizes of 4wt% Pd/SiO_2 (♦ Pd-2) and 1.9wt% Pd/SiO_2 (■ Pd-6) for HDO of PAc at 200 ºC and 1 atm. ~1.0 % PAc, 20% H2/He, catalyst mass 200 mg , total flow 200 sccm, (20-120 mesh sizes)..... 165

Figure C.2: Reaction rate vs. flow rate (sscm) for 4wt% Pd/SiO_2..... 166

Figure C.3: Reaction rate vs. flow rate (sscm) for 5wt% Pd/C..... 166

Figure C.4: Reaction rate vs. flow rate (sscm) for 2.3wt% Pd/TiO_2. 167

Figure C.4: X-ray diffraction pattern for Pd/SiO_2, before: Pd-2 (a), Pd-6 (b), Pd-10 (c), and after the reaction: Pd-2 (d), Pd-6 (e) and Pd-10 (f).
* Steel slide (background holder). 170

Figure D.1: Mass spectrometer for C_2H_6 rel. intensities..... 172

Figure D.2: Relative intensities for mass: 29,30 and 31 for the labeled PAc reaction. Using Argon as background. Ptotal = 4.0E-06. 173

Figure D.3: Network of elementary reaction steps considered in the hydrodeoxygenation of PAc over Pd (111). Elementary reactions involved in the DCX mechanism are shown with blue color arrows, DCN reactions are illustrated with red color arrows, and those reactions involved in both mechanisms such as dehydrogenation reactions and removal of the hydrocarbon pool are shown with gray color arrows..... 179

Figure E.1: blueprint of temperature controller box. 183

Figure E.2: Enclosed hood assembly..... 184

List of Abbreviations

AAc ..... Acetic acid

AAS ..... Atomic Absorption Spectroscopy

BET ..... Brunauer–Emmett–Teller

BOE ..... Barrel of oil equivalent

DCN ..... Decarbonylation

DCX ..... Decarboxylation

DEK ..... Diethyl ketone

DFT ..... Density functional theory

ZPE ..... Zero-point energy

Ea ..... Activation energy

FID ..... Flame ionization detector

FT ..... Fischer-Tropsch

FTIR ..... Fourier Transform Infrared

FWHM ..... Full width at half maximum

GC ..... Gas chromatography

HAADF ..... High-angle annular dark-field

HAc ..... Hexanoic Acid

HDO ..... Hydrodeoxygenation

HPAs ..... Heteropoly acids

HYS ..... Hydrogenolysis

ICP ..... Inductively coupled plasma

KIE ..... Kinetic Isotope Effect

MFC ..... Mass flow controller

MS ..... Mass spectroscopy

NMR ..... Nuclear magnetic resonance

PAc ..... Propanoic Acid

PPM ..... Parts per million

PZC ..... Point of zero-charge

QMS ..... Quadrupole mass spectrometer

RGA ..... Residual gas analyzer

SEA ..... Strong electrostatic adsorption

SMSI ..... Strong metal-support interaction

STEM ..... Scanning transmission electron microscope

TCD ..... Thermal conductivity detector

TOF ..... Turn-over frequency

TPD ..... Temperature programmed desorption

TPO ..... Temperature programmed oxidation

TPR ..... Temperature programmed reduction

UHP ..... Ultra high purity

VLE ..... Vapor-liquid equilibrium saturator

XPS ..... X-ray photoelectron spectroscopy

XRD ..... X-ray diffraction

CHAPTER 1

INTRODUCTION

1.1 OVERVIEW

The combustion of fossil fuels releases carbon dioxide, a major greenhouse gas, into the atmosphere. Most climate scientists believe that the build-up of this gas is one of the primary causes of global warming. Moreover, the extraction and utilization of these fossil fuels contribute to air pollution and can cause harm to both human health and the environment. The increasing demand for fossil fuels coupled with the decreasing availability of those resources, has prompted a move towards the alternate energy production and utilization [1, 2]. This new era research promises to bring ever greater advances in the science and technology of renewable energy production, of which biomass conversion to fuels and chemicals is a major component [3].

Biomass is a matter that is often thought of as garbage, and includes material that is often just laying around, such as dead trees, left-overs from crops, wood chips and bark, and sawdust from lumber mills. Low-cost biomass feedstock, such as waste greases and non-food oils from algae or plants that can grow on marginal lands contain a large amount of oxygen in their chemical structures that need to be removed for liquid fuels applications. The conversion of low-cost biomass feedstock and other raw bio-renewable materials into liquid hydrocarbon fuels is a goal that is being significantly pursued. Interest is peaking

our demand for energy increases and as environmental regulations for energy production is becoming more stringent. Leading experts have predicted that by 2030, around 20% of transportation fuels and 25% of chemicals will come from biomass [4]. Based on the reports from the Department of Agriculture (USDA) and Oak Ridge National Laboratory, the United States produces 1.3 x 10^9 metric tons of dry biomass each year. They are categorized as: agricultural (72%) and forest (28%), and it would not affect the food and export demands [5]. The cost of this biomass ranges from $5 to $15 per *BOE or boe* (barrel of oil equivalent) [6]. The limiting factor in the use of biomass as a feedstock is the development of new biomass conversion processes that are both technologically and economically viable. Figure 1.1 illustrates a biomass processing cycle (carbon cycle), showing the recycling of carbon from the atmosphere into plants and then into soils.

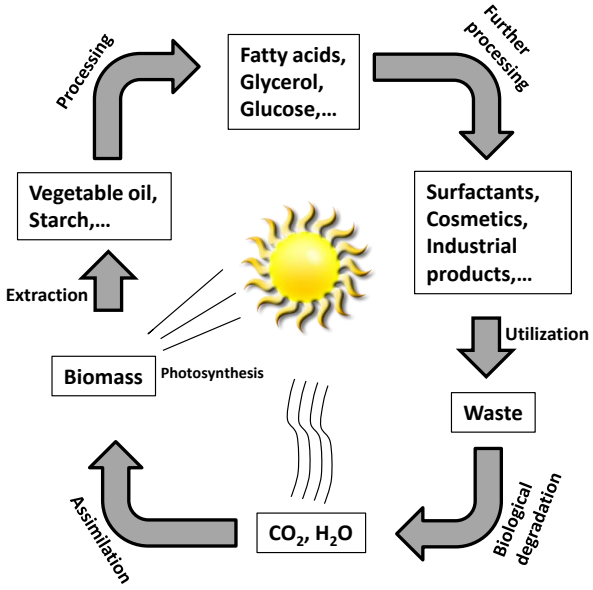

Figure 1.1: Schematic of biomass processing cycle.

Consequently, catalysis researchers in both industry and academia are devoting much attention to the design and discovery of new techniques for the development of catalytic processes for conversion of biorenewable feedstocks.

Heterogeneous catalytic gas- and liquid-phase deoxygenation of non-food biomass-derived feedstocks to produce fuel is an area of much current interest. Overall, catalytic deoxygenation (including HDO) is one of the most promising (yet underdeveloped) processes for generating a hydrocarbon fuel from biomass. During the HDO process, H_2 is co-fed with the reactant to facilitate hydrogenolysis (HYS) and hydrogenation reactions required for the removal of oxygen. In the case of long chain fatty acids and acid esters, the HDO process results in the production of a liquid with high energy density that possesses identical properties to those of conventional fossil fuels. Thus, typical feed streams will contain free fatty acids and/or fatty acid esters or a combination of both. Usually, the feed stream is heated in the presence of a heterogeneous catalyst to produce a partially deoxygenated stream. The partially deoxygenated stream undergoes further deoxygenation depending on the reaction temperature, hydrogen pressure, metal and support effect to produce an effluent stream containing the hydrocarbon.

Equations 1-6 illustrate the hydrogenation, decarbonylation, and decarboxylation pathways proposed for the HDO of organic acids and esters. In addition, the CO_2 and CO products from the decarboxylation and decarbonylation routes can undergo further reaction through water-gas shift and methanation, consuming large amount of H_2.

Hydrogenation

$$R_1 - COO - R_2 + 4H_2 \leftrightarrow R_1 - CH_3 + R_2 - H + 2H_2O \quad (1)$$

$$R - COOH + 3H_2 \leftrightarrow R - CH_3 + 2H_2O \quad (2)$$

Decarbonylation

$$R_1 - COO - R_2 + 2H_2 \leftrightarrow R_1 - H + R_2 - H + CO + H_2O \quad (3)$$

$$R - COOH + H_2 \leftrightarrow R - H + CO + H_2O \quad (4)$$

Decarboxylation

$$R_1 - COO - R_2 + H_2 \leftrightarrow R_1 - H + R_2 - H + CO_2 \quad (5)$$

$$R - COOH \leftrightarrow R - H + CO_2 \quad (6)$$

This dissertation aims to explore the catalytic chemistry of the HDO of aliphatic carboxylic acids over supported group VIII noble metal-based catalysts. Propanoic acid has been chosen as the model compound, since it is representative of the chemistry expected to occur in longer chain acids. Monometallic catalysts are proposed for study, based on their potential to catalyze different bond breaking events relevant to the above reactions. The review allows for understanding the possible reaction pathways for the HDO, identification of the key reaction intermediates expected to be formed during HDO of small carboxylic acids, and surface chemistry of such organic acids, especially related to monomer and dimer/catemer formation on surfaces. This will be followed by a description of the previous research that has been performed, including the experimental protocol, catalyst screening, and kinetic studies.

1.2 Background and Current State of Knowledge

Recently, researchers have increased their efforts to develop new catalytic techniques for the biomass conversion into efficient hydrocarbons for the bio-fuel industry [7, 8]. Unfortunately, there are a few industrial/chemical hydroprocesses for the selective HDO of carboxylic acid into alkane [9-17]. The following section presents an overview of the literature pertinent to the hydroproccesing such as hydrodeoxygenation (including deoxygenation and hydrogenation) of biomass explicitly on triglyceride-based feed such

as carboxylic (i.e. aliphatic) acids and esters. The section will be divided into three main parts:

- Deoxygenation of carboxylic acids and esters
- Hydrogenation (hydrodeoxygenation) of carboxylic acids and esters
- Acid decomposition: Interactions of carboxylic acids on the catalyst surface

1.2.1 CHEMICAL CHARACTERISTIC FOR THE TRANSFORMATION OF BIOMASS INTO BIO-FUELS

Biomass is an alternative renewable source readily available in the environment and the increased interest to reduce the consumption of fossil fuels have prompted a move towards the utilization of biomass as a source of energy, especially for the production of transportation fuels [18]. Biomass feedstock can be obtained from waste materials, forest products, energy crops or aquatic biomass [19, 20]. There is a variety of chemical/industrial reactions for the processing of biomass (i.e. lignocellulosic) including: fermentation, dehydration, aldol condensation, hydrolysis, hydrogenation, esterification, epoxidation, hydroformylation, isomerization, etc. [9, 21, 22]. While a whole range of products can be obtained from biomass, the ones considered relevant for the energy industry include terpenes, vegetable oils, lignin and sugars [22]. Renewable fuels can be classified as:

a. Produced from conventional processing of edible feedstock
    i. ethanol from the fermentation of sugarcane
    ii. biodiesel from the esterification of triglycerides
b. Gasification, hydroprocessing and pyrolysis of non-edible feedstock
    i. Waste greases
    ii. Lignocelluloses

c. Harvesting and advanced processing of ultra-high yield biomass

i. Algae

As shown in Figure 1.2, biomass can be divided into three categories: carbohydrates (cellulose, hemicellulose), lignin (oxygenated polyaromatics) and vegetable fatty oils (triglycerides, fatty acids) [23]. These molecules derived from lignocellulosic substances contain great amounts of oxygen such that C:O approaches 1:1. Generally, if a molecule contains high oxygen concentration, its energy density will be lower [24]. Table 1.1 summarizes the common organic substances that biomass contains along with their atomic composition (carbon and oxygen contents). Cellulose constitute 40-80wt% of biomass entailing the main component of plant cell walls, composed of a crystalline glucose polymer consisting of a linear polysaccharide with β-1,4 linkages of D-glucopyranose monomers. Cellulose is essentially hydrophobic, except for the sides of the chain that are hydrophilic, and forms hydrogen bonding because all the aliphatic hydrogen are in the axial position [25]. In contrast, hemicellulose is a complex amorphous polymer (constitutes 20-40 wt% of biomass) that contains five different sugars. The common sugars are: xylose, arabinose, galactose, glucose, and mannose. Compared to cellulose, hemicellulose is easy to hydrolyze because of it branched composition [26]. 10-25 wt% of biomass consists of lignin, which is a branched, substituted, mononuclear aromatic polymer found mostly in trees. It is formed mainly on the polymerization of coniferyl, sinapyl and coumaryl alcohol. The polymer can bond at different sites of the phenylpropane monomer based on the electron delocalization in the aromatic ring, the double bond containing the side chain, and the oxygen functionalities [27].

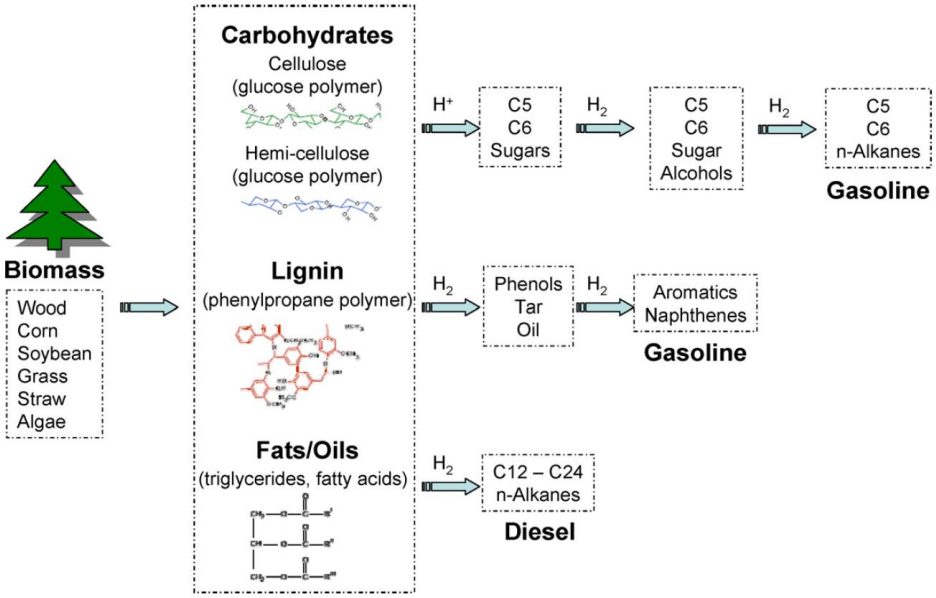

Figure 1.2: Hydrodeoxygenation of the basic building block of biomass to renewable hydrocarbon fuels.

Table 1.1: Atomic composition of common biomass feedstock and fuels.

SUBSTANCE	C (MOL%)	H (MOL%)	O (MOL%)	H/C	O/C	AVG. FORMULA
Pine (Hard)	32	48	20	1.5	0.6	$C_{1.6}H_{2.4}O$
Corn stover	33	46	21	1.4	0.7	$C_{1.6}H_{2.2}O$
Rice husk	29	48	23	1.7	0.8	$C_{1.3}H_{2.1}O$
Cottonseed hull	22	48	30	2.1	1.3	$C_{0.7}H_{2.2}O$
Cellulose	29	48	23	1.7	0.8	$C_{1.3}H_{2.1}O$
Hemi-cellulose	33	48	19	1.4	0.6	$C_{1.2}H_{2.5}O$
Lignin	40	46	14	1.2	0.3	$C_{2.9}H_{3.3}O$

Crude oil	38-46	54-72	<2	1.5-2.0	<0.03	$CH_{1.5}$
Liquefaction bio-oil	40-44	49-53	7	1.1-1.3	0.1-0.3	$C_6H_{7.3}O$
Gasoline	33-37	63-67	<0.01	1.7-2.0	<0.01	$CH_{1.9}$
Diesel	33-37	63-67	<0.01	1.7-2.0	<0.01	$CH_{1.9}$
Ethanol	22	67	11	3.0	0.5	C_2H_6O
DME	22	67	11	3.0	0.5	C_2H_6O
MTBE	28	66	6	2.4	0.2	$C_5H_{12}O$
Methane	20	80	0	4.0	0	CH_4

Other minor components of biomass, but equally important, are extractives (i.e. terpenes, starches) and triglycerides. Triglycerides are high-energy density liquid molecules, found in vegetable oils and animal fats that contain hydrophobic substances involving one molecule of glycerol and three molecules of fatty acids. The substance can be demonstrated with the general formula $CH_2(OCOR_1)CH(OCOR_2)CH_2(OCOR_3)$, where R_1, R_2 and R_3 can be the same or different and can have different chain lengths. Examples of triglycerides are: canola, almond, corn, peanut, sunflower seed oils, coconut and shea butter, tallow animal, beef and milk fat. Currently, triglycerides can be converted through trans-esterification, wherein the substance reacts with an alcohol (usually methanol) to produce an alky ester and glycerol over an acid or base catalyst. The alkyl ester (also known

as fatty acid methyl ester- FAME) can be used directly as a diesel fuel and is called B100. In addition, the ester can be blended with traditional diesel fuel (20 vol%) and is called B1-20. Trans-esterification is widely used and produces fuels that contain apt energy density, particularly when mixed with conventional diesel. However, this process is significantly costly and produces large amount of waste. Furthermore, it can suffer hydrolyzing of the ester with carboxylic acids usually forming soap and causing corrosion, filter plugging and long-term storage problems [28].

Two general approaches are known for the HDO of triglycerides involving the hydrotreatment of vegetable oils (i.e. stand-alone) and co-processing the vegetable with crude oil in a petroleum refinery. In addition, Table 1.2 compares the composition of crude oil with bio-oil produced by different hydroprocesses (determined by the American Petroleum Institute) [29]. The amount of carbon in the liquefied bio-oil can be compared to the crude oil, however the amount of oxygen lead to a great disadvantage. The energy of the fuel can significantly increase, however deoxygenation to produce less than 5wt% oxygen is required to obtain low viscosity fuels for practical applications [30].

Table 1.2: Comparison of the chemical composition between the conventional oil and bio-oil.

	Conventional crude	**Coal-derived naphtha**	**Oil shale crude**	**Bio-oils**	
				Liquefied	**Pyrolized**
Carbon	85.2	85.2	85.9	74.8	45.3
Hydrogen	12.8	9.6	11.0	8.0	7.5

H/C	1.8	1.4	1.5	1.3	2.0
Sulphur	1.8	0.1	0.5	<0.1	<0.1
Nitrogen	0.1	0.5	1.4	<0.1	<0.1
Oxygen	0.1	4.7	1.2	16.6	46.9

As stated above, the primary goal of this project is to study the hydrodeoxygenation reactions involving the conversion of triglyceride-based feed with specific attention to carboxylic acids. The hydrodeoxygenation (HDO) reaction has been of great importance since 1980's [31, 32]. The first review about HDO was published in 1983, however very limited information concerning biomass HDO was available during that period [33]. It is known that an ideal reaction would be of the organic acid reacting with hydrogen to remove the heteroatom oxygen to form water at low temperatures and hydrogen pressures. However, the process for oxygen removal by HDO requires a heterogeneous catalyst, used at moderate to high temperatures (300-600ºC) and usually under high H_2 pressures. Table 1.3 compares HDO with other types of hydroprocessing methods such as high-pressure liquefaction and flash pyrolysis [34]. These processes are highly expensive and further upgrading to remove the remaining oxygen is still required [35]. Depending on the substance, HDO can be favorable or undesirable. For example, HDO of aromatic compounds should be avoided, since this decreases the octane number while consuming more H_2.

Table 1.3: Properties of bio-Oils and upgraded bio-oils.

	High-press. liquefaction	**Flash pyrolysis**	**Hydro-deoxygenated bio-oils**
Carbon (wt %)	72.6	43.5	85.3-89.2
H_2 (wt %)	8.0	7.3	10.5-14.1
Oxygen (wt %)	16.6	46.9	0.0-0.7
Sulfur (wt %)	<45	29.0	0.005
H/C atom ratio	1.21	1.23	1.4-1.97
Density (g/mL)	1.15	24.8	0.796-0.926
Moisture (wt %)	5.1	24.8	0.001-0.008
Viscosity (cP)	15K (61 ^oC)	59 (40 ^oC)	1.0-4.6 (23 ^oC)

1.2.2 HYDROPROCCESING OF CARBOXYLIC ACID AND ESTERS

Carboxylic acids and esters are triglycerides-based feeds that can be hydro-treated to produce hydrocarbons. The triglycerides can decompose to fatty acids that can then undergo hydrogenation, decarboxylation and/or decarbonylation. The product contains either an equivalent number of carbons, or one less carbon, than the reactant, depending on the reaction pathway. Carboxylic acids (RCOOH) are organic acids that contain at least one carboxyl group. The carboxyl group is composed of two functional groups: carbonyl (R-C=O) and hydroxyl (R-O-H). They are considered as Brønsted-Lowry acids because of their ability to donate protons. The acid could be as simple as formic acid (H-COOH), or a more complicated, long carbon chain molecule such as lauric acid ($C_{12}H_{24}O_2$). Organic acids can also contain two or three carboxyl groups, called dicarboxylic and tricarboxylic,

respectively [36]. Esters usually are formed by the replacement of the hydroxyl group in an organic or inorganic acid by an alkoxy group. Carboxylic acid esters can be hydrogenated to form alcohols, and is dependent on the catalyst, the hydrogen pressure, and the structure of the substrate molecule. The hydrogenation of ester to alcohols is a reversible reaction; and the temperature and pressure affect the concentration of the esters and alcohols [37, 38]. Usually the reaction takes place in a slurry phase or fixed bed reactor over metal over supported metal oxide [39].

In summary, biomass conversion is an arduous process that requires heterogeneously catalyzed reactions involving high H_2 pressure, moderate temperatures, and an active and selective catalyst. Further separation processes are needed in order to achieve the formation of useful hydrocarbon chemicals for the bio-fuel industry. From this section forward, the deoxygenation and hydrogenation of carboxylic acids and esters will be discussed in detail. Additionally, the catalyst metal and support effect on these reactions will be reviewed. The decomposition of carboxylic acids on different metal and support will be investigated in order to understand the reaction mechanism and the kinetics that involves the hydrodeoxygenation of carboxylic acids.

1.2.3 METAL SELECTION FOR THE HDO OF CARBOXYLIC ACID AND ESTER

The type of catalyst is crucial for the performance of HDO reactions, with the choice of metal being especially important. The metal is responsible for absorbing the reactants, especially hydrogen for the hydrogenation reaction. Electronic and geometric properties of the catalyst such as high electron densities and the amount of edges and corners respectively, can affect the reaction rate and selectivity. These properties influence the surface reactions, which are affected by the reactant, intermediate, and product

adsorption, and vary depending on the metal surface. From this section forward, current literature for the type of deoxygenation/HDO reactions and the catalyst used in the liquid and gas phased hydroproccesing will be discussed.

1.2.4 Deoxygenation of Carboxylic Acid and Ester

To understand thoroughly the HDO reactions, extensive studies on the deoxygenation of carboxylic acids and ester should be made. The production of hydrocarbons does not happen in a simple reaction; mainly it is composed of several parallel reactions that are affected by the nature of the process. As mentioned previously, some reactions may require hydrogenation of the molecule followed by deoxygenation, and hence formation of the hydrocarbon. Decarboxylation and decarbonylation reaction are present as well and the process may encounter water gas shift and methanation reactions. The catalytic deoxygenation reaction has been used extensively since the 1970's [40]. There are two common types of deoxygenation reactions relevant to this proposal: The Barton-McCombie reaction which comprises the replacement of a hydroxyl group by hydrogen to give an alkyl group and the Wolff-Kishner reduction where the oxo group is replaced by two hydrogen atoms[41]. The Barton-McCombie reaction is commonly used for the deoxygenation of alcohols to produce hydrocarbons, while the Wolff-Kishner is used to reduce a ketone or aldehyde to produce an alkane. In this type of reactions it is important to have selective deoxygenation, without breaking the C-C bonds and hence obtain the desired product.

Considerable amount of research have been done for the deoxygenation reactions, however, the selective deoxygenation of renewable feedstock leading to biodiesel product is a relatively new topic. Several studies recently demonstrated that renewable feeds over

heterogeneous catalyst in gas and/or liquid phase decarboxylate by the removal of the carboxyl group in the fatty acid and ester, producing CO, CO_2 and linear hydrocarbons[42]. The following section will discussed in detail the effect of the supported noble metals on this particular reaction.

1.2.5 DEOXYGENATION: EFFECT ON SUPPORTED NOBLE METAL CATALYSTS

Recently, intensive research from Snare, Lestari and Murzin et al. have been focusing on the liquid phase catalytic deoxygenation of fatty acids and their esters (e.g., palmitic and stearic acid, ethyl stearate and tristearine) for the formation of hydrocarbons[10, 43]. A mixture of 59% palmitic and 40% of stearic acid was investigated [44]. The main products for this reaction were C_{16} and C_{18} straight chain hydrocarbons with one carbon less than the corresponding acids. Different noble metals such as: Ni, Ni/Mo, Ru, Pd, Pt, Ni, Rh, Ir etc. were tested on different supports (i.e., metal oxides, carbon) for the screening of deoxygenation reactions [16, 43, 45] . However, the majority of their research has focused on these reactions over 1-5wt% Pd/C. The reactions were carried out in semi-batch and continuous mode (discussed later) [46]. They explored the influence of metal, support, solvent, temperature, initial concentration and reaction atmosphere (i.e carrier gas) on the decarboxylation and/or decarbonylation reaction of fatty acids and their esters. The decarboxylation of stearic acid at 300 ºC under Helium yielded a 97% conversion to n-heptadecane. The addition of hydrogen favored the decarboxylation reaction, as well as the initial reaction rate. For ethyl stearate, the decarboxylation was mostly achieved with alkaline Pd/C and it was shown that stearic acid was an intermediate in the conversion of this reactant[42]. Nevertheless, using the alkaline catalyst resulted in the formation of aromatic compounds. The prominent gaseous product formed was carbon monoxide, as

opposite to stearic acid where carbon dioxide was produced. The decarboxylation of stearic acid to produce n-heptadecane is more favorable than the DCX of ethyl stearate since the reaction pathway of the ester favors the formation of aromatic compounds and unsaturated olefins.

In addition to semi-batch mode, Lestari and Murzin et al. reported the continuous deoxygenation of stearic acid ($C_{18}H_{36}O_2$) and lauric acid ($CH_3(CH_2)_{10}COOH$) in liquid phase over mesoporous 5wt% Pd/C catalyst beads [14, 43]. The main emphasis was on the catalyst stability and the parameters investigated were reaction temperature, initial concentration of the acid and the type of solvent. The major product obtained was heptadecane with a 15% conversion at 633K and the gaseous products were CO and CO_2. The main reactions were decarbonylation and decarboxylation. The CO formed can be due to the decarbonylation of the acid or through a reverse water-gas shift reaction. When comparing the amount of CO and CO_2 to the amount of paraffin and olefin formed, they found that at the beginning of the reaction the amount of CO_2 decreased while the amount of CO increased. The concentration of the paraffin was lower compared to the concentration of CO_2. Therefore, a reverse water-gas shift reaction for the CO formation was inferred. The catalyst suffered deactivation due to coking and/or poisoning of CO and CO_2.

Murzin and Bernas proposed that the catalytic deoxygenation of dodecanoic acid under inert atmosphere can be achieved [45]. The reaction was carried out with 1wt% Pd/C and under similar conditions stated before (reaction temperature, pressure, gas flow rate etc.). Argon was utilized as the inert gas and no solvent was required. The conversion towards dodecane and dodecene was between 90-100%. The pressure did not have a

significant effect on the catalytic performance; however coking deactivated the catalyst, since hydrogen is known mitigate coke formation. The cause for the deactivation of supported Pd catalyst on the decarboxylation reactions of fatty acids was investigated by Jones et al [47]. The recyclability of the catalyst was evaluated in a batch DCX reaction of stearic acid at 300 ºC under inert atmosphere. They concluded that the deactivation of the catalyst was due to the strong adsorption of reactants and products on the surface. This suggests that the coke formation reported by prior literature was not a factor for the deactivation. Their assumptions were supported by several characterization techniques made on the spent catalysts, including XPS, TEM, physisorption, chemisorption, NMR, and FT-IR.

The effect of metal dispersion was analyzed by Murzin and co-workers, using four synthesized 1.0 wt% Pd/C catalysts, for the deoxygenation of palmitic and stearic acid [48]. The reaction was carried out at a pressure of 17.3 atm and temperature range 260-300 ºC. The main products were heptadecane and pentadecane. They assumed that the deoxygenation of the fatty acids should be independent of the alkane chain length since it is far from the reactive center (i.e., deoxygenation occurs on the carboxylic group). The metal dispersions of 47 and 65% exhibited similar high activities compared to 18 and 72% dispersion. It was proposed that the higher dispersed Pd metal has a stronger interaction with the support, which makes the metal structure less favorable for the deoxygenation of the carboxylic acid. In contrast, the 47 and 65% dispersion catalyst resulted in higher activity due to the uniformity of the Pd particle size distribution enhancing the surface structure required for the deoxygenation. Lower dispersion catalysts (18% disp.) were not enough active due to the lack of surface area and higher dispersion catalysts (72% disp.)

was not active due to the strong metal-support interaction (SMSI) (discussed in section 2.3.3) [49-51]. A metal dispersion between 47-65% (particle size between 1.7-2.3 nm) resulted to be the best catalyst for this particular reaction. It should be noted that the metal dispersion only affected the deoxygenation rate but not the product distribution.

Work from Lamb and co-workers concentrated on the deoxygenation of C_{18} free fatty acids (i.e. stearic acid) over 5wt% Pd/C employing on-line quadruple mass spectrometry (QMS) technique [52]. The technique can determine a connection between CO_2 and H_2 evolution which can help understand the formation of unsaturated compounds at low to intermediate conversions. QMS showed that H_2 is evolved at the same time as CO_2. Prior to reaching 100% conversion, the stearic acid undergoes decarbonylation generating unsaturated compounds, forming CO, which then undergoes the water-gas shift reaction forming CO_2 and H_2. As the reaction temperature increases, hydrogenation of heptadecene occurs via the hydrogen transfer from the solvent (i.e. dodecane) yielding 98% heptadecane. Moreover, the addition of 10% H_2 stabilizes the catalyst and avoids the formation of unsaturated compounds that inhibit the catalyst activity that can adhere on the catalytic surface and avoid further decarboxylation reactions.

1.2.6 Hydrogenation of Carboxylic Acid and Esters

Catalytic hydrogenation is used widely for the production of alcohols, aldehydes and ketones from fatty acids and esters. The challenge arises from the reduction of C=O bond which is less thermodynamically favored from that of the C=C bond [53]. Hydrogenation is an important reaction pathway in the hydroproccesing of organic acids and esters, wherein hydrogen reacts with carboxylic acid and/or ester in the presence of a catalytic surface to produce an alcohol or an aldehyde that can undergo further

deoxygenation steps. The organic acid on the surface of the heterogeneous catalyst can experience competitive/noncompetitive, dissociative/non-dissociative adsorption and desorption reactions, adsorption of solvents, coke formation etc. As part of the hydrogenation reaction of carboxylic acids and ester to produce hydrocarbon, we encounter deoxygenation reaction as well. Both processes are interconnected; thus essential for the triglyceride-based feed conversion to bio-fuels. The following section will examined the hydrogenation/hydrodeoxygenation reaction literature that pertain the conversion of carboxylic acid and ester to intermediate products including alcohol and ester trough the formation of hydrocarbon.

1.2.7 SUPPORTED NOBLE METAL CATALYSTS

The required severity of the reaction conditions depends on the nature of the feedstock. For the HDO reactions, it should be pointed out that the molecule size (i.e. amount of functional and/or alkyl groups) can influence the activity and selectivity of the reaction. Riisager et al. explored the HDO on oleic acid and tripalmitin over Pd and Pt supported on γ-Al_2O_3 at 300-350 ºC [54]. At 598 K, the differences in the molecular size and diffusivity of the reactants affected the reaction rate, resulting in the conversion of the fatty acid to be faster than the conversion of the triglyceride. However, at 598 K the reaction rate proceeded fast for both compounds. Pd catalyst was more active than Pt and the reaction rates of both DCX and DCN were higher than that of hydrogenation. Thus, it was concluded that Pd favored C=O bond scission rather than hydrogenation in spite of the significant hydrogen pressure. Experimental work from Valyon et al. compared the hydroconversion of tricaprylin and caprylic acid to hydrocarbons over Pd/C and NiMo/γ-Al_2O_3 [55]. The activity and selectivity were independent of the hydrogen pressure, but

depended greatly on the carboxylic acid intermediates (i.e. alcohol and aldehydes) pressure. They concluded that reaction proceeded via HYS of the multifunctional acid, followed by the HDO of the carboxylic acid. Pd/C favored DCN forming CO, water and alkane and NiMo favored hydrogenation forming mainly alkane and alkene. Murzin et al. also investigated the hydrogenation of linoleic acid to stearic acid over Pd/C and Ru/C [16]. The results showed that 5wt% Pd/C had the highest conversion and selectivity of 100 and 86% respectively. 5wt% Ru/C only reached 90% conversion, due to deactivation. They implied that the deactivation was due to the formation of unsaturated acids, which inhibited the formation of important intermediates. Other research has addressed tall oil fatty acid (TOFA) hydrogenation and decarboxylation over 1wt% Pd/C at 300 ºC to achieve a 95% selectivity toward C_{17} hydrocarbons [17].

Resasco et al. came to the conclusion that the HDO of esters such as methyl octanoate and methyl stearate over Pt/Al_2O_3 at 330 ºC, can be achieved under inert atmosphere. However, the hydrogen suppresses the formation of heavy products such as ketone and ester (i.e., condensate products). The hydrocarbon (mostly C_7) products formed via the oxygen removal, from the oxygen vacancies created on the support or directly via C-O HYS on the metal site, leading to DCN and DCX [56]. Additionally, they compared Pt, Pd and Cu catalyst over precipitated silica at 200 ºC and found that Pt was the most active for the hydrogenation of C=C bond of 2-methyl-2-pentenal [57]. However, Cu was a good catalyst for the total oxygen removal, by hydrogenation of C=O. Even though Pt and Pd exhibited higher activity, the loss of carbon via DCN is a disadvantage since CO is formed. When the reaction was performed over acid catalyst H-ZSM-5 at 500 ºC, the main products were light hydrocarbons and aromatic compounds [58]. In contrast, when the reaction was

carried out over basic CsNaX no aromatics were formed, and the main products were alkenes. Acidic NaX deactivated quickly while forming mostly aromatics [59]

1.2.8 SMALL CARBON-CHAIN CARBOXYLIC ACIDS (SIDE REACTIONS)

As reviewed earlier, it is expected that the reaction mechanism that occurs on monofunctional carboxylic acid that contains for example, 9 carbons or more, that can lead the formation of hydrocarbon will be the same reaction path as for a carboxylic acid with 2 or 3 carbons. Curiously, this is not the case. Carboxylic acids such as acetic and propanoic acid can suffer other reactions when exposed to the catalysts presented earlier for the DCX and DCN reactions. The caboxylate can undergo other reactions prior to DCX that lead to the formation of ketones and esters. The following section will discuss the literature for these types of reactions on metal oxides and on different supports [60].

1.2.9 EFFECT ON METAL OXIDES

In 1930, patented work from Drossbach and Johansen described the production of adelhydes through the catalytic deoxygenation of dicarboxylic acid with a reducing agent (H_2 and CO) over supported metal catalyst and metal oxides. The metal under study belonged to the 5^{th} to 11^{th} group of the periodic table including: Cr, Fe, Cu, Mn and Co either as a metal oxide, alone or in a mixture with each other . The reaction temperature ranged from 200-400ºC. The selective deoxygenation of aliphatic acids to aldehydes followed the Mars van Krevelen mechanism [61-63]. The oxide catalyst offered an oxygen vacancy to the organic acid, followed by the adsorption of one of the oxygen from the acid, and subsequently one carbon-oxygen bond was broken. They concluded that the metal oxide was the most favorable for the aldehyde production.

Consequently, Yokoyama and Yamagata focused their interest on the hydrogenation of aromatic and aliphatic carboxylic acids to the corresponding aldehydes on metal oxides [64]. For aliphatic acids, Cr_2O_3 and the partially reduced Fe_2O_3 gave the highest selectivity. Cr_2O_3 exhibited superior selectivity to aldehyde while avoiding ketonization. Figure 1.3 shows the selectivity to aldehydes, for different metal oxides with increasing bond strength [65]. The selective formation of the aldehyde was greatly affected by the acid-base character of the metal oxide. They concluded that the weak redox properties that metal oxides exhibit might influence the catalyst performance.

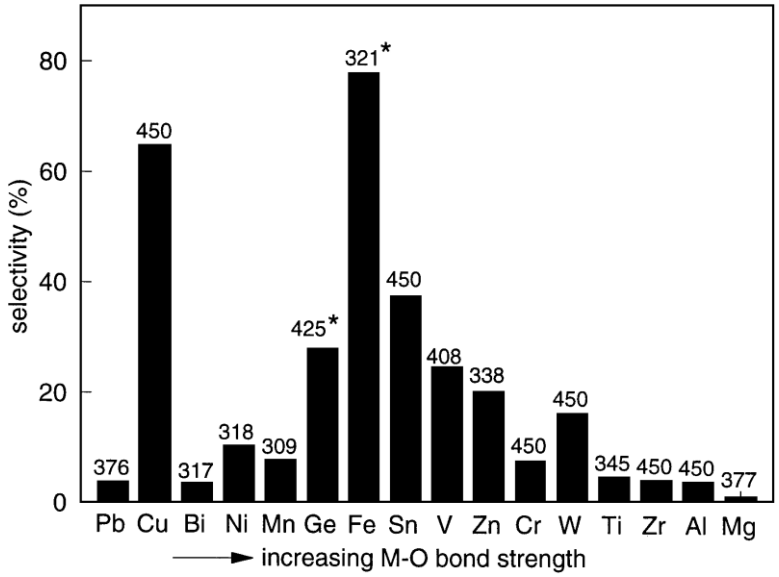

Figure 1.3: Plot of maximum selectivity as a function of increasing (not on scale) metal–oxygen bond strength. Above each bar is given the temperature (ºC) at which this selectivity is reached.

Ponec et al. investigated the relationship between the α-hydrogen atoms of four carboxylic acids and the selectivity towards the aldehyde [66]. The carboxylic acids were: acetic (three α-hydrogen), propanoic (two α-hydrogen), isobutyric (one α-hydrogen) and pivalic (zero α-hydrogen). The catalysts utilized include oxides of iron, vanadium,

zirconium, and titanium. The study concluded that the abstraction of the α-hydrogen enhances the selectivity towards the aldehyde instead of the by-product ketone. The ketonization reaction requires the presence of α-hydrogen, since this reaction proceeds via the ketene-like intermediate or via Claisen condensation to form β-keto acid that leads to decarboxylation [67, 68]. The acids that contained two or more α-hydrogen were prone to absorb on the catalyst surface and form a carboxylate. The carboxylate can form the ketene intermediate, whereupon coupling with a methyl group can form the ketone. Isobutyric and pivalic acid favored the formation of the aldehyde on iron, vanadium and titanium oxide catalysts. Figure 1.4 explains diagrammatically the carboxylate formation and the several possible reactions to form ketone.

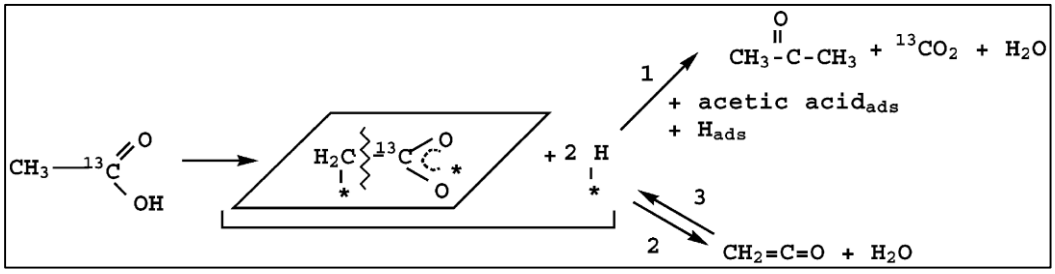

Figure 1.4: Reaction mechanism for the ketonization of acetic acid.

Dumesic et al. focused their attention on the ketonization and esterification reactions of hexanoic acid (HAc) over $Ce_{0.5}Zn_{0.5}O_2$ catalyst, at 448-623 K and HAc partial pressure ranging 0.05 to 0.03 atm [69]. They proposed that the ketonization and esterification reactions are key processing steps for the biomass conversion, with, low temperature reactions favoring esterification over ketonization. This is in good agreement with the activation energies for ketonization (132 kJ/mol) and esterification (40 kJ/mol). A temperature of 548 K was required to favor the ketonization reaction. Additionally, reverse esterification became significant at this temperature, to replace the carboxylic acid

consumed by ketonization. The pressure of the acid had an effect on the ketonization reaction rate; shifting from second order to zero order over a hexanoic acid pressure range of 0.05-0.75 atm. Water and CO_2 were found to inhibit esterification.

Another important attribute of HDO catalysts could be strong-metal-support interactions (SMSI) that have been shown to exist on metal oxides such as TiO_2, V_2O_3, Nb_2O_5 and Ta_2O_5. These interactions and their properties have been used to explain why for example Pt/SiO_2 or other metal oxide are not as effective for the C=O hydrogenation as Pt/TiO_2. Moreover, this active hydrogenation could be caused by the hydrogen spillover generated by the Pt (low temperature reduction) that reacts with the carboxylic acid adsorbed on the oxide support. This issue has been investigated by Resasco [70], who showed that the metal and the support have a considerable effect on the hydrogenation of AAc. As a result, they developed a kinetic modeling following the Langmuir-Hinshelwood-type sequence that gave the most consistent fit of the data. The high temperature reduction (HTR) of Pt/TiO_2 showed TOF values 7-8 times greater than the catalysts treated by low temperature reduction (LTR). Pt powder, Pt/SiO_2 and Pt/Al_2O_3 resulted mostly on decarbonylation and decomposition reactions. Hardacre et al. publish work on the study of an efficient hydrogenation of carboxylic acids to alcohols and alkanes utilizing Pt over TiO_2 [71]. The study proposed that HDO can be achieved at 333 K and 5 atm. The catalyst achieved high conversion (83%) and selectivity towards alcohol (93%). The addition of Re to form a bimetallic catalyst lead to higher conversion (86%), however the selectivity shifted towards 33% alkanes (67% alcohol). The improved-activity Pt-Re catalyst was attributed to the increased oxyphilicity that the surface exhibited when exposed to Re cations. The electron pair of the carbonyl group interacts with the Re cations, thus favoring

the formation of the alkanes and CO_2. Figure 1.5 demonstrates the oxygen vacancy mechanism for Pt/metal oxide and the corresponding products.

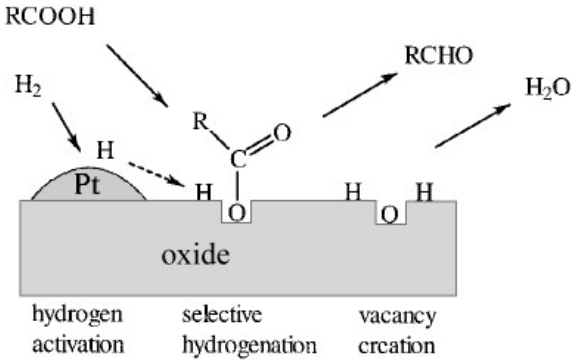

Figure 1.5: Schematic representation of reaction steps in the selective hydrogenation of carboxylic acid to the corresponding aldehyde.

Kozhevnikov and co-workers investigated bulk Keggin heteropoly acids (HPAs) $H_{3+n}[PMo_{12-n}V_nO_{40}]$ (n=0-2) and their Cs^+ salts that catalyze the vapour-phase hydrogenation of propanoic acid (PAc) at 623 K and 1atm H_2 forming mainly propanal, diethyl-ketone and propane [73]. HPAs a very strong acids (considered Brönsted acids) and are efficient oxidants (redox transformation). Additionally, the acids have a very high solubility in polar solvents and fairly high thermal stability in the solid state [74] . Different HPC catalysts were tested, and ~ 90% conversion was obtained for PMo at the first 15 min. The drawback arose when the catalyst showed considerable deactivation after 12 hr of operation. The catalysts produced mainly propanal and propane. A kinetic study was performed using differential conditions (conversion ≤ 10%) utilizing $Cs_{2.4}$OMoV catalyst at 2-7 vol% PAc in H_2 flow in the temperature range 593-653 K. The reaction was zero order with respect of PAc. They concluded that the reaction was not affected by diffusion limitations. The mechanism is also similar to the metal oxide Mars-Van Krevelen redox

type mechanism discussed previously. Tuning the catalyst acidity by Cs substitution enhances greatly to selectivity towards propanal.

1.2.10 SUPPORT EFFECT ON THE HYDROGENATION OF CARBOXYLIC ACID AND ESTER

The principal objective of the support is to aid in dispersing the metal, since higher metal dispersion often leads to higher activity. Supports can be categorized as acidic, basic, amphoteric, and carbon based. Supports can be inert or non-inert. For example, a non-inert support can form with the metal an alloy or segregate such as the reduction of TiO_2 to TiOx. The surface area, pore volumes, acidities, electronic and geometrical properties can vary depending on the catalyst and application. The support could be a powder, paste, pellet, fiber or a monolith [75, 76].

Commonly, supports are inorganic oxides that could have the form M-O-M and M-OH on their surface. The more acidic oxides, such as silica, have low isoelectric point IEPs indicating a facile production of an anionic surface. In contrast, basic supports (high IEPs) are easily protonated to give a cationic surface. When a surface has a negative charge, cationic species are attracted to it and become adsorbed [77]. The following section will review hydrogenation reactions on different supports.

Rachmady and Vannice studied acetic acid hydrogenation over different supported platinum catalysts [78]. The reaction was carried out in the gas phase in a fixed bed reactor from 150-300 ºC and with 0.1-1 atm of H_2. Four catalysts were considered: Pt/SiO_2, $Pt/\eta Al_2O_3$, Pt/Fe_2O_3 and Pt/TiO_2. The latter was found to be the most active (i.e., higher turnover frequencies) and selective for the formation of alcohol and ester. Based on the reaction order obtained, they were able to model the data using Langmuir-Hinshelwood-

type catalytic sequence, where hydrogen is absorbed dissociatively on the metal and molecular acetic acid is absorbed of the surface of the oxide.

1.2.11 Acid decomposition: Interactions of carboxylic acids on the catalyst surface

Having knowledge of the temperature, pressure, type of catalyst and reaction atmospheres that favors the conversion and selectivity toward aldehyde, alcohols and/or hydrocarbons, is of great importance. However understanding the acid decomposition on the surface of a catalyst is crucial for the interpretation of the reaction mechanism. The hydrodeoxygenation reactions are comprised of several complex reaction pathways that often can occur in a parallel manner. The objective of this section is to review the adsorption chemistry of carboxylic acids on catalytic surfaces. Furthermore, it will focus on understanding the surface reaction mechanism followed by the possible intermediates and the results of steric effects during these surface reactions.

In order to understand the adsorption behavior of carboxylic acids and their derivatives, the structure and reactivity of metal carboxylates will first be discussed. The hydrogen atom in the carboxyl group is very acidic; hence there is deprotonation that leads to the formation of the carboxylate ion. Carboxylates can exist in the ionic form or they can form covalent bonds. The carboxylate anion contains two syn and anti-lone pair of electrons that function as bases and coordinate with a metal cation [79]. Figure 1.6 illustrates the four different type of metal-molecule bonding modes [80]. The (II) configuration, is commonly obtained when only one coordination site is available, this situation occurs when another ligand is present. The symmetric configuration (III) is not found commonly on metal complexes, since the two metal-oxygen bond have different length, reducing the

tension of the ring in the chelating coordination. The ionic form (I) can be seen commonly on alkali metal rather than transition metal complexes. The most common mode is the bridging configuration, found in the HDO of carboxylic acids and esters.

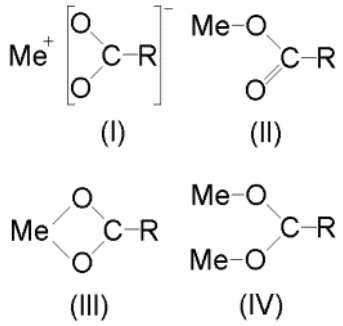

Figure 1.6: Structure of metal carboxylates according to the type of metal–ligand interaction. (I) Ionic or uncoordinated form, (II) unidentate coordination, (III) bidentate chelating coordination, (IV) bidentate bridging coordination.

The metal carboxylate formed by the carboxylic acid decomposition on a heterogeneous catalyst surface decomposes at elevated temperatures. Upon decomposition, the carboxylate loses a carbon and forms carbon dioxide.

Maier et al. proposed an adsorption DCX on Pd metal surface (Figure 1.7) [13]. The α-β-carbons of the carboxylic acid adsorbed on the Pd surface, followed by C-C scission producing CO_2 and an alkyl group. Dumesic et al. used DFT methods and showed that AAc can dissociate upon adsorption on copper over silica, with C-OH cleavage occurring on a hollow site and the adsorption of the acyl group on a bridge site [81]. Neurock and Pallassana reported DFT calculations on HYS of acetic acid over Pd(111) to ethanol, concluding that the most energetic favorable path for the HYS of AAc occurs by the formation of an acetyl intermediate, followed by hydrogenation to the aldehyde. Subsequently, hydrogenation to alcohol occurs, as shown in Figure 1.8 [82]. The DFT results indicated that C-O bond activation was the rate determining step because it is more exothermic and has lower

activation barrier energy compared to the C-OH bond activation which is endothermic and has higher activation barrier energy.

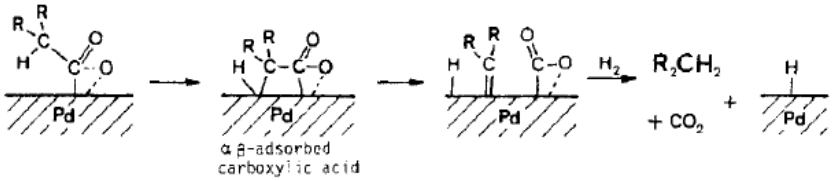

Figure 1.7: Surface decomposition on Pd catalyst of α-β-carbon.

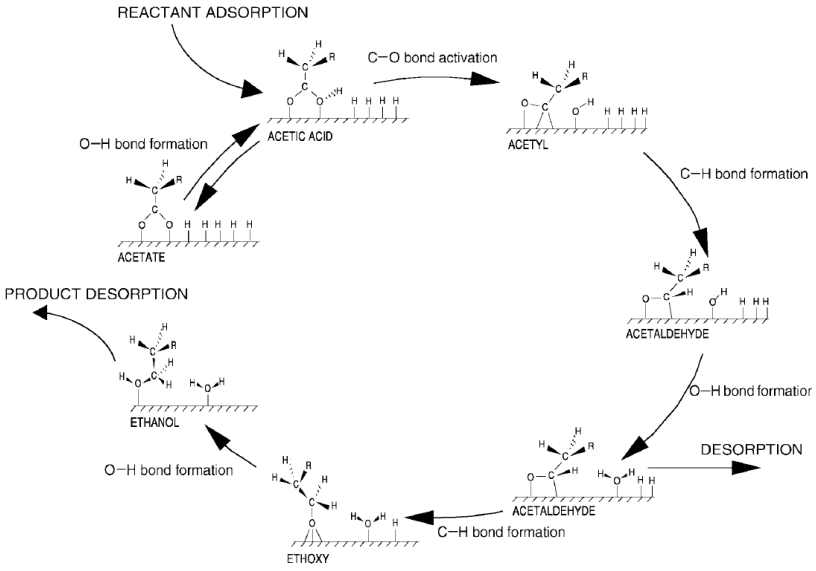

Figure 1.8: Proposed elementary mechanism for the HYS of acetic acid to ethanol over Pd(111), based on DFT-calculated overall surface reaction energies.

CHAPTER 2

EXPERIMENTAL TECHNIQUES

2.1 LIST OF CHEMICAL MATERIALS

Tables 2.1 and 2.2 show the chemicals and gases utilized for the HDO of PAc reaction. The chemicals were used as received. Tables 2.3, 2.4 and 2.5 show the commercial catalysts, the support and the precursors utilized for catalyst synthesis.

Table 2.1: Liquid chemicals utilized for the HDO of PAc. a n-propyl propionate purchased from Sigma- Aldrich

Chemicals	**Physical Properties [F.W (g/mol), B.P (°C)]**	**Concentration (%) [Source: Alfa Aesar]**
Propanoic acid ($C_3H_6O_2$)	74.08, 141	99
Propionaldehyde (CH_3CH_2CHO)	58.08, 48	97
1-Propanol ($CH_3CH_2CH_2OH$)	60.10, 91	99.5
diethyl ketone ($C_5H_{10}O$)	86.13, 102	99
n-propyl propionate	116.16,124	99[a]

Table 2.2: Gases utilized for the HDO of PAca14 liter disposable (Matheson Tri-gas).

Gases (paraffins and olefins)[a]	**PPM**
CH_4	1002
C_2H_4	1000
C_2H_6	995
C_3H_6	1000
C_3H_8	994
C_4H_8	1000
C_4H_{10}	1000

Table 2.3: Commercial and provided catalyst tested.

Commercial Catalyst	**Source**
1.86 wt% Pd/SiO_2	Engelhard
1.67 wt% Pt/SiO_2	
2.0 wt% Rh/SiO_2	
5.0 wt% Pd/C P-56	
5.0 wt% Pd/C	BASF
5.0wt% Pt/C	
2.0wt% Rh/C	
4.0 wt% Pt/TiO_2	Queen's University
4.0 wt% Pt-Re/TiO2	Belfast

Table 2.4: List of type of support and the physical properties (γ-Al_2O_3 powder and carbon were tested with BET).

Support	**Physical Properties (S.A (m^2/g))**	**Source**
SiO_2 powder	100	Engelhard
Carbon powder (CP-97)	615	BASF
γ-Al_2O_3 powder	170	Toyota technical center
TiO_2-Aerosil	46.06	Evonik

Table 2.5: Precursors (salts) utilized for the catalyst screening (soluble in water except, Pd (II) chloride (PdCl2) which is soluble in dilute mineral acids, aqueous metal halides. Additional metal complexes for strong electrostatic adsorption are summarized in chapter 3 (section 3.2).

Salt	**Physical Properties [F.W (g/mol), solubility]**	**Source**
Pd(II) nitrate hydrate ($Pd(NO_3)_2 \cdot xH_2O$)	230.43,	Sigma-Aldrich
Pd (II) chloride ($PdCl_2$)	177.318*	(99.9% Alfa Aesar)
Ru(III) nitrosylnitrate $Ru(NO)(NO_3)_3$	317.09	(31.3% min Alfa Aesar)
Ru(III) chloride hydrate ($RuCl_3 \cdot xH_2O$)	207.43	(99.98% Sigma-Aldrich
Nickel(II) perchlorate ($Ni(ClO_4)_2 \cdot 6H_2O$)	365.70	Alfa Aesar

Iridium(III) chloride hydrate ($IrCl_3 \cdot xH_2O$)	298.56	(99.9%, Alfa Aesar)
Cobalt (II) nitrate hexahydrate ($Co(NO_3)_2 \cdot 6H_2O$)	291.04	(98-102%, Alfa Aesar)
Iron(III) nonahydrate $Fe(NO_3)_3 \cdot 9H_2O$	404.00	(99.99% Sigma-Aldrich)

The gases utilized for the reaction and characterization experiments consisted of: H_2 (UHP), He (UHP), Ar (UHP), O_2 (UHP), 1% CO/He (UHP), 10% O_2/He (UHP), 10% H_2/Ar (2000Psi) and were supplied by Airgas National Welders.

2.2 Catalyst Preparation

2.2.1 Incipient Wetness

A series of catalysts for HDO of PAc reaction screening were synthesized utilizing incipient wetness method [83, 84]. The metals utilized belonged to the group VIII noble metals, and included Ru, Ni, Co, Ir, and Fe. The catalyst consisted of 2.0 wt% metal loading where SiO_2 (3.5 nm powder, Table 2.4) was chosen as the support for comparison purposes with commercial catalysts similarly tested. The SiO_2 pore volume was determined to be 0.70-0.90 cc/g where DI water was added in 10% excess to ensure that the pores were filled completely. The solution of the active phase (i.e. precursor) was previously prepared depending on the amount (g) of salt required to make up to 2wt%. The solution was added drop-wise to the support and stirred each time until a tacky solution was formed. The catalyst was dried in an oven overnight at 70 ºC, followed by calcination with air at several temperatures for 2 hours. Then a sample was reduced (see

table 2.6) in 100% H_2 for 2 hours before TPO, TPR, and H_2-chemisorption/O_2-H_2 titration experiments.

2.2.2 WET IMPREGNATION

A 2.0 wt% Pd/γ-Al_2O_3 was synthesized by conventional wetness impregnation method with $PdCl_4$ as precursor. A solution of 0.8 mL of 1M hydrochloric acid (HCl) (already prepared) was added to 0.07 g of $PdCl_2$ (salt), which was dissolved with water up to 100 mL. Approximately 2-5 g of γ-Al_2O_3 and 100 mL of the Pd solution were added to a 700 mL beaker. The solution was stirred (Fisher Scientific, model# 11-498-7SH) for 3-4 days until it was dried. The dried catalyst followed the process based on Figure 2.1. The catalyst was calcined and reduced at 300ºC for 2 hours in flowing air and H_2, respectively. After reduction, the catalyst was cooled to room temperature and washed with excess DI water (> 2L/g catalyst) to remove any remaining ions and impurities that were not evaporated during the drying process. The catalyst was characterized by TPO, TPR and H_2-chemisorption to determine the metal dispersion as discussed in detail in section 2.1.

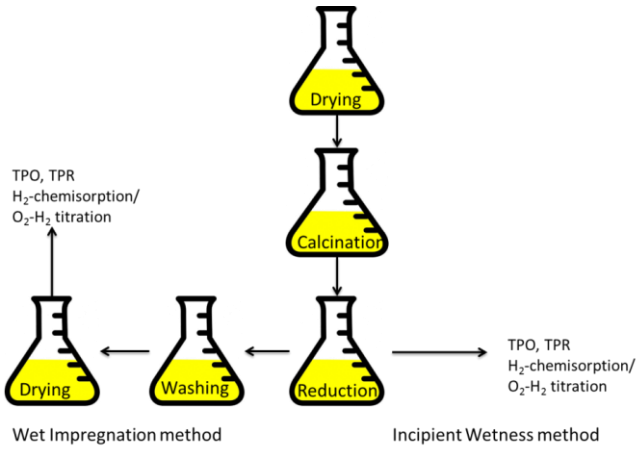

Figure 2.1: Procedure for the preparation of catalyst by incipient and wet impregnation method.

Table 2.6: Calcination and reduction temperature of the synthesized catalyst. a catalyst reduced in the TPR. b correspond to nitrate hydrate and chloride based metal salts. All catalysts were cooled down in a He flow.

Catalyst (2.0wt% M_x/SiO_2 or Al_2O_3)	**Calcination temp. (°C)**	**Reduction temp. (°C)**
Ruthenium	300	300
Nickel	450	450
Iridium	300	400
Cobalt	350	600[a]
Iron	177	600[a]
$Pd/SiO_2(N)$[b]	300	400
Pd/SiO_2 (Cl)[b]	300	400
Pd/ γ-Al_2O_3	300	400

2.2.3 STRONG ELECTROSTATIC ADSORPTION (SEA)

4.0 wt% Pd/SiO_2 and 2.3wt% Pd/TiO_2 were synthesized by strong electrostatic adsorption (SEA). The silica Aerosil-300 (S_{BET} = 330 m^2/g, Evonik) and titania-P25 (S_{BET} = 50m^2/g, Degussa) had a PZC of around 4. Stock solutions of the metal ammine complexes were prepared by placing the desired quantity of metal ammine complexes in a volumetric flask and diluted accordingly. The pH of the metal salt complex solution (200 ppm of $[Pd(NH_3)_2]^{2+}Cl_2$, 99.9% Sigma Aldrich) was controlled based on the PZC of the SiO_2 [85, 86]. Once the pH of the solution is acquired, the support was impregnated and shaken for 1 hour. After the final pH was obtained, the difference (ΔpH) indicated that a strong electrostatic interaction between the metal precursor and the –OH group on the support

took place, allowing a controlled impregnation with highly dispersed metal precursors (see figure 2.2, adapted from *Catalyst preparation: SEA* [87]). The metal concentrations (before and after adsorption) were measured ICP (Perkin Elmer Optima 2000). The accuracy of ICP measurements was improved by using a multi-wavelength calibration, yttrium as an internal standard and multiple replicate data.

Control experiments to measure the pH shift over metal free SiO_2 and TiO_2, were conducted. The samples were weighted and a surface loading (10,000 m^2/L) for 50 mL solutions was prepared. Acidic and basic solutions were created at various pH values ranging from 1-14 with HNO_2 and NaOH. Then, 50 mL of each solution was added to the silica. The solutions were shaken for 1 h. Final pH measurements were taken using a pH electrode. The initial and final pH measurements were then plotted with initial pH on the *x*-axis, and the final pH was plotted on the *y*-axis (as shown in figure 2.3).

The uptake–pH surveys were conducted for the Pd over SiO_2 and TiO_2 using the 200 ppm metal complex solutions and various masses of support such that surface loadings were 1000 m^2/L for both support. Metal solutions of initial pH of about 6-14 were used. Before adding the support, 5-mL portions of the metal complex solution were obtained. After the support was added, the suspensions were placed on an orbital shaker for 1 h, after which 5-mL portions were filtered for ICP analysis. pH measurements also were made at this time. Uptake-pH surveys for Pd/SiO_2 and Pd/TiO_2 are depicted in figure 2.4 and 2.5, respectively. The maximum uptake for Pd/SiO_2 and Pd/TiO_2 were 1.3 $\mu mol/m^2$ for both catalyst. This method can be applied for many ammine complexes to synthesize well-dispersed metals over amorphous silica.[88-90]

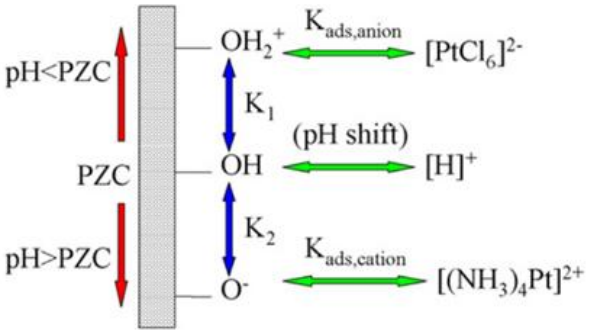

Figure 2.2: Example of a mechanism for Pt amine complexes electrostatic adsorption[87].

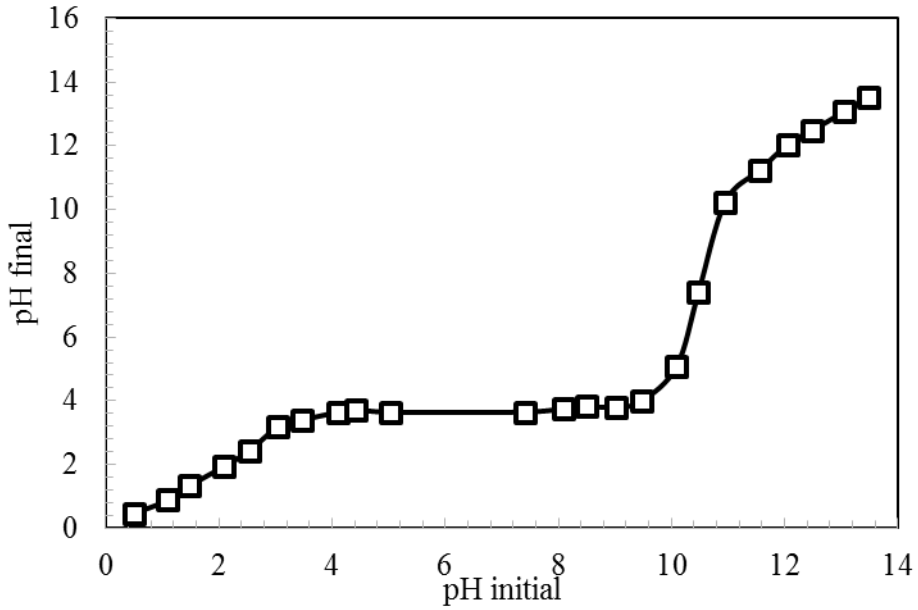

Figure 2.3: pH shift survey for 2.3wt% Pd/TiO_2.

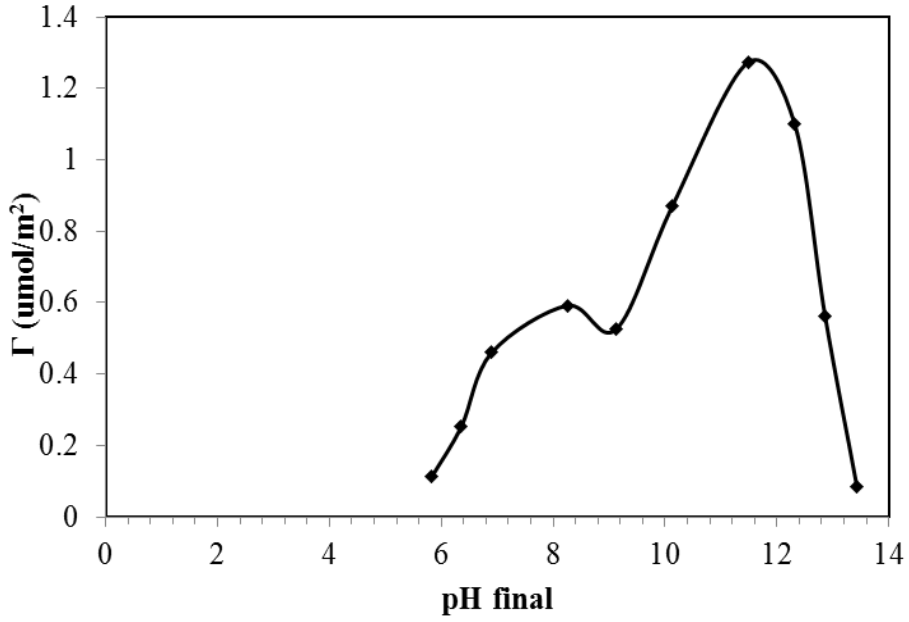

Figure 2.4: Uptake survey for 4wt% Pd/SiO_2.

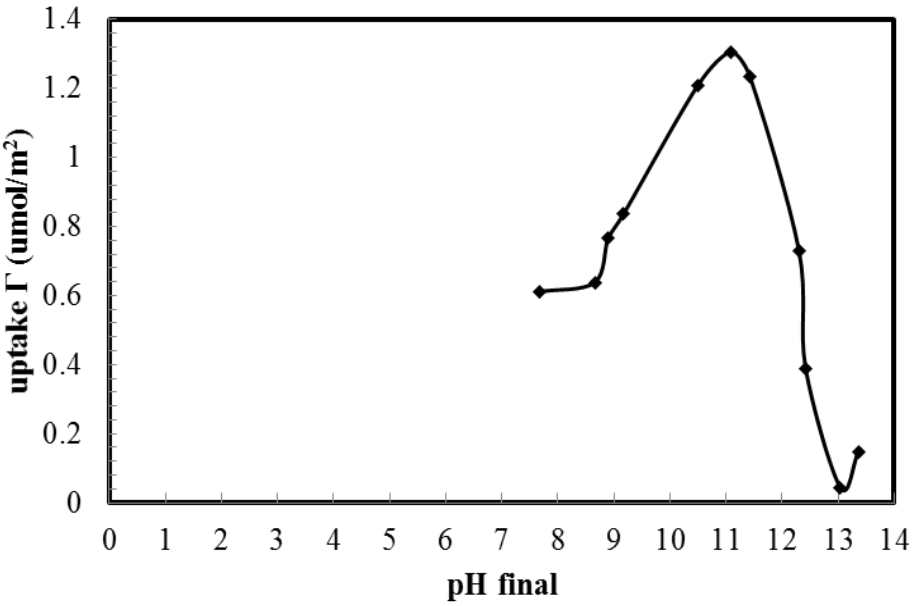

Figure 2.5: Uptake survey for 2.3wt% Pd/TiO_2.

2.3 CATALYST CHARACTERIZATION

2.3.1 PULSE H_2-CHEMISORPTION (HYDROGEN TITRATION OF OXYGEN PRE-COVERED CATALYST)

The catalyst dispersion was determined by pulse hydrogen chemisorption technique using a Micromeritics 2920 AutoChem II Analyzer. This technique can determine the active surface area, metal dispersion, and the average particle size by applying measured doses of reactant gas to the sample. There are three different methods consisting of: the static volumetric, the static gravimetric and the flow method (pulse chemisorption). The latter is utilized for this analysis. This method can determine strong interactions that exist between the reactive gas and the active phase. The gases that exit the sample, is sent through a thermal conductivity detector (TCD) to establish a baseline response. Once a known quantity of the reactive gas is determined, the gas is removed from the stream depending on the amount of unoccupied active sites that adsorb the gas and hence diminishes the quantity that reaches the detector. The gases are injected subsequently as pulses until the surface of the sample saturates and two successive peaks display the same area [91]. Figure 2.6 illustrates the sequence of the of peak area of the reactive gases detected by TCD.

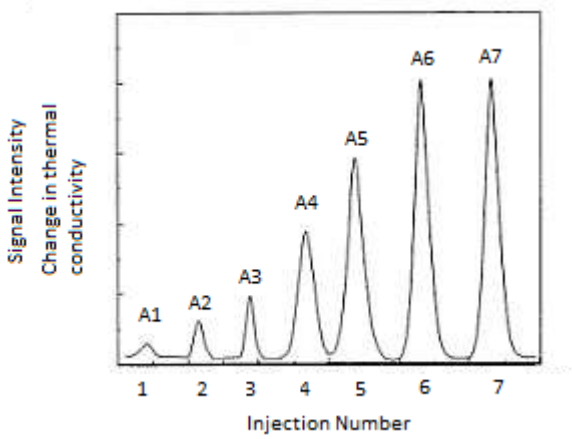

Figure 2.6: Pulse chemisorption adsorbed peak as a function of the injection number.

The reactive gases used in chemisorption should be chosen depending on the active phase of the catalyst. Therefore, a stoichiometric relation between the gas and the metal should be determined accurately since the chemisorption measurement depends on the gas amount that is absorbed or desorbed. Table 2.7 summarizes the common stoichiometric factors for the different types of reactions [92]. For example, for H_2-chemisorption, half of a hydrogen molecule is absorbed on the active site of the metal. Hence, the stoichiometry factor assigned to the Micrometrics analyzer should be 2. However, some catalysts can experience hydrogen spillover, a phenomenon that can induce the migration of hydrogen onto a second phase (usually the support) that do not react if present alone in the same conditions. This phenomenon is not desired since it results in overestimation of the amount of hydrogen adsorbed or desorbed on the active phase [93]. However, the spillover phenomena may be favorable in a catalytic reaction since it may effectively increase the number of active sites (i.e. Pt/TiO_2 HDO reactions). Figure 2.7 demonstrate an example of hydrogen spillover on a surface metal.

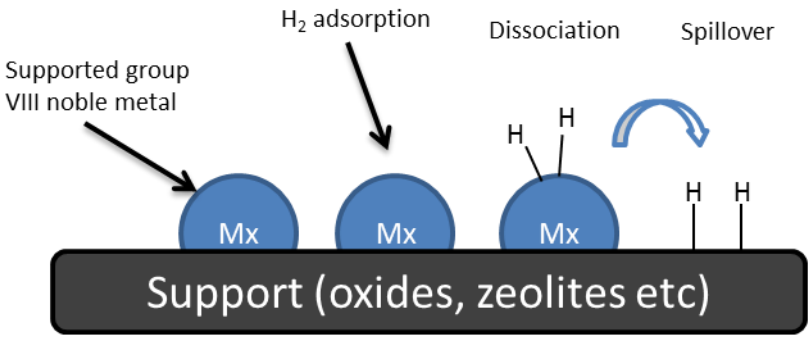

Figure 2.7: Hydrogen spillover over supported Mx.

For the experimental setup, the catalyst is placed in an enclosed compartment (sample holder or reactor) where the gases will react with the active site of the metal until all sites are occupied. The injected gas volume of the sample is recorded. Thus the amount of gas chemisorbed gas becomes the total amount of the gas injected minus the amount that emerged from the sample. The gases utilized were UHP grade consisting of: Ar, He, 10% H_2/Ar, 10% O_2/He. The first three gases contained Restek moisture and oxygen traps, meanwhile, the latter contained only a moisture trap. Prior to running the chemisorption, the catalyst (0.1-0.2 g) was loaded in quartz U-tube reactor packed with quartz wool. The catalysts were reduced as explained before for 2 hours, followed by purging with Ar for 2 hours, and then cooling to 40 ºC. For Pd, Pt, Rh and Ir, the conventional hydrogen chemisorption method was utilized. For Ru and Ni a customized hydrogen chemisorption method was implemented since the catalyst needs to be reduced and treated at different conditions. The latter catalysts are oxyphilic and are oxidized if exposed to air at room temperature. Therefore high temperature reduction is required. However, if the temperature is too high (>400ºC), sintering of the catalyst occurs, leading to lower dispersion.

Table 2.7: Stoichiometry factors for the chemisorption methods analyzed.

Method	**Reaction (Mx = active site of metal)**	**Stoichiometry factor**
Hydrogen chemisorption	$Mx + ½\ H_2 \rightarrow Mx\text{-}H$	0.5
Hydrogen/oxygen titration	$Mx\text{-}O + 3/2\ H_2 \rightarrow Mx\text{-}H + ½\ H_2O$	1.5
Oxygen/hydrogen titration	$Mx\text{-}H + ¾\ O_2 \rightarrow Mx\text{-}O + ½\ H_2O$	0.75

For the conventional method, after pretreatment, the catalyst was exposed to H_2 by pulsing 10% H_2/Ar at 40 ºC. During this step H atoms were absorbed on the active surface site. Then, 10% O_2/He is applied for 30 min and purged with Ar for 30 min. The oxygen reacts with the adsorbed H atoms to produce H_2O (g). However, the oxygen atoms are adsorbed on the active site, therefore, the sample was titrated with pulsations of 10% H_2/Ar until no changed in the peak area was detected. Then the sample was flushed with argon and the experiment concluded.

For the customized method, the sample underwent the same pre-treatment; however no H_2-chemisorption at 40 ºC was done. After being exposed to Ar, the sample was heated up to 100ºC by temperature programmed oxidation temperature, where the oxygen uptake temperature was determined. Then, the sample temperature was raised up to 498 K and flushed with Ar for 30 minutes, prior being exposed to 10% H_2/Ar. After O_2-H_2 titration, the sample was cooled and flushed with argon. The customized method was designed for

Ru and Ni catalyst, where the reduction temperatures are higher than room temperature. The active surface is covered with oxygen (instead of bulk oxygen) and then is titrated up to the corresponding reduction temperature. Table 2.8 summarizes the stoichiometry factor, dispersion, and estimated particle diameter of the catalysts tested. The H_2-chemisorption and O_2-H_2 titration gave similar results; however, the results were more reproducible using the titration methodology. Cobalt and iron were not analyzed by chemisorption since the reduction temperature are too high and can harm the equipment.

Table 2.8: Catalyst analyzed by chemisorption and the dispersion and physical properties.

Catalyst	**10% H_2/He titr. temp. (ºC)**	**Stoichiometric factor O_2-H_2 titr.**	**Disp. (%)**	**Part. Size (nm)**
1.86wt% Pd/SiO_2	40	0.67	7.8	14.4
1.67 wt% Pt/SiO_2			11.7	9.7
2.0 wt% Rh/SiO_2			21.0	5.3
5.0 wt% Pd/C			16.9	6.6
4.0 wt% Pt/TiO_2			45.2	2.5
2.0 wt% Ir/SiO_2			0.98	113.9
2.0 wt% Ru/SiO_2	250	0.40	6.7	19.9
2.0 wt% Ni/SiO_2	300	0.40	4.5	22.6
2.0 wt% Pd/γ-Al_2O_3	40	0.67	7.1	15.7
2wt% Pd/SiO_2 (N)			0.90	125.08
2wt% Pd/SiO_2 (Cl)			7.86	14.25

High temperature pre-treatment and reduction conditions could promote the sintering and poisoning of the catalyst. Sintering of a metal catalyst is known as the process where the temperature, time and ageing can cause the metal atoms to agglomerate and form larger particles. The pre-treatment and reduction of a catalyst should be made in such a way that all contaminants are removed at a certain temperature; however the temperature does not overtake the limit. If the metal forms large aggregates the dispersion is significantly lowered. Unfortunately, the phenomenon is irreversible and the original conditions of the catalyst will not be restored. This is the case of Ir, Ru and Pd/Al_2O_3 catalyst (as shown in the table above) where the dispersion significant decreased because of the pre-treatment they were exposed to. The reduction temperatures were determined based on the reaction conditions, to estimate the actual metal dispersion during the catalyst activation. Poisoning is also a common problem, and refers to an impurity present in the fluid phase that reacts selectively on some active sites, thus decreasing the activity. The formation of by-products can occur when the catalyst is poisoned. An example of poisoning could be coke formation in a reaction catalyzed by Pd/C. The coke could affect the reaction by favoring the methanation reaction.

2.3.2 Atomic Absorption (AA) Spectroscopy Study: Aqua Regia Digestion and Sodium Peroxide (Na_2O_2) Fusion

In order to determine the actual metal loading for Ru/SiO_2 and Pt/TiO_2 catalysts, Atomic Absorption Spectroscopy (AAS) experiments were conducted [94]. A sample of Ru/SiO_2 (11.0-13.0 mg to obtain the corresponding PPM) was diluted in aqua regia consisting of a mixture of nitric and hydrochloric acid (36%) with a volumetric ratio of 1:6 respectively. The samples were digested in the oven at 120 ºC for 5-7 hours, followed

by cooling and dilution with 10% HCl/0.5% $LaCl_3$ solution up to a volume of 25 mL. An aliquot of the solution was separated in a 12 mL vial and set up for AAS experiment. 4.0 wt% Pt/TiO_2 samples were also analyzed following similar procedure. Unfortunately, aqua regia was not able to dissolve the metal completely, therefore sodium peroxide fusion experiments were conducted for Ru and Pt catalyst [95]. Similar amounts of Ru and Pt (about 12.0 mg) catalysts were mixed with sodium peroxide (Na_2O_2), and placed in a zirconium crucible. The crucible was then exposed to a flame until the cake became red. The cake was cooled and 2 mL of 10% HCl-0.5% $LaCl_3$ was added to the cake, and then transferred to a Teflon tube where it was heated in the oven at 120 ºC for 3-4 hours. The AAS experiment followed the same procedure depicted above.

The atomic absorption analyses were conducted using a Perkin Elmer 3300 (series # 037N3041401) instrument. An acetylene/air flame was used for all analyses. A cathode lamp is a stable light source that is able to emit the corresponding wavelength of light corresponding to the element to be analyzed. The VWR scientific lamps characteristic for Ru and Pt are mA Op. current=7 to max current=10, and mA Op. current=8 to max current=12, respectively. For each metal, a calibration curve was prepared utilizing standards previously prepared. For Ru the calibration curve was done with 1.0, 5.0, 10.0, 16.0 and 20.0 PPM standard solutions. For Pt, 1.0, 5.0, 10.0, 15.0 were used. Secondary source solutions were also prepared in order to verify the calibration curve. For Ru catalyst the weight loading for the aqua regia and sodium fusion experiments were 1.39 and 1.64 wt% respectively. The percent recovered was 69 and 83 respectively. For Pt the results were 3.31% and 3.04% with a percent recovered of 82

and 79 respectively. Interestingly, the sodium fusion was more effective on Ru that on Pt catalyst.

2.3.3 Temperature Programmed Oxidation and Reduction TPR/TPO

Temperature programmed oxidation and reduction experiments were carried out using a flow system coupled to an Inficon Transpector 2 (model: TSPTT300) pumped by Pfeiffer (model: MVP 015-2) vacuum pump. The main purpose of these measurements was to find the most efficient reduction temperature before analyzing the catalyst with chemisorption. For TPO, a catalyst that is in the reduced state is exposed to a programmed temperature rise where a mixture of oxygen/helium is flowed over the sample. The amount of oxygen consumed during the reaction is related to the amount of reducible species on the surface or how much metal is oxidized. For the TPR technique, the oxidized catalyst is also exposed to a programmed temperature rise while the reducing gas mixture (hydrogen/argon) is flowed over the sample. The mass spectrometer measures the signal mass/charge ratio of the molecule. The oxidation or reduction process is determined by monitoring the H_2, H_2O or O_2 signal during the experiment. The mass spectrometer can also monitor other residual components resulting from the precursor decomposition such as nitrides or chlorides.

The sample is placed in a Pyrex or quartz reactor (attached to a sample holder) connected to a gas manifold that delivers 10% H_2/Argon, 10% O_2/Helium, as well as UHP H_2, O_2, He and Ar. The catalyst in the oxidized form, is first reduced *in-situ* with pure hydrogen (5ºC/min) to obtain the active metal zero valence form up to the corresponding reduction temperature, and then cooled to room temperature under inert argon flow. The total flows of the reactive gases were specified to be 50 sccm. The catalyst was then

exposed to 1% O_2/He in a temperature rise program and the signal output of O_2, and H_2 were monitored. It is crucial to make sure that the catalyst does not form bulk oxide, but rather simply adsorbs oxygen atoms onto the active metal surface. Therefore, the TPO experiments should be carried out at room temperature or at mild temperatures up to 100 ºC. Afterward, the sample is cooled under Ar to room temperature. Then, the sample is exposed to 1% H_2/Ar up to the reduction temperature or until a H_2O peak or H_2 uptake is detected by the mass spectrometer. During the whole experiment, the vacuum pressure was always maintained at 1.0E-06 mbar and monitored constantly, especially when changing the reactive gases.

2.3.4 BRUNAUER–EMMETT–TELLER (BET) MEASUREMENTS

The total BET surface area (m^2/g) of γ-Al_2O_3 and carbon support were determined by the ChemBET -3000 TPR/TPD (Quantachrome Instruments) coupled with a linear mass flow controller. The BET technique determines the physical adsorption of an inert gas on the surface of the solid sample. The amount of gas absorbed at a given pressure gives the surface area. The experiments were carried out by placing ~0.05 g of the support in the Pyrex reactor. The sample was pre-treated by flowing He at 250 ºC for about 2 hours to remove the remaining water and impurities. Afterward, the support was exposed to mixtures of nitrogen (10, 20 and 30%) balance He. The sample was cooled over liquid nitrogen and a thermal conductivity detector measured the absorbed and desorption peaks. A calibration peak was determined by injecting manually specific volumes of N_2 in the calibration port. The calibration peak should be about the same concentration as the desorption peak. Once the single BET points are collected the software computes the multipoint BET surface area and prints a report. The BET technique is based on the

assumption that the surface is homogenous and there is no lateral interaction between the molecules. In addition, the first adsorbed layer is determined by the heat of adsorption and the higher layers by the heat of condensation. The results obtained are summarized in the materials section (3.1, table 3.4).

2.3.5 FOURIER TRANSFORM (FT-IR) SPECTROSCOPY

Fourier transform-infrared (FT-IR) spectroscopy studies were carried out by the Nexus 470 spectrometer. The data was analyzed with OMNIC (version 7, Thermo Electron Corporation) software. The adsorption of PAc over Pd/SiO_2 and the corresponding SiO_2 support were analyzed in order to determine which functional group is adsorbed on the active phase of the catalyst. The catalyst was ground prior to the preparation of the pellets. The pellets with 0.029 g of catalyst were ground in a Carver Model C laboratory press. The FT-IR detector was cooled with liquid nitrogen before gathering the FT-IR spectra. The catalyst was placed in an enclosed cylindrical shape cell. A line attached to a VLE saturator containing PAc was attached to the FT-IR, to pulse a minor concentration of PAc (~0.13%) to the detector. The temperature of the VLE was kept to 0ºC while flowing 20 sccm of sweep He, followed by adding diluent He to a total of 50 sccm flow. As shown in Figure 2.8 the gases mixed before entering the reactor where, a three way valve was placed before the T connector to suppress the PAc vapor flow. A pressure gauge and shutoff valves were installed to ensure proper sealing of the flow cell. The cell was connected in such a way that the 50 sccm of gas flow enter before and exit after the sample pellet. The cell was heated utilizing a heating tape (max. temp. ~275 ºC) carefully wrapped around the cell. The temperature was controlled by a Variac by changing the voltage until desired temperature was reached. A thermocouple was installed in the flow cell inside a metal

connector on the pellet holder. The catalyst was reduced up to 275 ºC in H_2 (UHP) for 2 hours and cooled to room temperature in He (UHP). The catalyst and the support were placed in the same unit cell and a background spectrum flowing He was acquired for both samples. Once the VLE saturator reached a steady temperature and the experiment was setup, the samples were exposed to pulses of PAc that lasted about 3 minutes. Then, the flow was stopped by changing the 3-way valve to vent. Afterward, FTIR spectra were taken using 10 scans at 2.0 resolutions, followed by purging the sample with 1 minute of helium flow. Figure 2.9 shows the program of PAc pulses and the purge of He. The spectra collection was alternated in such a way that the proper background spectrum was referenced. Therefore, the cell was moved manually between the catalyst and the support right after they were exposed to the pulses of acid. The pulses were done until no significant changes in the spectra were detected. Spectra were analyzed by subtraction and by peak analysis available in the software. Results from the experiments are summarized in Appendix A.1

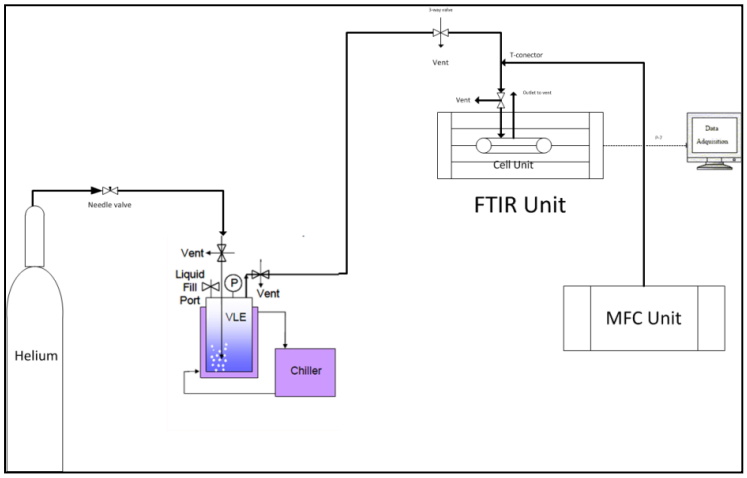

Figure 2.8: Experimental setup for the FT-IR spectroscopy of PAc over Pd/SiO_2 and SiO_2.

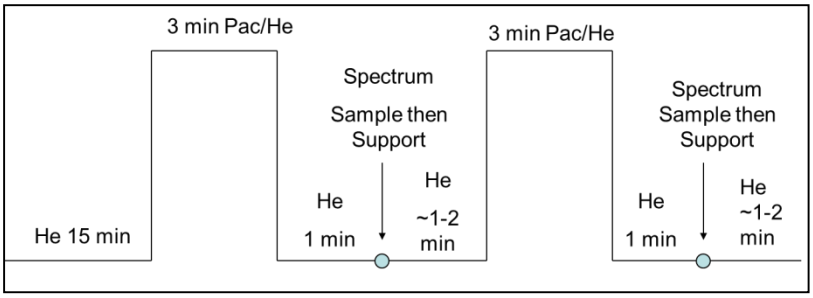

Figure 2.9: Diagram of programmed pulsed of PAc and He.

2.3.6 GC-MASS SPECTROSCOPY (MS) ANALYSIS

Diethyl ketone and propanoic acid, propanoic acid-propyl ester were detected utilizing Gas chromatography–mass spectroscopy (GC-MS). The analytical method combines the techniques of mass spectrometry and gas phase chromatography. The gas chromatogram separates the organic mixture in the sample and the mass spectrometry characterizes each substance. Additionally the technique can determine the concentration of each of the substances present. For the GC, the components are usually detected by FID and/or TCD. For mass spectroscopy, the molecules are electrically charged, accelerated through a magnetic field and hence breaks the molecule into different fragments displayed as a plot of the different masses. Therefore, the different masses are quantified together and a mass of the original substance is obtained.

The sample was gathered from the outlet of the reactor. A condenser attached to the line collected a small amount (~2mL) of the reaction product. The condenser had to be cooled below 0 ºC with liquid nitrogen (-196 ºC) to ensure all the gaseous products were condensed. The samples were analyzed in the chemistry department GC-MS lab by Mike Walla. The capillary column utilized was the Rtx-5 (temp range: -60-350 ºC). The samples were dissolved in pure acetone and a sample from the headspace was injected to the GC-

MS. The results concluded that the two unknown products from the PAc reaction belonged to diethyl ketone and propanoic acid, n-propyl propionate.

2.3.6.1 MS-RESIDUAL GAS ANALYZER (RGA)

For the MS experiments discussed in chapter 5, the products were diluted with argon carrier gas at approximately 35 ccm as measured by a digital flowmeter (ADM 2000, Agilent technologies). Sampling was done with a transfer capillary column of 25 micrometer i.d. (SGE) mounted onto the stainless steel (SS) stream tubing with a SS tee (Swagelok) and a reducing fitting with a bored Vespel-graphite ferrule (SGE). The other end of the capillary was mounted with VCR fittings and Vespel-graphite ferrule onto a vacuum chamber built with SS Conflat flange (CF250) parts (Duniway). The capillary was mounted at the top of the vacuum chamber in a cross configuration to provide accurate sampling with the gas analyzer to the left, the turbomolecular pumping station (Pfeiffer model TSH071E) beneath, and a Pirani/cold cathode full-range gauge (Pfeiffer model PKR251) to the right. The RGA used was a Stanford Research Systems RGA100 with an electron multiplier and accompanying software. The sampling rate was 3 sec for pressure vs. time measurements and the rate of intensity vs amu scans was 8 sec per 0-63 amu. Typical pressures in the chamber were 3-5 x 10^{-7} torr.

2.3.7 POWDER X-RAY DIFFRACTION (XRD)

The X-ray diffraction (XRD) patterns were recorded using a Rigaku Ultima IV diffractometer system with a D/tex Ultra detector with Cu Kα radiation (λ = 1.54 Å). Data were collected from 10-80º 2θ with a step size of 0.04º and a scan rate of 1º/min. Particle size was estimated using the Scherrer equation with LaB6 (NIST SRM 660a) as a reference

for instrumental broadening. The XRD particle sizes were estimated for Pd-2, Pd-6 and Pd-10 for both the fresh and spent catalyst by using the Scherrer equation which is defined as:

$$d = \frac{K\lambda}{\beta \cos(\theta)}$$

Where d is the particle diameter, λ is the wavelength of the incident radiation, θ is the Bragg angle, β is the full width at half maximum (FWHM) of the diffracted peak, and *K* is the shape factor of the particle which is designated to be 1.0 for spherical particles, but could have values as low as 0.73 for triangular shaped particles.

2.3.8 TRANSMISSION ELECTRON MICROSCOPY (TEM)

Scanning transmission electron microscopy (STEM) was performed on a JEOL 2100F 200kV FEG-STEM/TEM equipped with a CEOS C_s corrector on the illumination system. The geometrical aberrations were measured and controlled to provide less than a π/4 phase shift of the incoming electron wave over the probe-defining aperture of 17.5 mrad which at 200kV provides a nominal probe size of <0.1nm. High angle annular dark-field (HAADF) STEM images were acquired on a Fischione Model 3000 HAADF detector with a camera length such that the detector spanned 50-284 mrad. The scanning acquisition was synchronized to the 60 Hz AC electrical power to minimize 60Hz noise in the images and a pixel dwell time of 15.8μs was chosen. Histograms of the particle size distribution were obtained by measuring particles from at least six different micrographs for any sample analyzed and are discussed in chapter 4.

2.4 CATALYST EVALUATION

2.4.1 PROPANOIC ACID HYDRODEOXYGENATION: PLUG-FLOW REACTION SYSTEM

The catalysts were evaluated in a single pass, packed bed, plug flow reactor system. The reactor consisted of a stainless steel (SS) reactor (5.68 mm I.D, 9.52 mm

O.D) attached to a vertical split-tube furnace (Applied Test Systems Inc, 15" Series 3210, 1210 W, 115 V) with a maximum temperature capacity of 100ºC (controlled by Thermo Electric Instruments). The reactor was loaded with ~0.20-0.30 g of catalyst supported on glass wool and a 4.76 mm O.D, 127 mm length stainless steel tube. A thermocouple was inserted in the middle of the reactor in such a way that is close to the catalyst bed but does not come in contact with it, to offer an accurate reaction temperature. The catalysts were reduced *in-situ* at temperatures ranging from 200-400 ºC in 20% H_2 balance He (50 sccm total flow) for 2 hours followed by cooling to room temperature in helium. The flow of hydrogen and helium were controlled utilizing *Tylon* mass flow controllers (MFC). The feed stream for the reaction consisted of 0.8-1.5% PAc, 20% H_2/balance He. The pressure remained constant at 1 atm. The liquid reactant (PAc) was stored in a jacketed vapor-liquid equilibrium (VLE) saturator attached to a recirculating ethylene glycol (diluted in water) refrigeration system to control the temperature (VWR 1145). Propanoic acid was loaded into the VLE through the liquid fill port. Controlled flow of helium (sweep gas), was supplied to the VLE beneath the liquid level to create bubbles in the liquid. Overhead of the liquid level, PAc and He vapor reached a thermodynamic equilibrium state. The Helium saturated with PAc exited at the top of the VLE and mixed with the diluent gas stream. The VLE temperature was monitored and controlled so that the desired PAc concentration was attained.

The calculations of composition of PAc were determined by the USC Antoine equation (Figure 2.10). Undesired condensation of the feed lines was prevented by wrapping them with heating tape and keeping them at 125ºC. Heating tapes were regulated by a Variac (Staco energy products Co. Input: 120V, 50/60Hz). Figure 2.11

illustrates a schematic of the reactor system including the MFC, the VLE, the valve box and the GC inlet. The sweep gas coming from the VLE and the diluent gases coming from the primary manifold are mixed prior to entering the reactor. The valve box (Vici Valco Instruments Inc.), consists of a series of valves connected that direct the feed and product gas stream, where a sample is collected for the GC. The valve box and the lines connected to the GC are maintained at 100ºC by a Furotherm 91e temperature controller. The reaction feed and product were analyzed utilizing an on-line Hewlett-Packard 5890 gas chromatograph with two 30 m HP-PlotQ capillary column for the product detected by the flame ionization detector (FID) and thermal conductivity (TCD). In addition, to HDO of PAc, CO hydrogenation experiments were carried out to determine whether methanation is significant under the reaction conditions utilized. The 1% CO/He (UHP) cylinder was connected by replacing the He line (attached to the MFC), to an external line connected to the cylinder (as specified in Figure 2.11). The deuterium labeled PAc experiments (chapter 5) were conducted by adding a second VLE (2), with a chiller and connecting the lines to run the unlabeled and labeled PAc experiments at the same time. A residual gas analyzer is connected to the product venting lines to carry out the deuterium product labeled experiments. Figure 2.12 depicts a picture of the plug flow reaction system coupled with the GC and VLE.

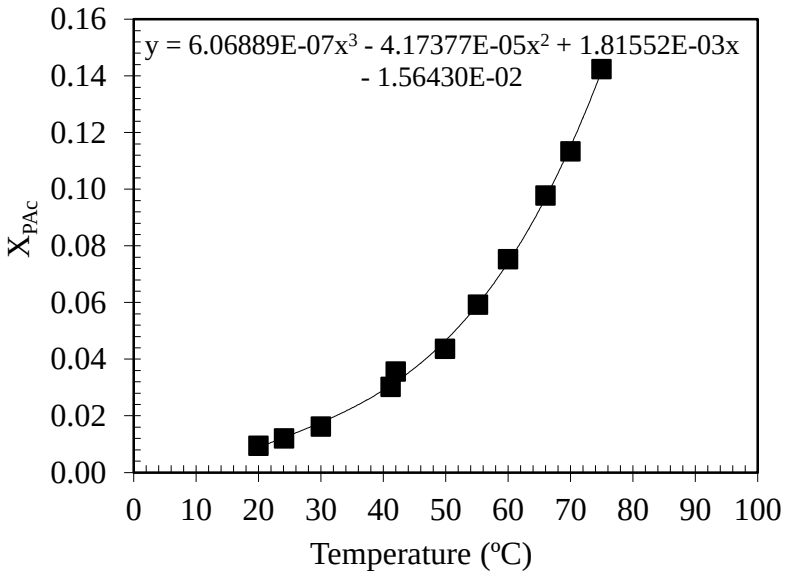

Figure 2.10: USC Antoine's estimation for the concentration of propanoic acid in the reaction system.

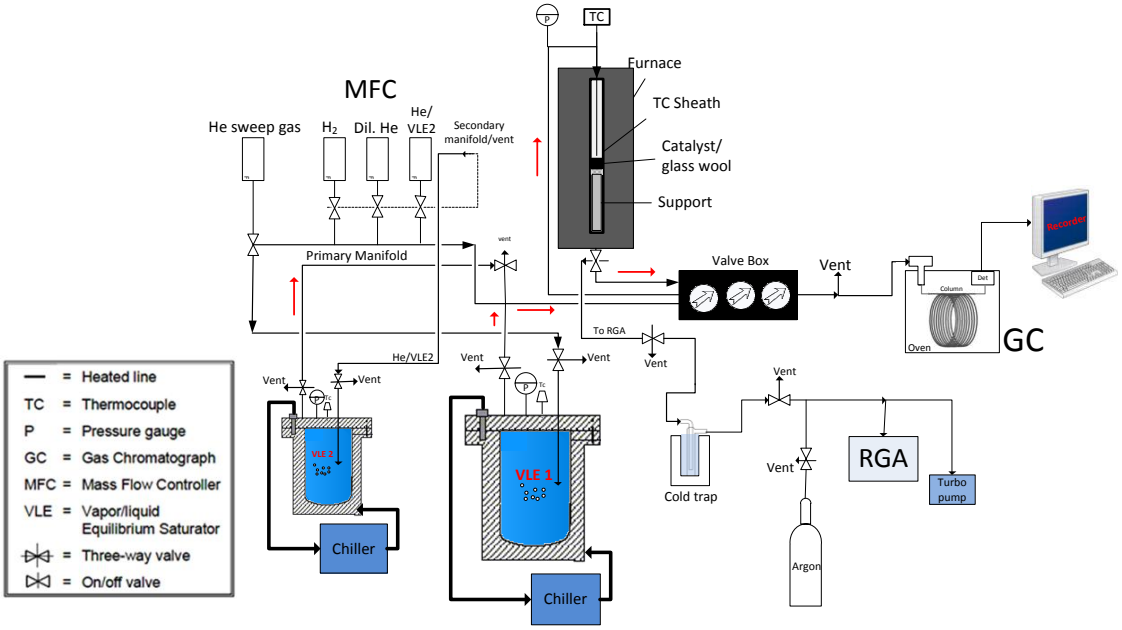

Figure 2.11: Schematic of the gas-phase plug-flow reactor system coupled with a GC system and a residual gas analyzer.

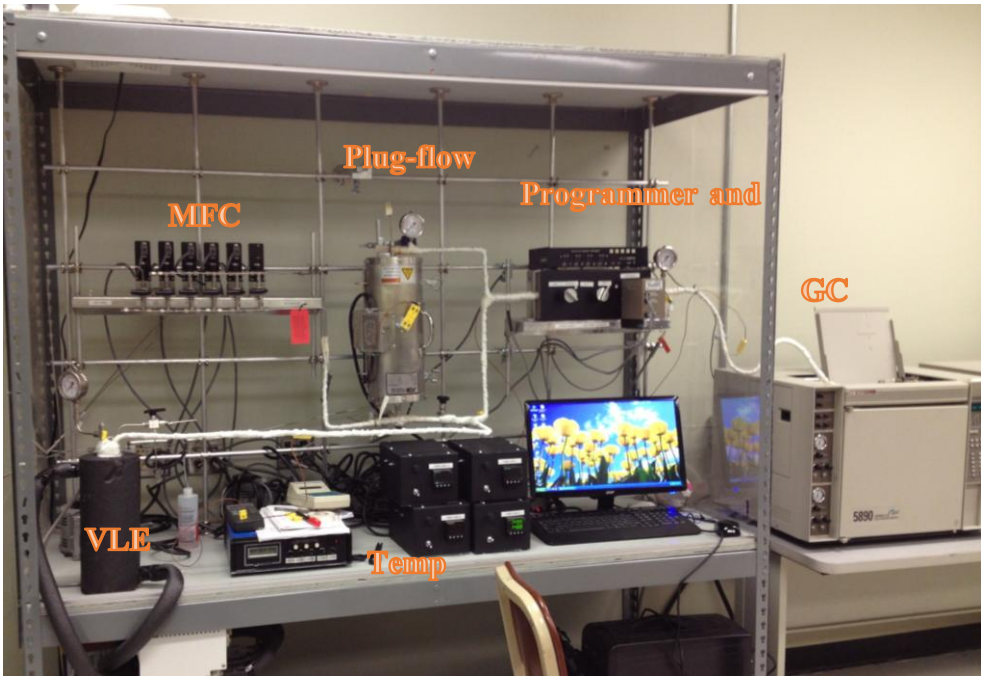

Figure 2.12: Picture of the continuous plug-flow reactor system.

The feed/products were analyzed by gas chromatography where the temperature ramp was set up for the peaks to come out gradually at a reasonable retention time. The chart speed, attenuation, peak width was specified, prior running the reactions. Figure 2.12 shows the reaction ramp utilized for this column. Propanoic acid, 1-propanol and propionaldehyde were calibrated by varying the temperature of the VLE for the different concentration (0-450 nmoles). The estimated nmoles was calculated by the USC Antoine equation and revised with the $loop\ capacity = [nmoles\ of\ gases\ injected] \times y_{PAc}$ (estimated based on the flow rate of the sweep and diluent gas). Diethyl ketone was calibrated by liquid phase injection using a 5 mL syringe (Hamilton 81520) and pump (New Era Pump Systems, model: NE-1000) attached to the lines connected before the valve box at different volumetric flow rate. The calibration graphs for the feed and product for the FID and TCD columns are shown below. The paraffins and olefins response factor were

determined by flowing the gases for a period of time and obtaining the integration area counts $R.F = \frac{nmoles\ X}{Int\ Area\ counts}$. The calibration curves, the retention time and response factor for each reactant and product are shown in appendix A.1.

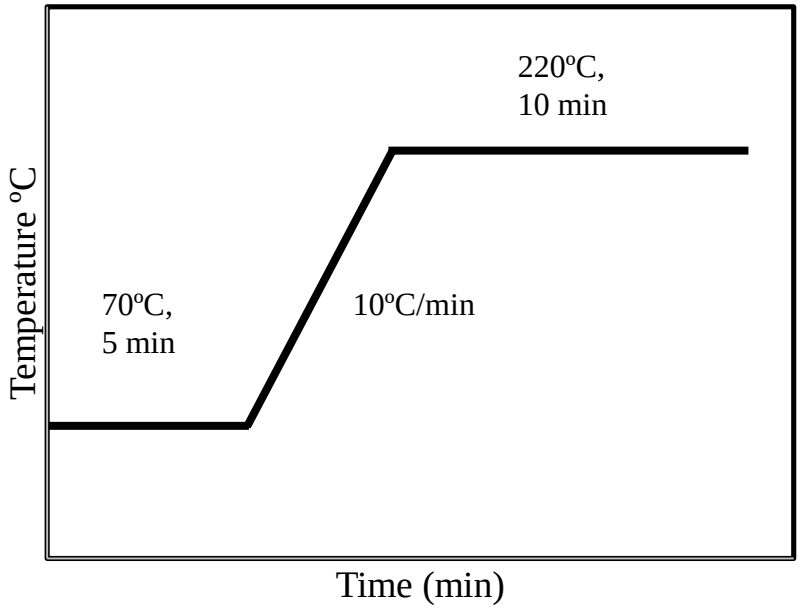

Figure 2.13: Programmed temperature ramp for the gas chromatography.

CHAPTER 3

GAS-PHASE, CATALYTIC HYDRODEOXYGENATION OF PROPANOIC ACID, OVER SUPPORTED GROUP VIII NOBLE METALS: METAL AND SUPPORT EFFECTS

3.1 INTRODUCTION

The demand of energy is increasing constantly and the United States is dependent on foreign sources for about half of its fuel consumption [96]. The combustion of fossil fuels releases carbon dioxide, a major greenhouse gas, into the atmosphere contributing to the problem of global warming. This factor, along with the increasing demand for fossil fuels coupled with the decreasing availability of those resources, has prompted a move towards alternative energy production and utilization[1, 2]. New research efforts promise to bring advances in a variety of areas, and biomass conversion to fuels and chemicals will play a critical role in the future.

Industrial processes for converting biomass into biofuels include gasification to syngas (leading to liquid fuels through FT synthesis), pyrolysis to produce bio-oil, and hydroprocessing to remove oxygen functionality[97-99]. During these processes, carbon dioxide is released as well; however, the emission gases are balanced largely by the carbon dioxide that is captured during the growth of the biomass, depending upon how much energy was used to grow, harvest and process the fuel [100]. Feedstocks derived from lignocellulosic substances contain great amounts of oxygen such that the C:O ratio approaches unity. However, the fuel and chemical products derived from such feedstocks must have an oxygen content less than about 5.0% to be commercially viable [23, 101].

Heterogeneous, catalytic deoxygenation (including hydrodeoxygenation) is one of the most promising processes for generating hydrocarbon fuels from biomass. During hydrodeoxygenation (HDO), hydrogen is co-fed with the reactant to facilitate hydrogenolysis (HYS) and hydrogenation reactions required for the removal of oxygen.

During the 1980's, Maier et al. studied the gas-phase decarboxylation of short chain carboxylic acids to hydrocarbons using Ni and Pd catalysts [13]. However, most of this work focused on C-C bond scission rather than removal or hydrogenation of the C=O bond. Since then, increasing amounts of research have been conducted in the area of biomass-derived platform molecules such as organic acids and esters (e.g., palmitic, oleic and stearic acid, ethyl stearate and tristearine) via decarboxylation and hydrogenation reactions on monometallic and bimetallic catalysts [10, 42, 44-51, 102-109]. For example, Murzin and co-workers have focused on biomass- derived, liquid-phase hydrogenation on supported palladium catalysts [14], while Resasco and Lobban reported the direct conversion of triglycerides to olefins and paraffins over Pt/Al_2O_3, Pt/SiO_2, and $PtSnK/SiO_2$ catalysts [110]. Additionally, Kozhevnikov et al. recently reported studies on heteropoly acid and bifunctional metal-loaded heteropoly acid catalysts for the deoxygenation of PAc [111].

The present work aims to explore the catalytic chemistry of the HDO of PAc (a model compound for aliphatic organic acids) over supported group VIII noble metal catalysts. The monometallic catalysts have been selected based on their potential to catalyze different bond breaking events relevant to the above reactions. The catalysts include Pd, Pt, Ru, Rh and Ni supported on SiO_2. Additionally, Pd was screened on different supports (i.e. carbon, SiO_2, and TiO_2), to investigate the influence of the support material on activity, selectivity and activation energy. These studies provide insight on the

different reaction pathways to form paraffins/olefins or oxygenated products from biomass derived organic acids.

3.2 Experimental Methods

3.2.1 Catalyst synthesis (M/SiO_2)

For the screening reaction on M/SiO_2 (M = Pd, Ru, Ni), the catalysts were synthesized by incipient wetness utilizing aqueous solutions of the following metal salts: palladium nitrate hydrate ($Pd(NO_3)_2 \cdot xH_2O$, 99.9 Sigma-Aldrich), ruthenium nitrosyl nitrate ($Ru(III)(NO)(NO_3)_3$, 31.3% min Alfa Aesar) and nickel perchlorate hexahydrate ($Ni(II)(ClO_4)_2 \bullet 6H_2O$, 99.99% Alfa Aesar). The SiO_2 support (Silica Star, S_{BET} = 100 m^2/g) and the commercial catalysts of 2.14wt% Pt and 2.06wt% Rh over SiO_2, were obtained from BASF. In addition, a 4.0 wt% Pd catalyst with a different SiO_2 support (Aerosil 300, S_{BET} = 330 m^2/g, Evonik) was synthesized by strong electrostatic adsorption (SEA) as described in chapter 2 section 2.2.3. The catalysts prepared by SEA or incipient wetness were dried overnight at 70 ºC, followed by calcination in air and reduction with 100% H_2 at their respective temperatures for 2 hours (see Table 3.1). The exception was the 4 wt% Pd/SiO_2, which was not subjected to a calcination step due to the fact that the 1.1 wt% Pd/SiO_2 catalyst exhibited very large particle size. The commercial catalysts were already prepared, and therefore it was decided that no calcination step was required.

3.2.2 Catalyst synthesis (Pd/X)

Three different palladium catalysts were investigated for the detailed kinetics of the HDO of PAc: 4.0 wt% Pd/SiO_2 (Aerosil 300, S_{BET} = 330 m^2/g, Evonik), 5.0 wt% Pd/C (CP-97, S_{BET} = 615 m^2/g, commercial BASF catalyst) and 2.3 wt% Pd/TiO_2 (TiO_2, S_{BET} =

46.06 m^2/g, Evonik). The Pd/SiO_2 and Pd/TiO_2 catalysts were synthesized by SEA, while the commercial Pd/C was supplied by BASF and followed the same procedure described in the previous section.

Table 3.1: Physical and chemical properties of M/SiO_2.*Pd/SiO_2 synthesized by SEA.

Metal loading (wt%)	**Catalyst Mx/SiO_2**	**Calcination temp. (ºC)**	**Reduction temp. (ºC) 100% H_2**	**Dispersion (%) O_2-H_2 titr.**	**Particle Diameter (nm)**
1.1	Pd	300	350	3.9	31.4
4.0	Pd*	-	350	55.0	2.0
2.1	Pt	-	300	11.7	9.7
2.2	Rh	-	300	21.0	5.3
1.6	Ru	300	300	11.7	11.4
1.8	Ni	450	450	4.8	22.6

3.2.3 PULSED H_2 CHEMISORPTION

The metal dispersions of the catalysts were determined by pulsed hydrogen titration of oxygen pre-covered sites using a Micromeritics 2920 AutoChem II Analyzer. Prior to the analysis, the catalysts (0.1-0.2 g) were reduced in flowing 100% H_2 for 2 hours, followed by purging with Ar for 2 hours to remove any physisorbed hydrogen. After cooling to 40 ºC in flowing Ar, the catalysts were exposed to 10% O_2/He for 30 min followed by purging with Ar (30 min). Titration with pulses of 10% H_2/Ar was then employed until no further H_2 uptake occurred. This method was applied for Pd, Pt, and Rh based catalysts. For Ru and Ni, a modified hydrogen chemisorption method was implemented. The sample

experienced the same pretreatment described previously; however no H_2-chemisorption at 40 ºC was done. After being exposed to argon, the sample was heated up to 100 ºC by temperature programmed oxidation, following by flushing with argon for 30 minutes. Then, the sample temperature was raised up to 225 ºC and exposed to 10% H_2/Ar. This titration temperature was confirmed based on the results of temperature programmed oxidation/reduction described in appendix B.2. Additional XPS analyses were performed for Ni/SiO_2 also described in appendix B.1.

3.2.4 HDO OF PAC OVER M/SiO_2: CATALYST EVALUATION

All activity and kinetics measurements for the HDO of PAc were carried out under atmospheric pressure. The experiments were carried out in a single pass, packed bed, plug flow reactor system. The catalysts were reduced *in-situ* at temperatures ranging from 200-400 ºC at a total flow of 50 sccm H_2 for 2 hours at 1 atm pressure. The reduction temperature was chosen depending on the different reduction treatments required for each metal (Table 3.1). The feed stream for the screening experiments consisted of 1.0% PAc (Alfa Aesar, 99%) and 20% H_2, balances He. For the kinetic experiments, PAc and H_2 concentrations ranged from X_{PAc} ~ 0.0020-0.017 and X_{H2} ~ 0.20-0.99. An schematic of the plug flow reactor system including the Brooks mass flow controllers (MFC), vapor-liquid equilibrium saturator (VLE), switching valve box, and the GC inlet is shown in chapter 2 section 2.4.1. PAc (Alfa Aesar, 97%) was used as received. The gas feed and product lines (going through the valve and reactor) were heated >100ºC, to prevent acid and product condensation. Reaction products were analyzed by an on-line Hewlett-Packard 5890 gas chromatograph equipped with two HP-plot Q capillary columns; one was linked to a flame ionization detector (FID) for analysis of organic products and

unreacted PAc, while the second column was connected to a thermal conductivity detector for analysis of permanent gases such as CO and CO_2. Carbon monoxide hydrogenation experiments were also conducted for two M/SiO_2 (M = Ru, Ni) catalysts to explore their degree of methanation activity. The concentration of carbon monoxide was maintained at 1.0% to simulate what might be encountered during the HDO reaction based on the amount of PAc that was being fed. The conversion and selectivity for a given catalyst was defined according to the following equations:

$$Conversion = \left(\frac{PAc_{in} - PAc_{out}}{PAc_{in}} \right) * 100$$

$$Selectivity = \left(\frac{P_i / \lambda_i}{\sum_i^n P_i / \lambda_i} \right) * 100$$

Where, PAc_{in} and PAc_{out}, denote the concentrations of PAc before and after the reaction, and λ_i, P_i are the stoichiometric factor and product concentration, respectively.

3.3 Results and Discussion

3.3.1 Hydrodeoxygenation of PAc over M/SiO_2: effect of reaction temperature

The effect of reaction temperature on the hydrodeoxygenation activity of PAc was investigated over the range 200-400 ºC. The reactions are classified, based on the formation of main products, as decarbonylation/decarboxylation for hydrocarbon products and hydrogenation and ketonization (for oxygenated products). Prior to examining the HDO of PAc on various SiO_2-supported group VIII noble metals, the activity and selectivity over two different SiO_2 supports were explored. Figures 3.2a and 3.2b show the conversion and selectivity as a function of temperature for Silica Star and Aerosil 300. These supports were capable of catalyzing the ketonization reaction due to the acid properties of the silica

surface [77]. Reaction over Silica Star resulted in the formation of diethyl ketone (DEK) at temperatures above 300 ºC around 92% selectivity. The remaining 8% of products consisted of small amounts of ethane and propionaldehyde. The reaction over SiO_2 Aerosil 300, resulted primarily in the formation of DEK (73% selective), but also ethylene (27% selective) at temperatures above 350 ºC, suggesting the Aerosil 300 has lower surface acidity. Pestman and co-workers have reported reactions of carboxylic acids over metal oxides (i.e., Al_2O_3, Fe_2O_3, SiO_2)[112, 113]. According to their work, a bimolecular ketonization reaction was observed that produced DEK along with CO_2 and water. According to their findings, for metal oxide surfaces with high metal-oxygen bond strength (i.e. SiO_2, TiO_2), the reactant required at least one reactive α-hydrogen atom to form a ketene-like intermediate which subsequently reacted with an adsorbed carboxylate species (from a second molecule of adsorbed carboxylic acid) to form the ketone [114].

The physical and chemical properties (i.e. dispersion and particle size) for M/SiO_2 catalysts are summarized in Table 3.1. Catalyst evaluation data for 1.1wt% Pd/SiO_2 (incipient wetness) and 4.0wt% Pd/SiO_2 (SEA) catalysts are summarized in Figures 3.2c and 3.2d. For 1.1wt% Pd/SiO_2, complete conversion is reached at 350 ºC with 98% selectivity to ethane. Conversely, at lower temperatures of 200 ºC, the product distribution is mainly ethane (83%) and some propionaldehyde (17%), a deoxygenation product formed by C-OH cleavage. Thus, even at 200 ºC, the reaction proceeds mainly through decarbonylation and hydrogenation pathways supported by CO formation. The reaction result is in agreement with previous work conducted by Lamb et al., where the liquid-phase HDO of carboxylic acids over Pd/SiO_2 catalyst occurred mainly via decarbonylation at 300 ºC [115]. The reaction over 4wt% Pd/SiO_2 shows 94% conversion at 350 ºC with 97% and

3% selectivities toward ethane and methane, respectively. At lower temperatures (200 ºC), the product distribution is mainly ethane (94%), with lower production of propionaldehyde (6% selective). The different selectivities with respect to propionaldehyde formation at 200 ºC could be attributed to a combination of particle and support effects. The 2nm particles present for the 4 wt% catalyst have a significantly larger fraction of step and kink sites than the 31 nm particle for the 1.1 wt% catalyst (Table 3.1), which contain primarily low index (111) and (100) crystal faces. Another explanation may be the different degrees of acidity for the two SiO_2 supports, as indicated by the data in Figures 3.2a and 3.2b. Such possible effects are currently under further investigation.

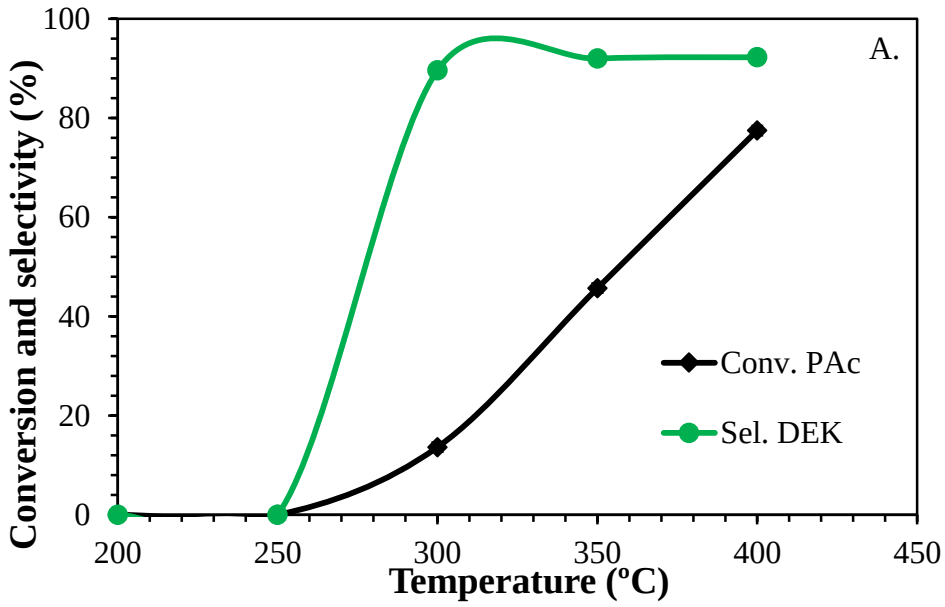

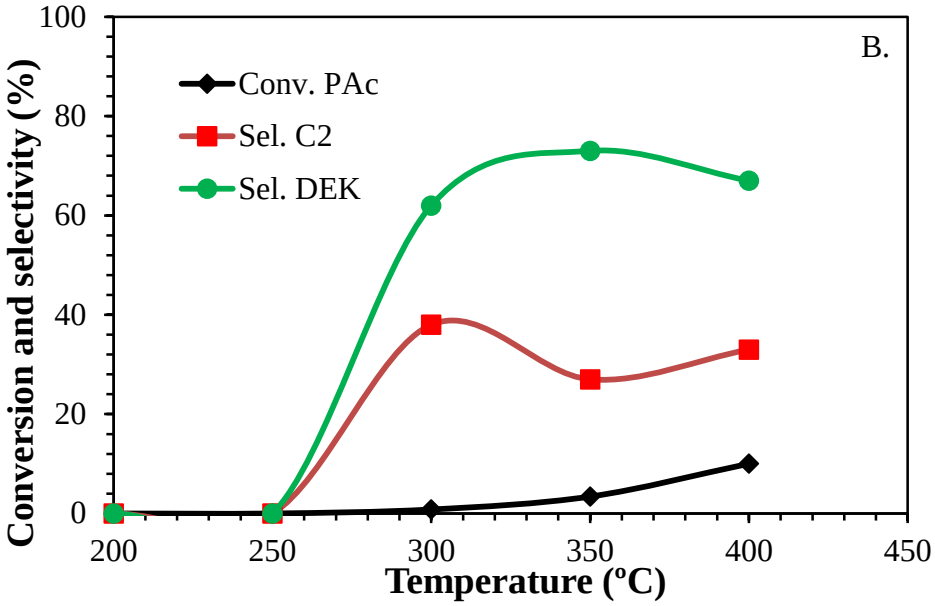
B.
Conv. PAc
Sel. C2
Sel. DEK
Conversion and selectivity (%)
Temperature (°C)
0
20
40
60
80
100
200
250
300
350
400
450

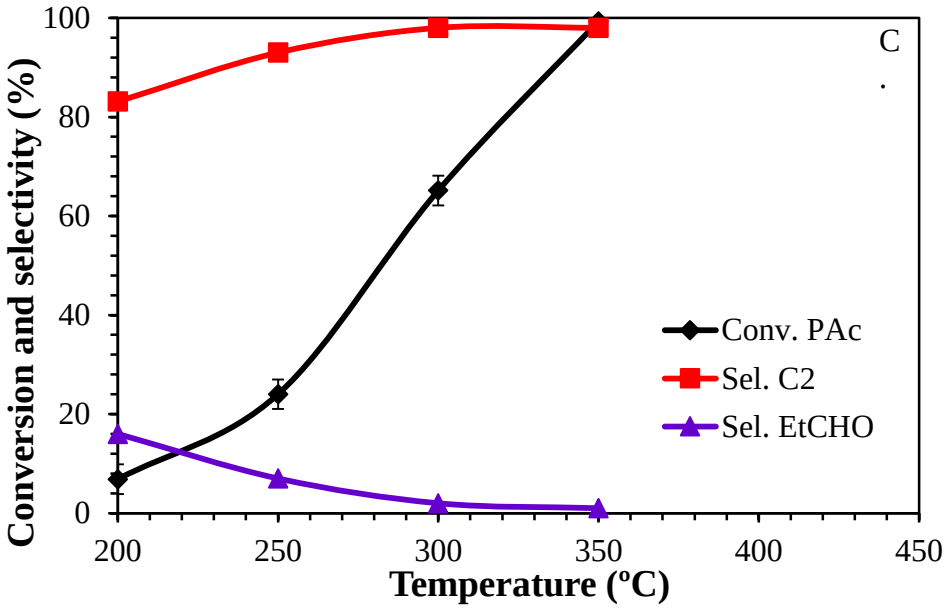
C
.
Conv. PAc
Sel. C2
Sel. EtCHO
Conversion and selectivity (%)
Temperature (°C)
0
20
40
60
80
100
200
250
300
350
400
450

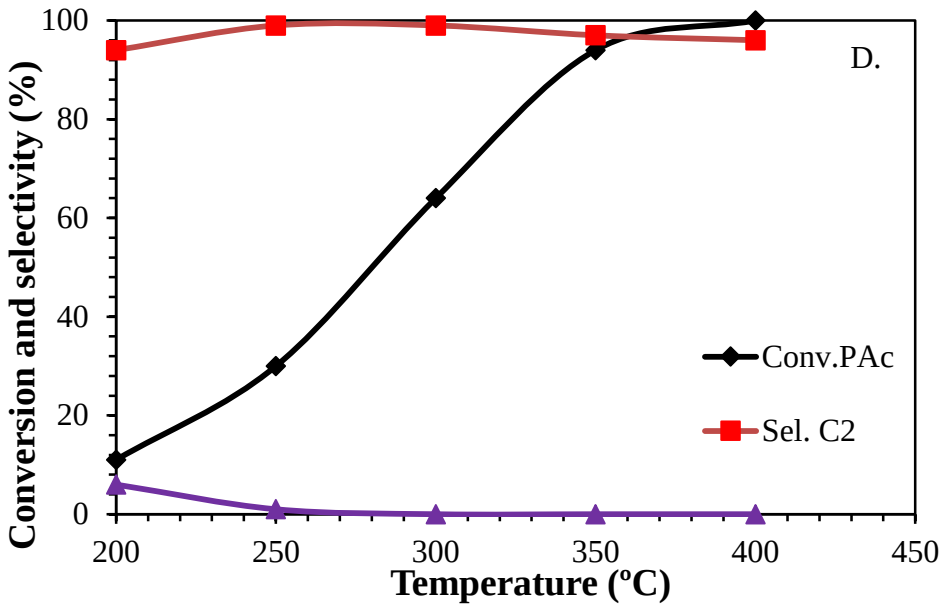

Figure 3.1: Conversion and selectivity for a) Silica Star and b) Aerosil 300 SiO_2 supports; c) 1.1wt% Pd/Silica Star and d) 4.0wt% Pd/Aerosil 300. C2 denotes the sum of ethylene and ethane. EtCHO and DEK refer to propionaldehyde and diethyl ketone, respectively. Mass of catalyst (100-300 mg); feed composition 1% PAc, 20% H_2, balance He. Total flow rates for 1.1wt% and 4wt% Pd/SiO_2 were 50 and 200 sccm, respectively.

Given that DEK was formed on both the Silica Star and (to a much lesser extent) Aerosil 300 supports at temperatures of 300ºC and above, it was important to consider whether this species could undergo reaction to form ethane and/or propionaldehyde at these temperatures on the supported Pd catalyst. Thus, the activity of DEK on 1.1wt% Pd/SiO_2 (incipient wetness) catalyst was explored to address this issue. Hydrodeoxygenation of DEK was conducted between 200-400ºC using 1.0% DEK, 20% H_2, and the balance He. The results confirmed negligible activity (<3% conversion) only by 400ºC, indicating that the observed product formation over the Pd catalyst during HDO of PAc was not proceeding through this pathway on the support surface.

Catalyst performances for 2.1wt% Pt and 2.0wt% Rh on SiO_2 show selectivity only towards hydrocarbons. The results indicate mainly decarbonylation based on the

observation of CO production as opposed to CO_2. Figures 3.3(a) and (b) show the conversion and corresponding selectivities to C_2 and C_3 hydrocarbons for the Pt and Rh catalysts, respectively, as a function of temperature. Measurable PAc conversions were detected at temperatures above 200 ºC and the conversion was complete at temperatures above 300 ºC for Rh and above 350 ºC for Pt. At complete conversion, Pt/SiO_2 shows 100% selectivity to ethane, while Rh/SiO_2 mainly shows selectivity to ethane (89%) and some propane (8%), revealing that some hydrodeoxygenation/hydrogenation is occurring for the formation of propane.

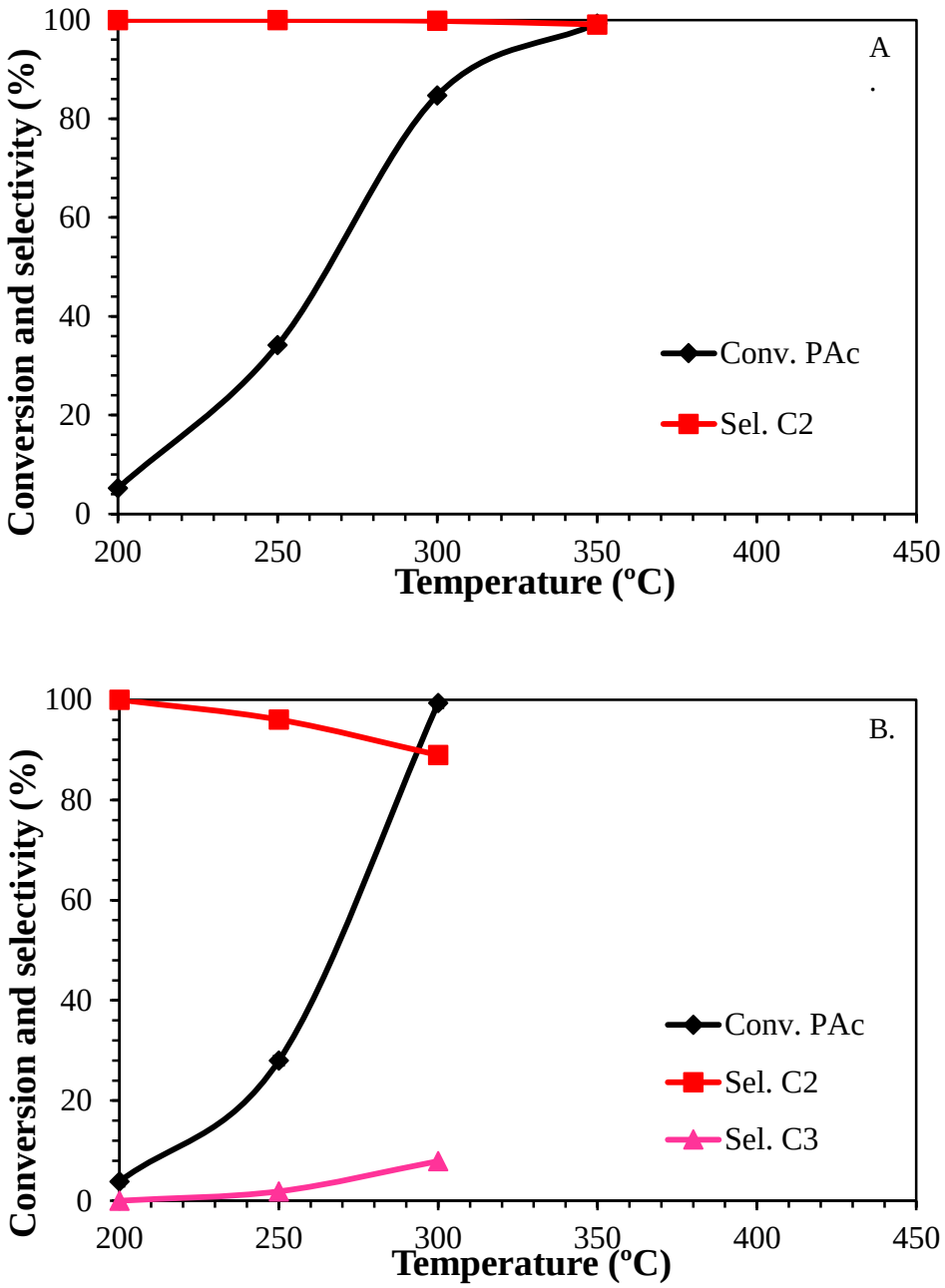

Figure 3.2: Conversion and selectivity for a) Pt and b) Rh supported on SiO2 Star. C2 and C3 denote ethane and propane, respectively. Mass of catalyst (200-300 mg); feed composition 1% PAc, 20% H_2, balance He; total flow rate 50 sccm.

For the reactions with Ru and Ni supported on SiO_2, at high conversion levels, both oxygenated compounds and cracking products are observed. Figure 3.4a shows that the selectivity for Ru/SiO_2 at 200 ºC, is mainly towards methane (72%), ethane (22%) and

small traces of propane and butane (6%). As the temperature approaches to 350 ºC, the selectivity changes toward DEK (45%), suggesting PAc interaction at the surface the support. At this temperature, considerable amounts of methane were formed (38% selectivity). Therefore, methanation experiments were conducted to verify whether the catalyst can produce methane by CO hydrogenation at similar temperatures. Based on these methanation experiments (see appendix B.3 for supporting information), no substantial amount of methane is produced over the temperature range 200-400 ºC. Therefore, methane is considered to be produced via the cracking of PAc and/or ethane.

For Ni/SiO_2 (Fig. 3.4b), very low activity (<1% conversion) is observed at 200 ºC, although at 250 ºC, conversion increases to 11% to form mainly methane (32%) and ethane (59%). However, as the temperature is raised to 350 ºC, the conversion reaches 100% and the product distribution is mainly ethane (71%) and propane (12%), indicative of decarbonylation and hydrodeoxygenation/hydrogenation. At 350 ºC, the catalyst shows methane (9%) and DEK (6%) formation. This methane is formed by CO hydrogenation, as a similar yield of methane is obtained during direct methanation of CO at similar temperature (see appendix B.3 for supporting information).

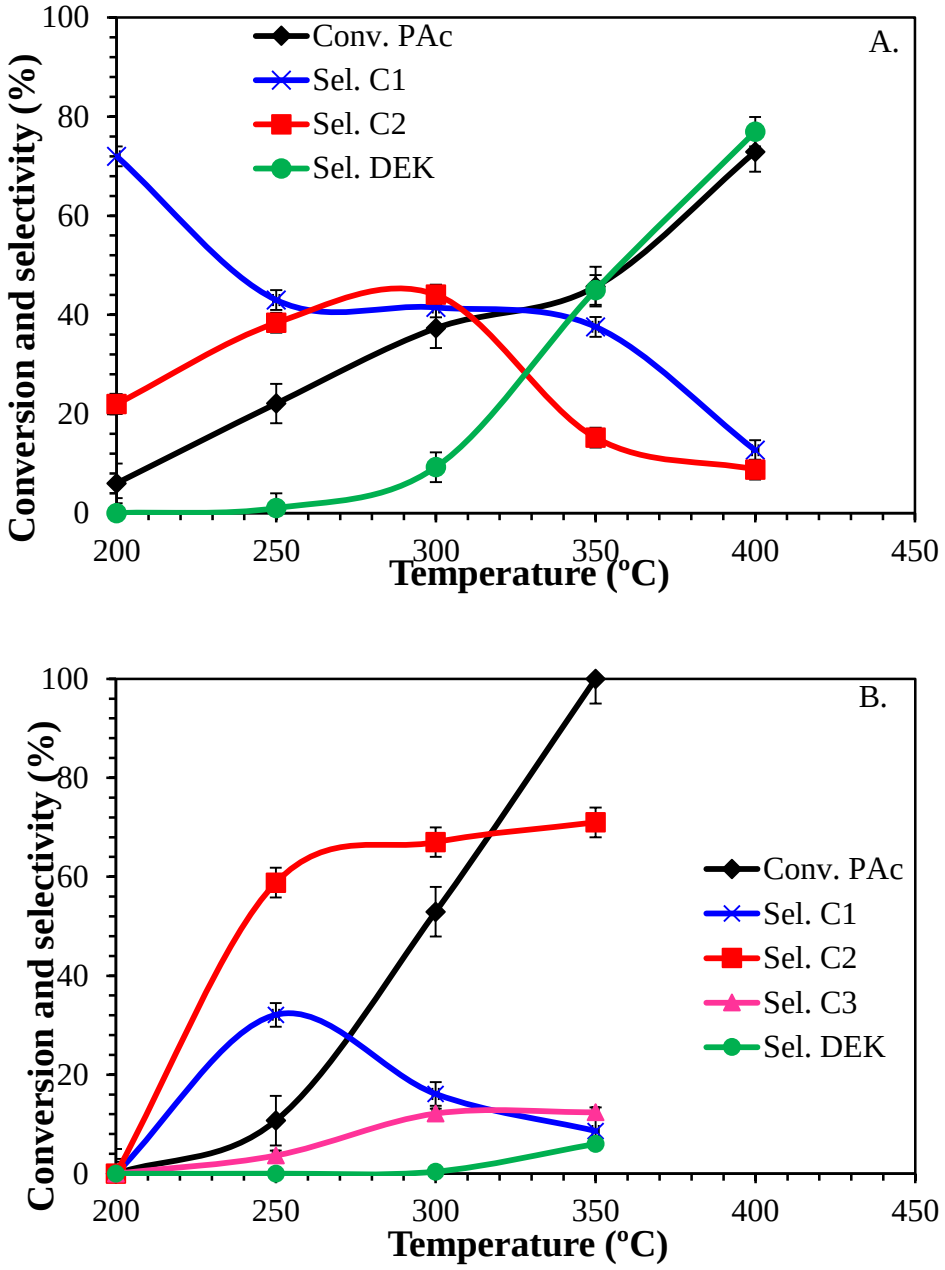

Figure 3.3: Conversion and selectivity for a) Ru and b) Ni over SiO_2 Star. C2 denotes as the sum of ethylene and ethane C3 denote as propane. EtCHO and DEK denote propionaldehyde and diethyl-ketone respectively. Mass of catalyst (200-300 mg); feed composition 1% PAc, 20% H_2, balance He; total flow rate 50 sccm.

In addition to selectivity pattern studies at variable temperatures, experiments were conducted at low conversion at 200 ºC and 1 atm for all the M/SiO_2 catalysts. Table 3.2

summarizes the reaction rates in μmol product formed/min•g_{cat} and turnover frequencies (TOF, molecules•$site^{-1}min^{-1}$). The non-rate performance parameters such as conversion, selectivities towards oxygenated and nonoxygenated hydrocarbon products, and the carbon balance, which is the ratio of carbon atoms in the reactor outlet to carbon atoms in the reactor inlet. The reaction rates were restricted to differential conversion (< 10%), and followed the order: Pd > Rh ~ Pt > Ru > Ni. According to the rates per g catalyst, 4.0wt% Pd/SiO_2 was approximately 25 times higher than for 1.1wt% Pd/SiO_2. However, when activities are expressed as turn over frequencies (activity per surface site of Pd), the orders are reversed, with the lower dispersion 1.1 wt% Pd catalyst being more active by a factor of two. While there may be some support acidity effects, the most likely explanation is that the nature and distribution of the exposed Pd sites are different in these catalysts due to different particle sizes. Overall, the TOF values followed a similar trend as reaction rates with the order: Pd > Ru > Pt > Rh > Ni. The work conducted by Kozhevnikov et al. on the deoxygenation of PAc, suggested comparable activity trends when Pd and Pt are compared (i.e., Pd > Pt) [111]. The Ni/SiO_2 catalyst was the least active at 200 ºC, consistent with previous investigations that gave similarly poor activities for nickel-based catalysts for the HDO of carboxylic acids [116, 117].

Table 3.2: Kinetic data for the screened catalysts in the HDO of PAc at 200 ºC and 1 atm. ~1.0 % PAc, 20% H2/He, catalyst mass 100-300 mg , total flow 50 sccm. Pd* was measured at a total flow 200 sccm.

Metal load (wt%)	**Cat. Mx/SiO_2**	**Rate (µmol/min*g_{cat})**	**TOF (min^{-1})**	**Conv (%)**	**Select. organic product(%)**	**Select. Hydr.(%)**	**C out/ C in**
1.1	Pd	2.57	0.64	7.0	17	83	1.0
4.0	Pd*	69.1	0.32	11.0	6	94	1.0
2.1	Pt	1.60	0.12	5.0	0	100	1.0
2.1	Rh	1.89	0.05	4.0	0	100	0.9
1.6	Ru	4.55	0.24	6.0	0	100	1.0
1.8	Ni	0.13	0.009	1.0	0	100	-

3.3.2 CATALYTIC EVALUATION OF PALLADIUM ON VARIOUS SUPPORTS

In addition to examining the catalytic performance of various group VIII noble metals over SiO_2, the influence of different supports on the activity and selectivity of Pd for the hydrodeoxygenation of PAc was explored. Three different supported Pd catalysts were evaluated for detailed kinetics: 5.0wt% Pd/C, 4.0wt% Pd/SiO_2 and 2.3wt% Pd/TiO_2. Prior to these studies, the performances of the carbon and TiO_2 supports alone were examined, as shown in Figures 3.5a-b. For carbon, no significant activity was observed until 350 ºC, where at 10% conversion, small amounts of ethane (78% selectivity) were formed; the remaining products consist of C_2 and C_3 hydrocarbons and propionaldehyde.

In contrast, for TiO_2 at 300 ºC conversion was 20% and DEK was produced at 100% selectivity. This indicates a strong interaction between the acid and the support that lead to ketonization catalyzed by acidic sites on TiO_2.

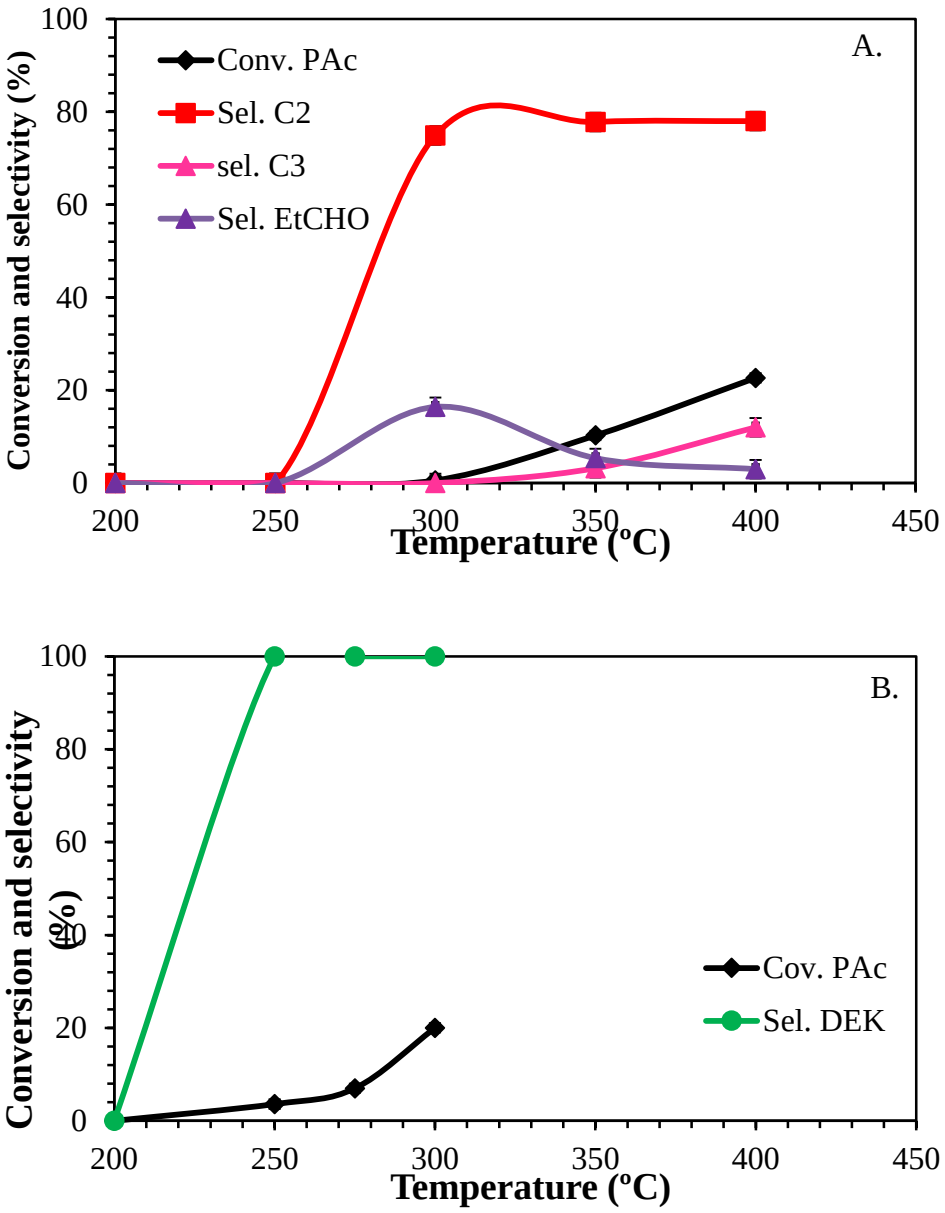

Figure 3.4: Conversion and selectivity for a) carbon and b) TiO_2. C2 denotes as the sum of ethylene and ethane. DEK denote as diethyl-ketone. Mass of catalyst (200-300 mg); feed composition 1% PAc, 20% H_2, balance He; total flow rate 50 sccm.

Figure 3.6a for 5.0 wt% Pd/C shows very high selectivity (100%) at 200ºC and 91% selective at >350 ºC, towards ethane with balance CH_4 over the entire temperature range of 200-400 ºC, producing mainly CO. At the latter temperatures, the formation of CH4 became prominent. Methanation experiments indicate that at 400ºC, 5wt% Pd/C under the same conditions (1% CO/20%H_2/balance He), formed significant amount of CH4 (~30% conv.). Thus, it is highly probable that at the high temperature methanation reaction is present.The results are in agreement with work of Murzin and co-workers on the continuous liquid-phase deoxygenation of lauric acid over 5wt% Pd/C [118]. They reported an activity of 44% conversion and 98% selectivity to undecane at 300 ºC. Both studies indicate that decarbonylation and/or decarboxylation is/are the main reaction pathways. In contrast, for 2.3 wt% Pd/TiO_2 (Figure 3.6b) the reaction temperature has a significant effect on product distribution. At 200 ºC, the selectivity is primarily towards oxygenated compounds (15% propanol, 59% n-propyl-propionate) and some ethane (23%). As the temperature increases, the selectivity towards ethane is increased with no evidence of n-propyl-propionate formation above 300 ºC, which indicates that decarbonylation is favored above this temperature, due to the formation of CO, verified by gaseous products analyses generated by the TCD at the different temperatures studied. At complete conversion (300 ºC), the reaction was selective toward ethane (90%) with balance propanol (10%) due to decarbonylation and hydrodeoxygenation respectively.

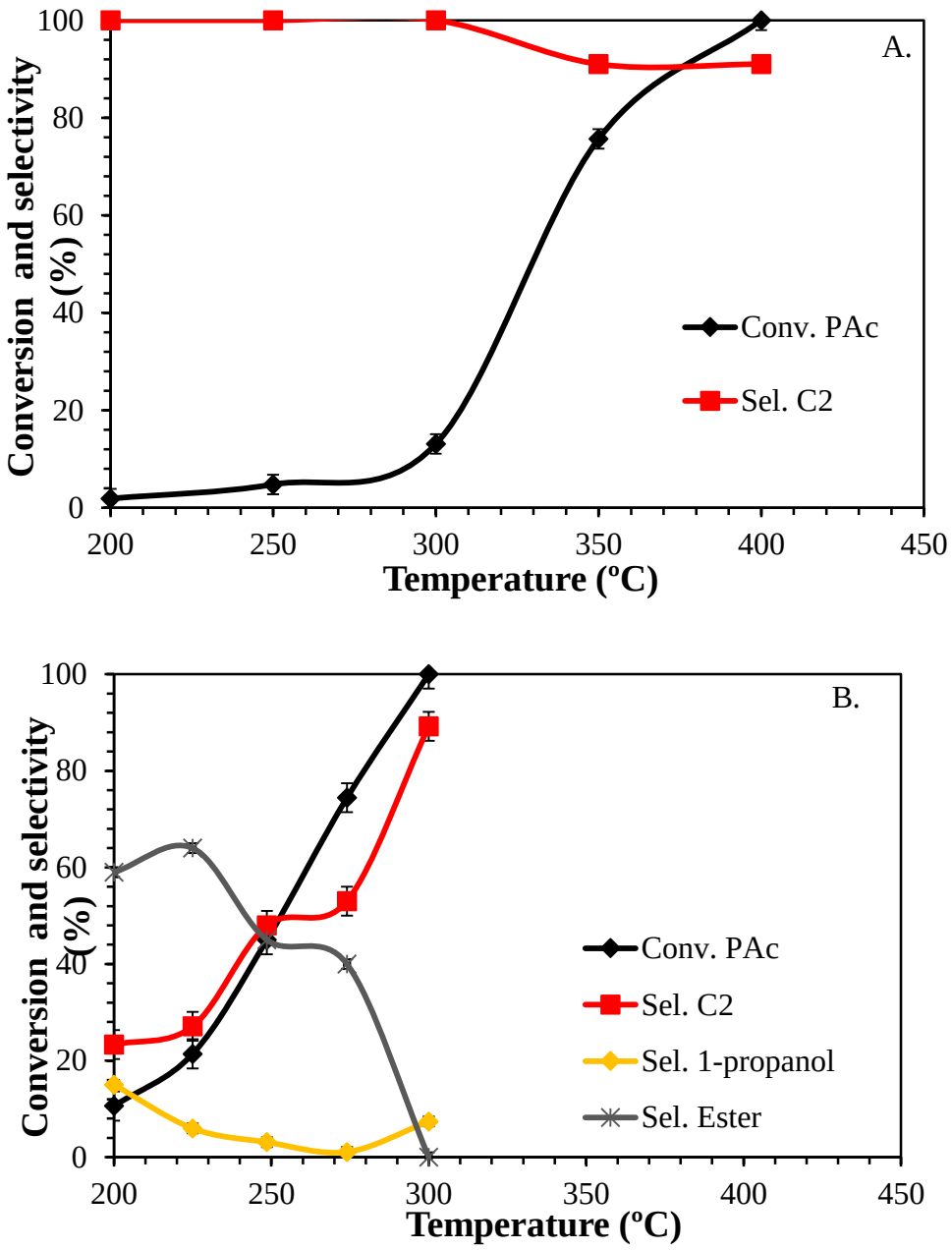

Figure 3.5: Conversion and selectivity for a) Pd/C and b) Pd/TiO_2. C2 denotes as the sum of ethylene and ethane. Ester denotes as propyl-propionate. Mass of catalyst (100-200 mg); feed composition 1% PAc, 20% H_2, balance He; total flow rate 50 sccm.

Table 3.3 summarizes the physical properties (i.e., metal dispersion, particle diameter) and catalyst evaluation results for these three catalysts. The TOF values decrease in the following order: Pd/SiO_2 > Pd/TiO_2 > Pd/C. The Pd/TiO_2 and Pd/SiO_2 catalysts

exhibit TOF values 20 and 30 times higher, respectively, than Pd/C, which can be attributed to a combination the particle size [119] [120] and support effects. It is difficult to assign the higher activities to support effects alone, since TiO_2 and SiO_2 have markedly different physiochemical properties, yet both are much more active than the carbon-supported Pd catalyst. These issues are currently under further investigation in our laboratory.

Table 3.3: Kinetic data for the HDO of PAc over supported Pd catalyst. Reaction conditions: 200 ºC and 1 atm, XPAc = 0.01, 20% H_2/balance He, catalyst weight: Pd/C - 200 mg, Pd/SiO_2 and Pd/TiO_2 – 100 mg.

Metal (wt%)	**Cat.**	**Disp (%)**	**Part. size d_{nm}**	**Conv (%)**	**Sel. Oxy (%)**	**Sel. Non-Oxy (%)**	**C out/ C in**	**TOF (min^{-1})**
5.0	Pd/C	16.9	6.8	2.0	0	100	1.0	0.01
4.0	Pd/SiO_2	55.2	2.0	4.0	6	94	1.0	0.32
2.3	Pd/TiO_2	27.3	4.1	3.3	42	58	1.4	0.20

A series of plausible reaction pathways (Scheme 3.1) has been developed to better understand the performance of these catalysts. For Pd/C at 200-250 ºC, the reaction pathway is more consistent with decarbonylation, based on the simultaneous formation of ethane and CO. At higher temperatures (> 300 ºC), CO_2 is produced, which could be due to decarboxylation, but also the water-gas shift (WGS) reaction. Therefore, the WGS equilibrium constants of K_{eq} ~ 38.1, 19.9 and 11.5 at 300, 350 and 400 ºC [121], respectively, were used to calculate the maximum amount of CO_2 that could be produced by WGS reactions between 350-400 ºC. Results showed that WGS could account for only < 5% of the CO_2 actually observed. Consequently, at 350-400 ºC the reaction proceeds mainly via

decarbonylation and decarboxylation, with negligible WGS. However, at 300ºC, the amount of CO_2 that could be formed based on WGS equilibrium would be equivalent to ~50% of the CO_2 that was actually observed. Therefore, it is possible that some of the CO_2 formed at 300ºC was from WGS, with the remaining amount produced from decarboxylation.

For Pd/SiO_2, similar results are observed. The reaction pathways consist mainly of decarbonylation and hydrogenation steps. PAc is primarily decarbonylated to produce ethane and CO, although the formation of small amounts of propionaldehyde indicates hydrogenation of PAc also occurs, especially at lower temperatures (200-250 ºC). In contrast, Pd/TiO_2 exhibits different reaction pathways. At low temperatures (~200ºC), the formation of propanol and n-propyl propionate is observed. At temperatures >225ºC, ethane, CO and CO_2 are observed, indicating decarbonylation and decarboxylation. The results are consistent with previous studies for the hydrogenation of carboxylic acids over Pt/TiO_2, where it was claimed that oxygen vacancies were generated on the oxide support from the hydrogen spillover of Pd during reduction[122]. Hence, a plausible reaction pathway over Pd/TiO_2 could be the generation of oxygen vacancies at the interface of the catalyst, which in turn weakens the C=O bond of PAc to favor the formation of propanol and water. Esterification of propanol with PAc can then occur to form n-propyl propionate. At higher temperatures, however, decarbonylation of PAc to form ethane and CO becomes the predominant reaction pathway.

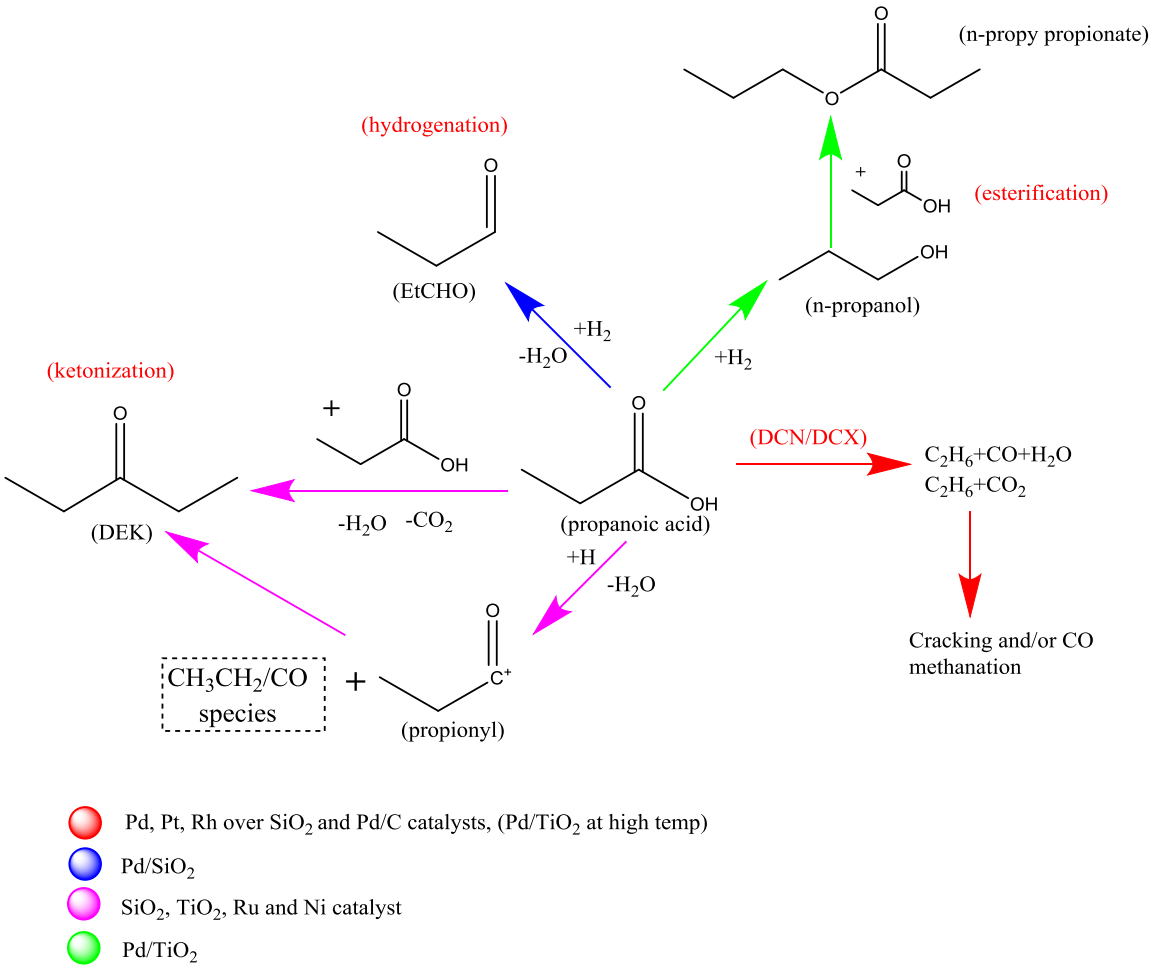

Scheme 3.1: Illustration of plausible reaction pathways for the HDO of PAc over Pd over SiO_2, C and TiO_2.

3.3.3 KINETICS OF PALLADIUM ON VARIOUS SUPPORTS

The reaction rates of the three catalysts can be expressed as power rate law equations, $r = A\exp\left(-\frac{Ea}{RT}\right)\prod_{i=1}^{n} P_i^{xi}$, where A is the pre-exponential factor, Ea is the activation energy, P_i is the partial pressure of species i, and x_i is the reaction order of species i. The apparent reaction order is obtained from the slope of ln reaction rate vs. ln mole fractions of PAc and H_2 (X_{PAc} and X_{H2}, respectively). Figure 3.7 shows the plots for 5.0wt% Pd/C, 4.0wt% Pd/SiO_2 and 2.3wt% Pd/TiO_2. For all catalysts, the reaction orders in PAc

and H_2 are approximately 0.5 and 0, respectively, over the range of concentrations examined. It can be seen based on the formation of CO, that decarbonylation is the dominant deoxygenation pathway under these conditions, which is consistent with the computational studies of Heyden [121] for the DCX and DCN of PAc on Pd(111) model surfaces. Heyden's computations indicated the most kinetically-favorable pathway was decarbonylation and the rate controlling steps included dehydroxylation of PAc (C-OH bond cleavage) to produce propanoyl (CH_3CH_2CO), which was followed by α carbon dehydrogenation to form C_2 hydrocarbons. Thus, the rate determining step is dependent on the capacity to remove the hydrocarbon pool (CH_3CH_x) from the surface, which could explain why the reaction order for PAc was less than first order. For H_2, the reaction order of zero implies a high coverage of hydrogen on the Pd surface, relative to PAc reaction intermediates. Interestingly, even though Pd/SiO_2 and Pd/TiO_2 have different reaction pathways that lead to hydrogenation and esterification products such as aldehydes, alcohols and esters, the reaction orders are not affected by the supports even though the selectivity trends are significantly different.

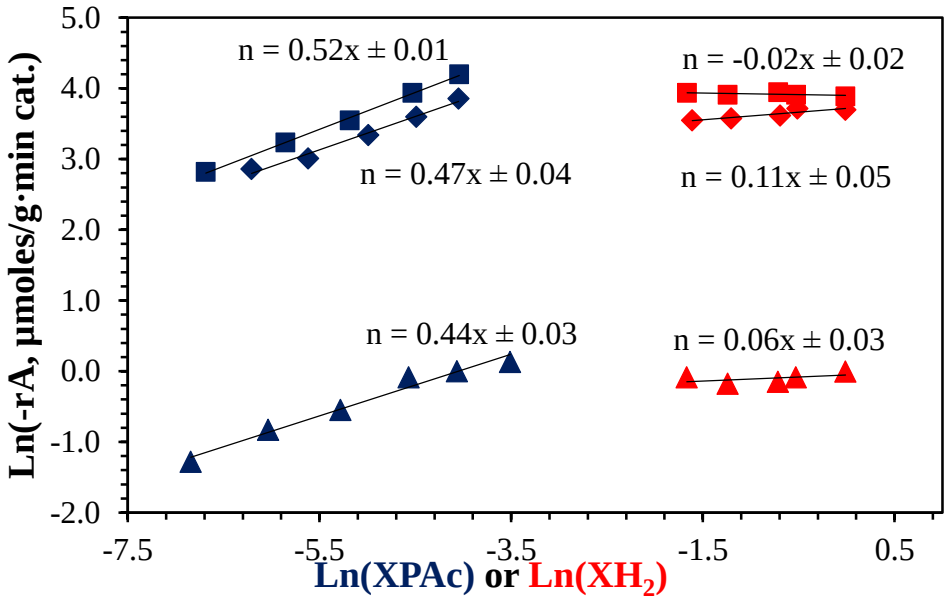

Figure 3.6: Power rate law for the kinetic dependencies of PAc and H_2 for PAc conversion at 200 ºC and 1 atm pressure. (■) 4.0wt% Pd/Aerosil 300, (♦) 2.3wt% Pd/TiO_2, (▲) 5wt% Pd/C, reactor conditions: 20% H_2/balance, total flow: Pd/C - 50 sccm, Pd/SiO_2- 200 sccm, Pd/TiO_2 - 150 sccm. For hydrogen kinetics ~ 1.0% PAc balances He.

The Arrhenius plots for each catalyst are shown in Figure 3.8. Activation energy values of 16.7 ± 0.6, 19.3 ± 1.6 and 11.7 ± 0.7 kcal/mole were obtained for the Pd/C, Pd/TiO_2 and Pd/SiO_2 catalysts, respectively. The apparent activation energies were calculated based on the total consumption rates of PAc, and therefore represent an aggregate of multiple pathways. Pd/C exhibit mainly decarbonylation/decarboxylation reactions, where Pd/SiO_2 and Pd/TiO_2 exhibit hydrogenation/decarbonylation reactions. For Pd/C, the results are in general agreement with previous work [78, 123], where activation energy values for the vapor-phase hydrogenation of carboxylic acids over platinum group metals ranged from 13-16 kcal/mol. In the case of Pd/SiO_2, a recent investigation [111]has reported an Ea value of 8.4 kcal/mol over the temperature range 250-300 ºC, which is lower than the value reported here (11.7 kcal/mol). However, in addition to the temperature range being higher, the selectivity in the previous study was towards ethylene as opposed to

ethane observed here, suggesting different mechanistic behavior. In addition, the value of 8.4 kcal/mol is on the edge of what might be expected in the presence of mass transfer limitations, and no indication that their absence was confirmed by either varying the flow rates (external) or by Weisz-Prater criterion considerations (internal) was given.

While the lower Ea value of 11.7 kcal/mol for Pd/SiO_2 might suggest the presence of some external mass transfer limitations [122], the experiments here were conducted in the kinetic regime. This was confirmed by varying the flow rates over a range of 50-250 sccm for each catalyst to determine the minimum flow rate where the reaction rate remained constant (and thus free of external mass transfer limitations). The minimum flow rates where no external mass transport limitations were observed were found to be 50, 200 and 150 sccm for Pd/C, Pd/SiO_2 and Pd/TiO_2, respectively, and these were the flow rates used in the kinetic studies.

In addition to confirming the absence of external mass transfer limitations, intraparticle diffusion limitations could be dismissed since application of the Weisz-Prater criterion showed that the silica pore diameters were much lower than the mean free path (λ) of PAc, indicating that diffusivity was governed by Knudsen diffusion and that internal mass transport limitations were absent [124-126]. The criterion represents a useful technique, which includes parameters that can be calculated to determine if the reaction process is operating in a diffusion or reaction-limited regime. In order to determine the absence of pore diffusion limitations the following equation has to be satisfied:

$$N_{W-P} = \frac{\Re_{PAc} \rho_c R_p^{\,2}}{C_s D_{eff}} \leq 0.3 \qquad (9)$$

Where $\Re_{PAc}$ (moles/sec*g_{cat}) denotes the rate of reaction of PAc, ρ_c (g_{cat}/ cm^3) is the catalyst pellet density, R_p (cm) is the radius of the particle, Cs (moles/cm^3) is the concentration of PAc at the surface of the catalyst (assuming that it is the same as the bulk concentration) and D_{eff} is the effective diffusion coefficient. If the support pore diameter is much less than the mean free path (λ), the diffusivity is governed by Knudsen diffusion. The criterion values for Pd over carbon, TiO_2 and SiO_2 were 4.5E-04, 2.4E-05 and 1.8E-02 respectively, confirming the absence of internal mass transport limitations. Recently, Lopez-Ruiz and Davis used the same criterion for confirming the absence of internal mass transport during the decarbonylation of heptanoic acid over Pt/C [127]. Therefore, we are confident that the lower E_a value of 11.7 kcal/mol reflects the true kinetics of the reaction. The observations for the lower E_a for Pd/SiO_2 compared to Pd/TiO_2 and Pd/C might be due again to a combination of support and particle size effect, and this is currently under investigation.

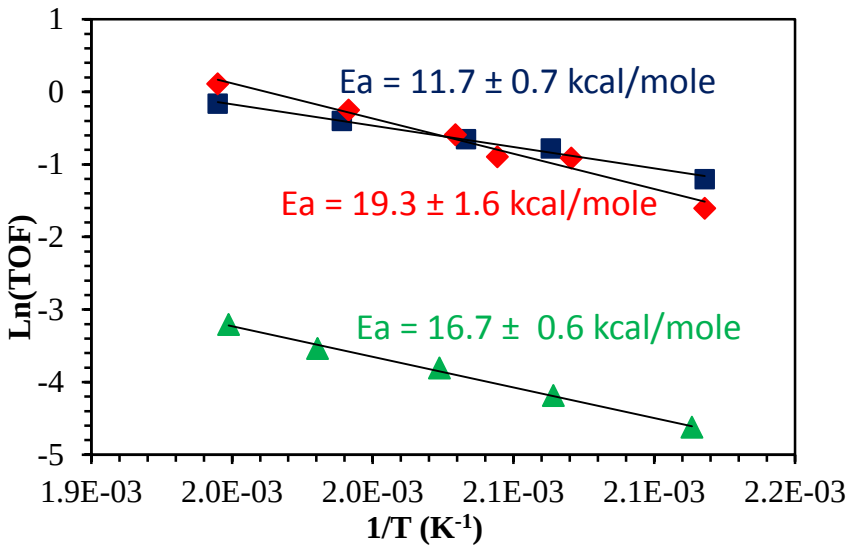

Figure 3.7: Arrhenius apparent activation energies for (■) 4.0wt% Pd/Aerosil 300, (♦) 2.3wt% Pd/TiO_2 and (▲) 5wt% Pd/C.

3.4 CONCLUSION

In conclusion, gas-phase HDO of PAc over various supported metal catalysts has been carried out. For M/SiO_2 catalysts, the choice of group VIII noble metal has a significant effect on the selectivity, which is also significantly influenced by the temperature. At 200 ºC the main reaction pathways for the HDO of PAc under the explored conditions are: (1) hydrogenation, decarbonylation and decarboxylation over Pd, Pt and Rh based catalysts, and, (2) decarbonylation and methanation, followed by ketonization at high temperatures over Ru and Ni respectively. The TOF for the PAc conversion is highest over Pd based catalysts, suggesting that this metal is the most effective for this class of reactions of the ones tested. Kinetic studies over Pd on different supports indicate that the activity (TOF) changes depending on the support, thus indicating a combination of particle size and support effects. For all Pd catalysts, the apparent reaction order with respect of PAc and hydrogen is half and zero order, respectively. These reaction orders are consistent with rate determining steps involving C-OH bond cleavage and the removal of hydrocarbon pool species (e.g., CH_3C_x) from the surface of the catalyst. These initial findings have formed the basis for more focused studies of the effect of Pd particle size on activity and the influence of adding second metal to Pd (i.e., bimetallic effects), and will be the subject of future report.

CHAPTER 4

HYDRODEOXYGENATION OF PROPANOIC ACID, OVER SUPPORTED PALLADIUM CATALYST: EFFECT OF PD PARTICLE SIZE

4.1 INTRODUCTION

The upgrading of biomass-derived pyrolysis oil can provide a means to produce both useful fuels and chemicals, as well as generate substantial economic and environmental benefits [101]. However, such bio-oils contains large amounts of carboxylic acids (e.g., acetic acid, propanoic acid) that decrease stability, are highly corrosive, and are challenging to deoxygenate [128]. Furthermore, fatty acids, fatty acid esters, and triglycerides are present in other sources such as waste greases and nonfood oils from a variety of plants. Therefore, the hydrodeoxygenation (HDO) of biomass-derived carboxylic acids is of both fundamental and practical interest. A significant amount of effort in these areas has focused on catalytic HDO of aliphatic acids using a variety of monometallic and bimetallic catalysts [10, 42, 44-51, 102, 104-109, 128-133].

Previous studies have shown that the physical properties of small catalytic nanoparticles are often significantly different from those of bulk metals [120, 134-138]. Research over the years has suggested that particle size-induced changes in the electronic structure and/or the geometry of the metal atoms exposed at the catalyst surface will influence catalyst performance [139]. Along these lines, Boudart et al. classified catalytic reactions as either

structure-sensitive and structure-insensitive [140]. If the reaction is structure-insensitive and there are no mass transport limitations, the active sites will be proportional to the number of surface metal atoms, regardless of metal nanoparticle size. However, if the reaction is structure-sensitive the turnover frequency (TOF) changes as the metal dispersion is altered. For example, reactions such as the hydrodechlorination of 1,2-dichloroethane over Pd/SiO_2, are considered to be structure-insensitive [141]. In contrast, reactions over Pd/SiO_2 such as hydrogenolysis of methylcyclopropane, hydrogenation of ethylene, and selective hydrogenation of acetylene in ethylene-rich mixtures are considered structure-sensitive [142-145].

Interestingly, there has been very little work performed to explore the structure sensitivity of aliphatic acid HDO over metals. In the only such study, Simakova et al. investigated the effect of metal dispersion on the deoxygenation of palmitic and stearic acid over Pd/C catalysts in the liquid phase[14]. The initial TOF varied by almost an order of magnitude when the initial dispersion of a 1%Pd catalyst was varied from 18% to 72%. However, only four particle sizes were examined, and the catalysts (especially the one with highest dispersion) were found to greatly sinter during the reaction.

The present work explores the effects of metal nanoparticle size (1.9-12.4 nm) on the HDO of propanoic acid (PAc) over a family of silica-supported palladium catalysts. While some small effects on catalytic performance are observed, the activity and selectivity of HDO is not influenced significantly by Pd particle size in the range studied, suggesting that the reaction is largely structure insensitive.

4.2 EXPERIMENTAL METHODS

4.2.1 CATALYST SYNTHESIS

The Pd/SiO_2 catalysts were synthesized by strong electrostatic adsorption (SEA), where the pH of the metal salt complex solution (100-400 ppm of $[Pd(NH_3)_4]^{2+}Cl_2$, 99.9% Sigma Aldrich) was controlled based on the potential of zero charge (PZC) of the SiO_2 [85, 86]. Once the pH of 11.5 was acquired, the support (Aerosil 300, S_{BET} = 330 m^2/g, Evonik) was impregnated and shaken for 1 hour at room temperature. The surface loading of the catalyst support ranged from 1000-2000 m^2/L. Additional details about the SEA procedure are explained elsewhere [88-90, 146]. Additionally, for some catalysts the support was heat treated under different conditions prior the impregnation of Pd (see table 4.1). The catalysts were dried overnight, and pre-treated at different conditions in 20% H_2/balance He in order to obtain a range of different particle sizes through sintering. The final treatment stage prior to reaction involved *in-situ* reduction in 20% H_2/balance He for 2 hours at 350ºC. Table 4.2 summarizes the prepared Pd/SiO_2, which were named Pd-1 to Pd-10 based on their increasing particle size.

Table 4.1: Physical properties of support SiO_2 Aerosil heat treatment.

Catalyst Id.	**Pd loading (wt%)**	**Support SA (m^2/g)**	**Support heat treat. Cond.**
Pd-1	2.0	330	
Pd-2	4.0	330	Not heat treated
Pd-3	2.6	330	
Pd-4	2.0	309	350ºC, 2hrs, helium

Pd-5	1.4	190	800ºC, 24hrs, calcined
Pd-6	1.9	130	Not heat treated
Pd-7	3.5	285	500ºC, 2hrs, hydrogen
Pd-8	3.5	285	
Pd-9	2.9	190	800ºC, 24hrs, calcined
Pd-10	3.3	309	350ºC, 2hrs, helium

Table 4.2: Physical properties of Pd/SiO_2 a Determined by chemisorption, O_2-H_2 titration.
[b] Catalysts were reduced in-situ at 350ºC, for 2 hours at 5ºC/min, unless otherwise noted.
[b] TEM results in parenthesis indicate the particle size obtained after the reaction.

Catalyst Id.	**Pd loading (wt%)**	**Pre-treatment cond.[b] 20% H_2/bal. He**	**Disp.[a] (%)**	**d_{Pd}[a] (nm) O_2-H_2 titr.**	**d_{Pd} (nm) TEM (after)[b]**
Pd-1	2.0	150ºC, 2.5ºC/min, 2hrs	58.6	1.9	
Pd-2	4.0		55.7	2.0	2.7(2.8)
Pd-3	2.6		53.7	2.1	
Pd-4	2.0		43.1	2.6	
Pd-5	1.4		36.4	3.1	
Pd-6	1.9		29.4	3.8	5.1(8.0)
Pd-7	3.5	400ºC, 10ºC/min, 2hrs	18.1	6.2	
Pd-8	3.5		14.3	7.9	
Pd-9	2.9	150ºC, 2.5ºC/min, 2hrs	11.6	9.7	

Pd-10	3.3	350ºC, 2.5ºC/min, 2hrs	9.0	12.4	12.1(13.4)

4.2.2 PULSED H_2 TITRATION OF OXYGEN PRE-COVERED SITES

The dispersions and particle sizes of the catalysts were determined by pulsed hydrogen titration of oxygen pre-covered sites utilizing a Micromeritics 2920 AutoChem II Analyzer. The catalysts (0.1-0.2g) were reduced at 350 ºC by flowing 20% H_2/balance He, for 2 hrs, followed by purging with Ar for 1 hr to remove the physisorbed hydrogen. After cooling to 40 ºC in flowing Ar, the catalysts were exposed to 10% O_2/He for 30 min followed by purging with Ar (30 min). Titration with pulses of 10% H_2/Ar was then employed until no further H_2 uptake occurred.

4.2.3 HDO OF PAC: CATALYST EVALUATION

All activity and kinetics measurements for the HDO of PAc were carried out under atmospheric pressure in a single pass, packed bed, plug flow reactor system with online GC analysis. Prior to the reaction, the catalysts (~0.2 g) were reduced *in-situ* (as indicated in Table 4.1) at a total flow of 200 sccm for 2 hours in 20% H_2 balance He. All the catalytic activity experiments were conducted at 200ºC, with 1.0% PAc (Alfa Aesar, 99%) and 20% H_2, balance He. The reaction rate was determined based on the formation of product (which is proportional to the rate of acid disappearance) in μmol product formed/min•gcat and turnover frequencies were based on the reaction rate per active site based on surface atoms (TOF, molecules•site^{-1}min^{-1}). For the kinetic experiments, PAc and H_2 mole fractions ranged from X_{PAc} ~ 0.0020-0.017 and X_{H2} ~ 0.20-0.99. Measurements were also carried out from 200-240 ºC in order to determine the apparent activation energy. The plug flow

reactor system, including gas chromatographic analysis of product streams, is the same as described previously [146]. The conversion and selectivity for a given catalyst were defined according to the following equations:

$$Conversion = \left(\frac{\sum P_i / \lambda_i}{PAc_{in}} \right) * 100$$

$$Selectivity\ of\ Product\ i = \frac{TOF_{Pi}}{\sum_{i}^{n} TOF_{Pi}}$$

where PAc_{in} denotes the concentration of PAc in the feed, TOF_{Pi} is the turnover frequency for a given product, and λ_i and P_i are the stoichiometric factors and product concentrations, respectively. Experiments were carried out at differential conversion in the kinetic regime, under conditions confirmed to be free of both internal (Fig. C.1) and external (Fig. C.2) mass transfer limitations (see appendix C).

4.3 Results and Discussion

4.3.1 Particle Size Characterization

In order to be able to draw clear correlations between structure and catalytic performance, the intrinsic catalyst properties such as dispersion, surface active sites, and particle size had to be determined. As summarized in Table 4.1, two characterization techniques were employed: chemisorption (O_2-H_2 titration), and STEM, with the latter applied to both the fresh and spent catalyst (i.e., before and after the reaction). A wide range of particle sizes and dispersions ranging from 1.9-12.4 nm was obtained by O_2-H_2 titration. Representative STEM images and histograms are shown in Figure 4.1 for the Pd-2, Pd-6 and Pd-10 catalysts, both before and after reaction. The Sauter mean particle size was determined from the surface area based on the measured Pd crystallite size distribution. The estimated

particle size for the fresh and spent Pd-2 catalyst was 2.7±0.9 and 2.8±0.7 nm, respectively, which is in excellent agreement with chemisorption. For Pd-6, particle sizes of 5.1±1.1 and 8.0±2.0 nm were found for the fresh and spent catalyst, respectively. Finally, the size of the fresh Pd-10 (12.1±2.7 nm) was not significantly effected after the reaction (13.4±3.5 nm) and was in close agreement with chemisorption (d_{Pd} =12.4 nm). Additionally, the DeBrouckere mean particle size calculated from STEM was compared with that estimated by XRD, showing good agreement (see appendix C.2, figure C.3). Given the inherent assumptions and limitations (e.g., ideal particle shape [147], relatively small sampling of particles in microscopy) in the calculations associated with these techniques, the agreement is relatively good overall. Since chemisorption can count all exposed surface Pd sites in each sample, the estimate of particle size and dispersion from this approach was used to obtain the TOF values for this study.

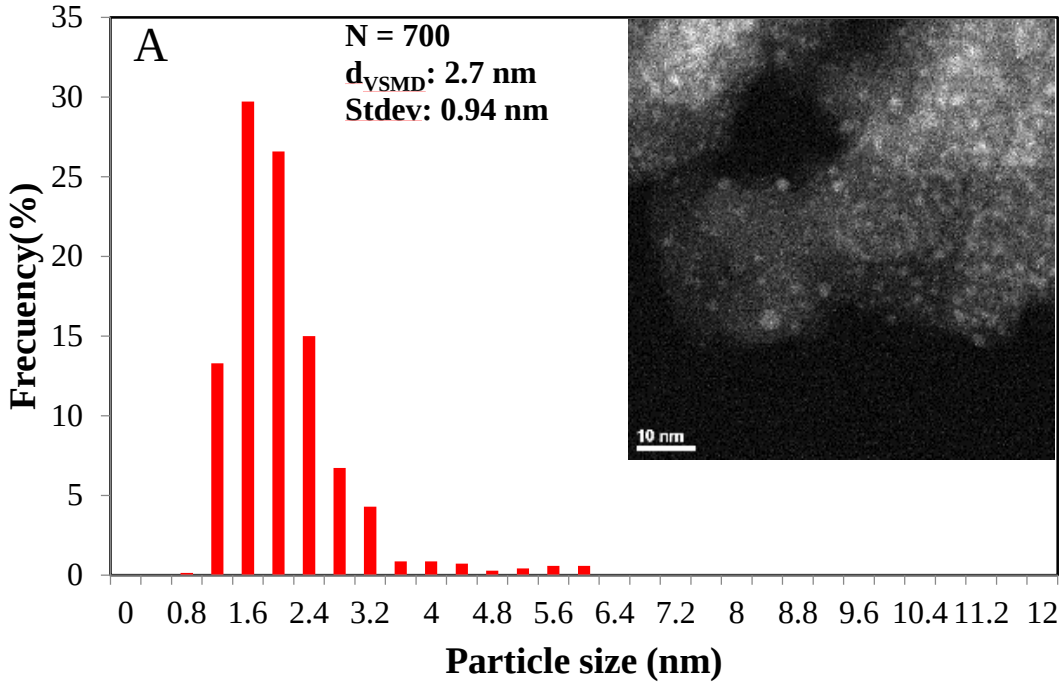
A
N = 700
d_{VSMD}: 2.7 nm
Stdev: 0.94 nm
10 nm
Frecuency(%)
Particle size (nm)
0
5
10
15
20
25
30
35
0 0.8 1.6 2.4 3.2 4 4.8 5.6 6.4 7.2 8 8.8 9.6 10.4 11.2 12

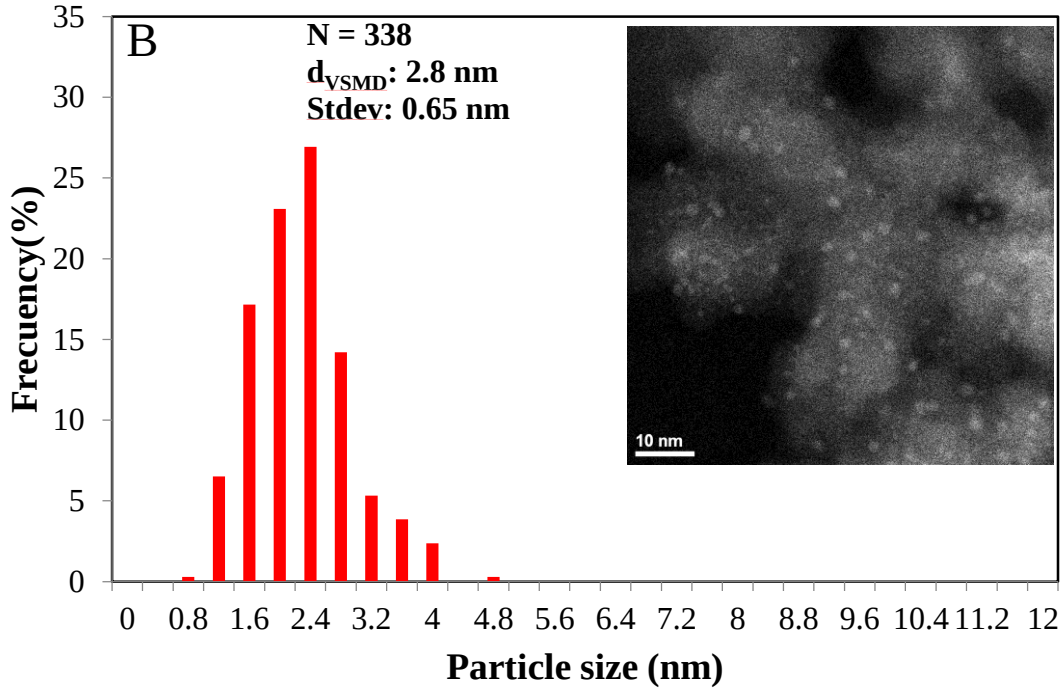
B
N = 338
d_{VSMD}: 2.8 nm
Stdev: 0.65 nm
10 nm
Frecuency(%)
Particle size (nm)
0
5
10
15
20
25
30
35
0 0.8 1.6 2.4 3.2 4 4.8 5.6 6.4 7.2 8 8.8 9.6 10.4 11.2 12

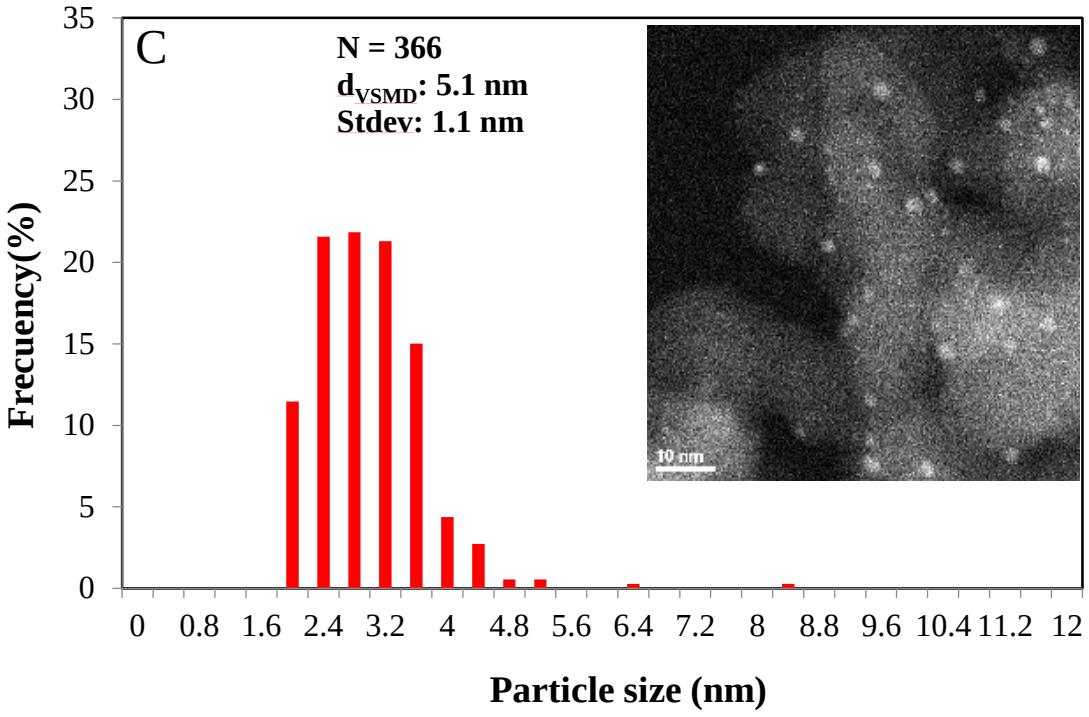
C
N = 366
d_{VSMD}: 5.1 nm
Stdev: 1.1 nm
10 nm
Frecuency(%)
Particle size (nm)
0
5
10
15
20
25
30
35
0 0.8 1.6 2.4 3.2 4 4.8 5.6 6.4 7.2 8 8.8 9.6 10.4 11.2 12

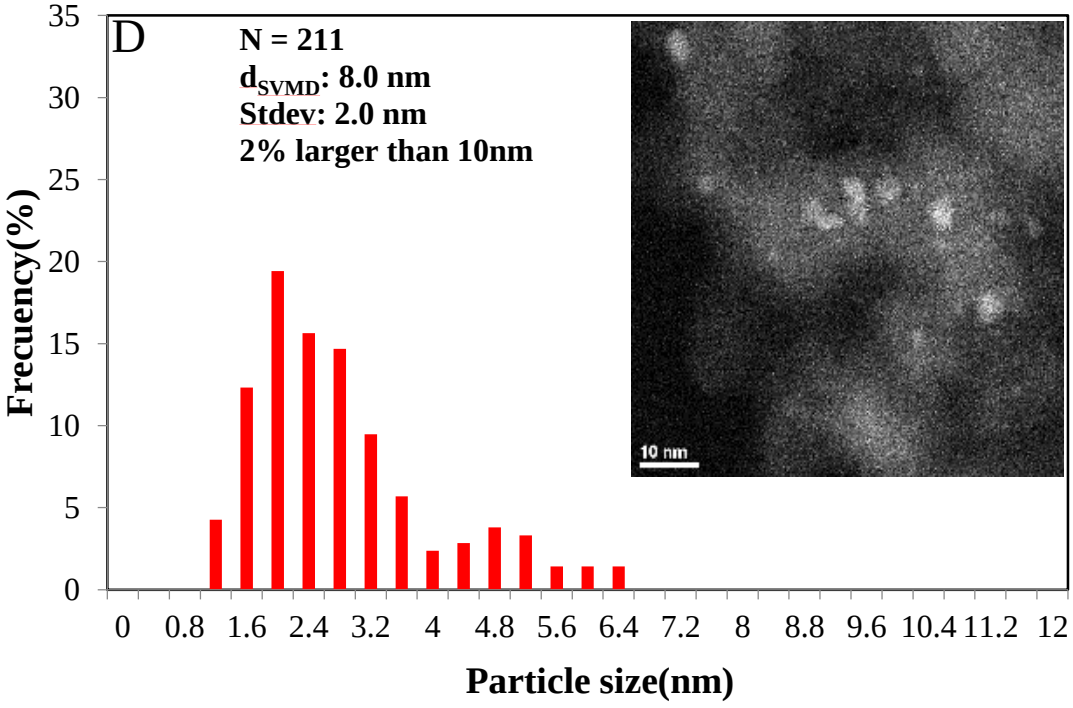
D
N = 211
d_{SVMD}: 8.0 nm
Stdev: 2.0 nm
2% larger than 10nm
10 nm
Frecuency(%)
Particle size(nm)
0
5
10
15
20
25
30
35
0 0.8 1.6 2.4 3.2 4 4.8 5.6 6.4 7.2 8 8.8 9.6 10.4 11.2 12

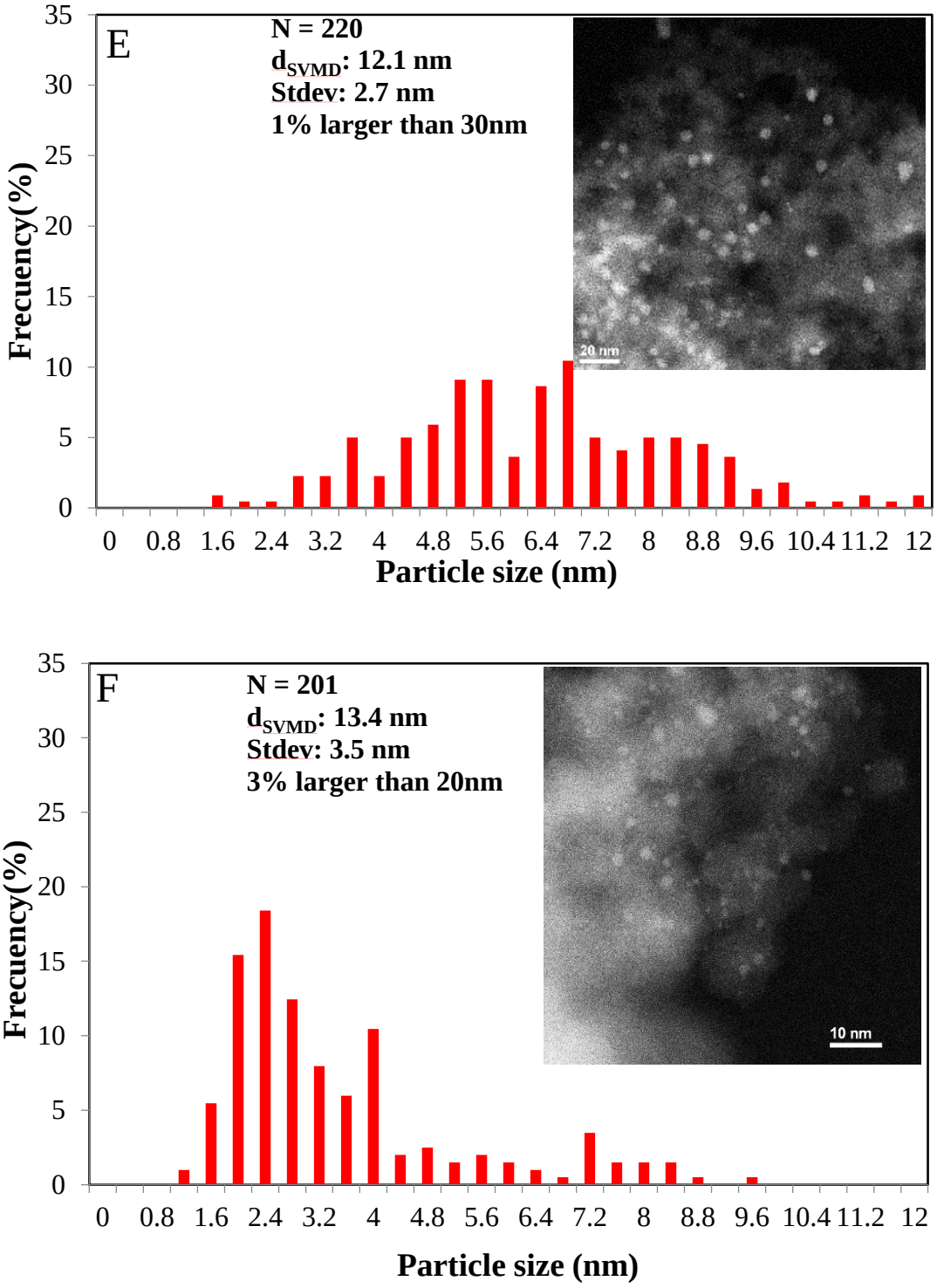

Figure 4.1: Histogram showing the particle size distribution of Pd-2 (2nm A-B before and after reaction), Pd-6 (C-3.8nm before and D-3.8nm after reaction, 1% of particles around

20nm) and Pd-10 (E-12.4 nm before and F-12.4nm after reaction, 2-4% particle around 30nm).

4.3.2 Particle Size Effect on Activity and Selectivity

In order to elucidate the effect of metal particle size for the HDO of PAc, the activity and selectivity of each Pd/SiO_2 catalyst was investigated under the same conditions. The specific activity expressed per Pd surface atom (TOF) and selectivity towards C_2H_6 and propionaldehyde (EtCHO) are summarized in Table 4.2. Starting at the smallest particle size, the overall TOF increased by around a factor of 2.5 up to 3.1 nm, above which point it remained roughly constant. The overall change over the whole range is considerably less than the differences in other well-known structure sensitive reactions [142, 148, 149]. This point will be addressed in the next section. From 1.9 to 3.1 nm, the selectivity is found to be >90% toward C_2H_6, with the balance going towards EtCHO. Thus, in this size range, the HDO of PAc occurs primarily via decarbonylation and subsequent hydrogenation (pathway 2 in Scheme 4.1) to form the main products C_2H_6 and CO. Further increase in the particle size up to 12.4 nm shifted the selectivity toward EtCHO up to about 24% (balance C_2H_6).

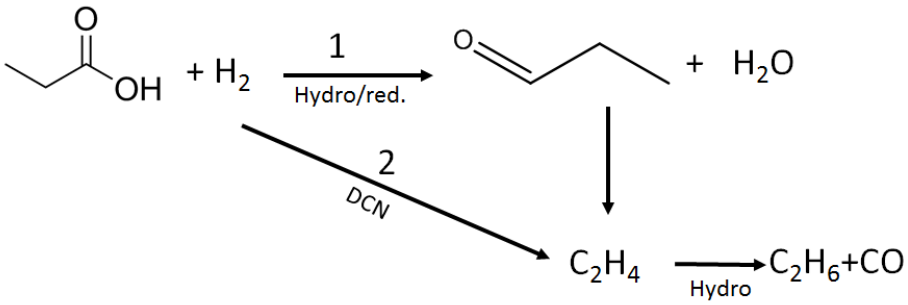

Scheme 4.1: Reaction pathway for the decarbonylation/hydrogenation of PAc over Pd/SiO_2.

These trends can be further analyzed by examining the change in the TOF for production of each product with particle size, as shown in Table 4.2. The general trend is that the C_2H_6 TOF increases more at the lowest particle size range, while the EtCHO increases more at the higher particle size range. To attempt to quantify the trends in product formation and further explore structure sensitivity, the following analysis was performed. Given the f.c.c. crystal structure of Pd and assuming the particles are shaped as cubo-octahedra with corners truncated as (100) planes, Van Hardeveld and Hartog [119] statistics can be applied. As a result, the amount of (111) and (100) planes can be estimated based on the Pd particle sizes. Table 4.2 summarizes the fraction (in percent) of (111) and (100) planes found in these samples. In the range from 1.9 to 3.1 nm where the largest change in overall TOF occurs, the combined fraction of (111) and (100) planes changes from 56% to 71%, with low coordination sites such as corners and edges making up the significant fraction of the remaining surface. As the particle size increases beyond 3.1 up to 12.4 nm, the combined fraction of (111) and (100) planes increases from 71 to 93%, at which point the low coordinated sites are greatly diminished.

For the purposes of this analysis, it was hypothesized that the TOF value for each product will be different on each of these types of surface sites (i.e., (111), (100), corners/edges). If this is the case, then the TOF values for each product can be written as:

$$TOF_{C2H6} = TOF_{C2H6/(111)} \times F_{(111)} + TOF_{C2H6/(100)} \times F_{(100)} + TOF_{C2H6/CE} \times F_{CE}$$

$$TOF_{EtCHO} = TOF_{EtCHO/(111)} \times F_{(111)} + TOF_{EtCHO/(100)} \times F_{(100)} + TOF_{EtCHO/CE} \times F_{CE}$$

where, TOF_{C2H6} and TOF_{EtCHO} are the total TOF values for those products, $TOF_{i/j}$ are the TOF values for the given molecule i = C_2H_6, EtCHO, on a given type of site j = Pd(111), Pd(100), Pd corners/edges (CE), and F_j are the fractions of each type of site. Using the

experimental data for the ten catalysts in Table 4.2 and assuming that TOF values on various types of sites are independent of particle size, the values of $TOF_{i/j}$ were estimated by using least squares regression.

Figure 4.2 shows the estimated total TOF values for each product (lines) compared with the experimental data (points), along with the fitted values of $TOF_{i/j}$. It is seen that the decarbonylation of PAc to produce C_2H_6 is favorable on both Pd(111) and Pd(100) faces but not on corners/edges. In addition, the production of EtCHO would appear to be favored on Pd(100) sites. While admittedly somewhat speculative, this analysis helps to rationalize the very small particle size effect over the range studied. The reaction takes place mainly on Pd(111) and Pd(100) sites, which increase by 75% over the range studied. In contrast, the almost 7-fold decrease in the fraction of corners/edges sites has a negligible effect on activity due to their inactivity for this reaction.

As mentioned earlier, a previous particle size effect study involving deoxygenation of palmitic and stearic acid over 1 wt% Pd/C was conducted by Simakova et al. Their results suggested that as the Pd dispersion increased up to 65%, there was an increase in the TOF. However, for 72% disperse catalyst, there was a significant (~10-fold) decrease in the TOF, attributed to the extreme sintering that occurred in that sample based on post reaction characterization. The present results would seem to contradict these previous findings, since overall activity decreased with increasing dispersion and there was no significant sintering at the lowest dispersion. Further studies are required to determine if the origin of these differences is from the support (SiO_2 vs. C) or reaction environment (gas-phase vs. liquid-phase).

Table 4.2: Kinetic data for the screened catalysts in the HDO of PAc at 200 ºC and 1 atm. ~1.0 % PAc, 20% H2/He, catalyst mass 200 mg , total flow 200 sccm. Van Hardeveld and

Hartog statistics on Pd(111) and Pd(100) fraction for the Pd, f.c.c Cubo-Octahedron-corners truncated at (100).

Cat. Id.	**d_{pd} (nm) O_2-H_2 titr.**	**TOF (min^{-1})**	**EtCHO Sel.**	**C_2H_6 Sel.**	**EtCHO TOF (min^{-1})**	**C_2H_6 TOF (min^{-1})**	**Face (111) (%)**	**Face (100) (%)**
Pd-1	1.9	0.38	0.08	0.92	0.05	0.33	47	6
Pd-2	2.0	0.51	0.05	0.95	0.05	0.46	49	6
Pd-3	2.1	0.56	0.09	0.91	0.05	0.51	50	7
Pd-4	2.6	0.67	0.06	0.94	0.10	0.57	56	9
Pd-5	3.1	0.89	0.04	0.96	0.04	0.85	60	11
Pd-6	3.8	0.92	0.16	0.85	0.11	0.81	64	12
Pd-7	6.2	0.95	0.09	0.91	0.08	0.87	70	15
Pd-8	7.9	0.84	0.17	0.83	0.13	0.71	72	16
Pd-9	9.7	0.87	0.16	0.84	0.13	0.74	74	17
Pd-10	12.4	0.95	0.24	0.76	0.22	0.73	75	18

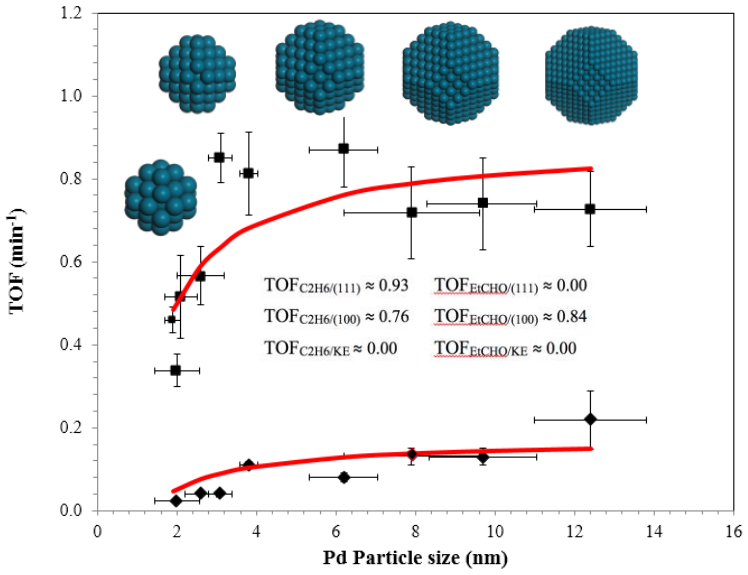

Figure 4.2: TOF_{C2H6} (squares) and TOF_{EtCHO} (diamonds) as a function of particle size for the series of Pd/SiO_2 catalysts for the HDO of PAc at 200 ºC and 1 atm.Reactor conditions: ~1.0 % PAc, 20% H_2/He, catalyst mass 200 mg , total flow 200 sccm. The solid lines are the least squares fits of the data. See text for details.

4.3.3 Particle Size Effect on Kinetics

The reaction kinetics for the Pd-10 (12.4nm) catalyst were explored using a power rate law equation, $TOF_i = A_i \exp\left(-\frac{Ea_i}{RT}\right)\left(\prod_{i=1}^{n} X_i^{\alpha_i}\right)P^{\sum_{i=1}^{n}\alpha_i}$,where A_i is the pre-exponential factor, Ea_i is the apparent activation energy, X_i are the mole fractions of species i, P is the total pressure in the reactor, α_i is the reaction order of species i, and TOF_i is the rate of production of species i in terms of turnover frequency. The reaction orders can be obtained from the slope of ln TOF vs. ln X_i of PAc and H_2 (i.e., X_{PAc} and X_{H2}, respectively). Figure 4.3 shows that the reaction orders for the TOF_{C2H6} on Pd-10 with respect to PAc and H_2 are approximately 0.5 and 0, respectively, over the concentration range examined. These reaction orders are consistent with our previous study [146] of the Pd-2 (2 nm) catalyst, which produces essentially only C_2H_6 as a product (cf. Table 4.2). In addition, the results are in harmony with the computational studies of Heyden [150] for the decarbonylation (DCN) of

PAc on Pd(111) model surfaces. Their findings indicated that a α-carbon dehydrogenation followed by dehydroxylation to produce CH_3CHCO is required to promote C-CO bond scission to yield CO and C2 hydrocarbons. The extent and removal of the hydrocarbon pool (CH_3CH_x) at the surface, explains why the reaction order with respect to PAc is less than one. Based on these results, it is concluded that the rate-determining step for the DCN reaction is essentially the same for all the particle sizes studied.

In contrast, the TOF_{EtCHO} exhibits reaction rate orders for PAc and H_2 of approximately 1.0 and 0.3, respectively, over the range of concentrations examined. The reason for the different reaction rate orders (with respect to PAc and H_2) for the two products formed can be explained by the two reaction pathways PAc undergoes. For the formation of C2's hydrocarbons, the preferred reaction pathway is DCN (CO and C2's), where for the formation of EtCHO the preferred reaction pathway is hydrogenation (without carbon loss), as described below. A Langmuir Hinshelwood-type adsorption sequence is assumed with PAc and H_2 adsorbing dissociatively mainly on Pd(100) sites of the metal surface. The adsorbed propionate and H species combine to form propionyl and/or acetal intermediates. The subsequent hydrogenation of propionyl and/or acetal species leads to the formation of EtCHO. Therefore, the hydrogenation to produce EtCHO would be expected to have a 1^{st} order dependence with respect to PAc.

With respect to the concentration of H_2, a reaction order of 0.3 depends on what reaction pathway is favorable. If the addition of hydrogen is more favorable, a reaction rate order of ~0.5 is obtained, due to the assumption of equilibrated hydrogen adsorption on the surface. The further removal of H_2O through condensation would be expected to exhibit a reaction order of ~0. Alternatively, if –OH bond scission occurs, a rate order of ~0 will be

expected. The further addition of H to form propionyl species (CH_3CH_2CO) at the surface would have a rate order of ~0.5. Overall, if both reactions occur to some extent, the rate order with respect to hydrogen should be between 0-0.5. This would be consistent with the experimental observed rate order with respect to hydrogen of 0.3. The formation of propionyl species, which could also undergo decarbonlyation to produce C2 species that are responsible for the formation of ethane.

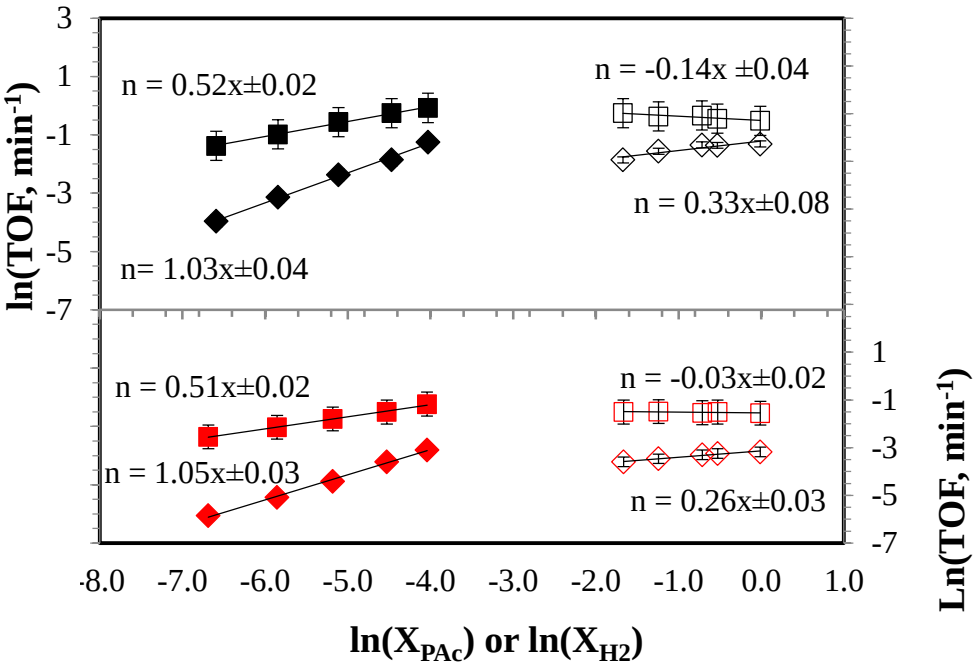

Figure 4.3: Power rate law dependencies of TOF_{C2H6} (squares) and TOF_{EtCHO} (diamonds) on PAc (filled symbols) and H_2 (open symbols) at 200 ºC and 1 atm total pressure for Pd-2-2nm (red symbols) and Pd-10-12.4nm (black symbols).Reactor conditions: 20% H_2/balance, total flow 200 sccm. For hydrogen kinetics ~ 1.0% PAc balanced with He.

The Arrhenius plot for the TOF of of Pd-10 (12.4nm) is shown in Figure 4.4. An apparent activation energy value of 11.7 ± 0.3 is found for C2H6/EtCHO production, which is same as observed in our previous detailed study of Pd-2 (2 nm) [146]. This again suggests a similar rate determining step for C2H6 and EtCHO production occurring on the Pd(111) and Pd(100) sites present in these catalysts.

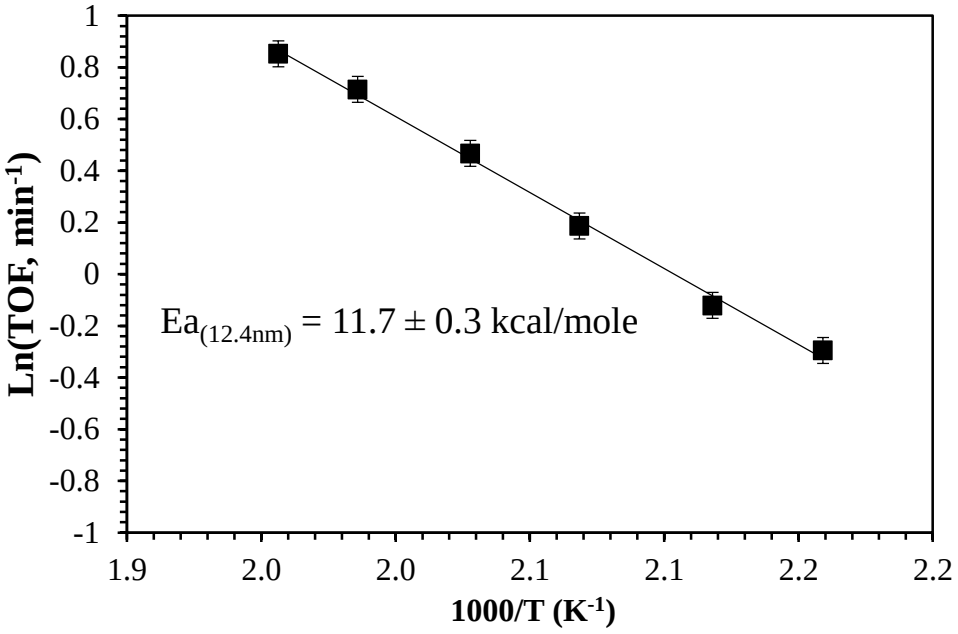

Figure 4.4: Arrhenius plots based on the total TOF of Pd-10 (12.4nm).Reactor conditions: 1 atm total pressure, ~ 1.0% Pac, 20% H_2, balanced He, total flow 200 sccm.

4.4 CONCLUSION

The present findings shed new light on the influence of metal particle size on the HDO of aliphatic carboxylic acids. Activity and selectivity trends for a family of Pd/SiO_2 catalysts at 200ºC revealed that PAc decarbonylation was the favored pathway over the entire particle size range studied (1.9-12.4 nm). While the reaction appears to be not strongly structure sensitive, some instructive trends in catalytic performance were observed. Smaller particles are less active but highly selective toward the formation of C_2H_6, whereas larger particles are more active but shift the selectivity partly toward EtCHO. These differences are attributed primarily to the differing composition of Pd crystal facets exposed in these catalysts, and suggest a means of tuning the selectivity through controlling particle size and shape. Current HDO studies in our laboratory are focusing on exploring

such particle size effects for other transition metals, as well as the use of bimetallic catalysts to enhance activity and stability.

CHAPTER 5

UNRAVELING THE MECHANISM OF PROPANOIC ACID HYDRODEOXYGENATION USING DEUTERIUM KINETIC ISOTOPE EFFECTS

5.1 INTRODUCTION

An extensive amount of research has explored the catalytic performance for the hydrodeoxygenation (HDO) of biomass-derived carboxylic acids and acid esters [151, 152]. Supported palladium is one of the most investigated catalysts in the area of catalytic hydrodeoxygenation of biomass derived platform molecules[42, 44-48, 109, 128-132]. For instance, early studies showed that supported palladium offers a strong activity and selectivity for the HDO of PAc[14, 133, 146, 153, 154]. While kinetic studies reveal overall reaction rates, reaction orders, and apparent activation barriers, they do not provide enough information for determining the fundamental elementary steps involved in the reaction mechanism[155, 156]. For HDO reactions, the network of these underlying steps is complex and not yet fully understood.

In our previous DFT studies,[157-159] the HDO of PAc was investigated over Pd (111) model surfaces. The elementary reaction steps involved in the decarbonylation (DCN) and decarboxylation (DCX) were identified from first principles. A microkinetic model was developed to determine the dominant pathway and rate-controlling steps under realistic reaction conditions of 200 ºC and low, medium, and high partial pressures of hydrogen (0.001, 1 and 30 bar) in the presence and absence of solvents. Our results suggest that under gas phase reaction conditions, DCN is favored over the DCX, while in the presence of

water, DCN and DCX mechanisms become essentially competitive.[157] This is in agreement with our experimental study of the gas-phase HDO of PAc over supported group VIII noble metals, where we found that on various metals the DCN pathway dominates.[160] Additionally, computations found that in all reaction environments, and at a low hydrogen partial pressure, dehydrogenation of the α-carbon in PAc is the primary rate-controlling step. With increasing hydrogen partial pressure, C-OH bond dissociation becomes most rate-controlling and the importance of C-H bond cleavage is diminished.[157] The dissociation of the C-OH bond is one of the key reactions in the DCN and was previously also identified as the rate-determining step for the HDO of acetic acid.[161, 162] Our studies, however, clearly suggest that at all conditions, dehydrogenation steps of the α-carbon of the acid have at least some importance for the HDO of the acid to hydrocarbons. Bateau et al. and Zhong et al. have also examined the deoxygenation of carboxylic acids over Pd [151, 163, 164]. They suggest that a carboxylate intermediate dehydrogenates, which is accompanied by C-O bond cleavage, resulting in CO and hydrocarbon formation by C-C bond cleavage.

Consequently, a deuterium kinetic isotope effect (KIE) to interpret the reaction mechanism of the catalytic HDO of PAc is described in this section. Kinetic Isotope Effects (KIE) has been studied extensively and provide valuable means to elucidate the reaction mechanism based on the transition-state for the rate-determining step of several organic reactions[165-169]. As early as 1933, published work by Eyring and Polanyi postulated that protonated and deuterated compound should react at different rates based upon the difference in their zero-point energy[170]. Later, Bigeleisen and Mayer, focused on the calculation of equilibrium isotope effects which was extended to include a KIE on reaction rates based on the transition-state theory. The theory postulates that the reactants on the

transition-state are in equilibrium, and can be derived as the difference in the Gibbs free energy when going from the ground state to the transition state of the reaction[171]. Thus, in a KIE, a perturbation of the reaction-rate results from the isotopic substitution at one position in the reaction molecule and are primarily due to changes in the vibrational modes as the reaction proceeds to the transition-state structure[172]. The KIE is expressed as the rate-constant ratio which is proportional to the reaction-rate and is defined by: KIE = k_H/k_D for the non-deuterated (unlabeled- k_H) and deuterated (labeled-k_D) molecule.

The present study explores the deuterium kinetic isotope effect (KIE) [165-170,171, 172] for the HDO of PAc in order to further confirm the importance of C-H bon cleavage in the reaction pathway. PAc substituted with deuterium at the α-carbon position (CH_3CD_2COOH) was deoxygenated over 5wt% Pd/C catalyst and its reaction rate compared with that obtained from unlabeled PAc (CH_3CH_2COOH). From these data, experimental rate constant ratio (k_H/k_D) was determined under various hydrogen partial pressures. Density functional theory (DFT) calculations were performed for labeled PAc and its intermediates on Pd(111) to obtain the reaction parameters of all the elementary steps involved. The DFT-derived parameters were then implemented in a microkinetic model that allowed prediction of k_H/k_D under the same conditions used for the experiments. The experimental and computational results are consistent with each other, and confirm the importance of C-H bond cleavage in governing the rates of HDO of PAc on Pd.

5.2 Experimental Methods

5.2.1 Materials and Catalyst characterization

The experimental conditions have been previously reported in detail and thus will only be discussed briefly[146]. Propanoic Acid (CH_3CH_2COOH, 99%) and propanoic acid-

2,2-d2 (CH_3CD_2COOH, 98%) were purchased from Alfa Aesar and Cambridge Isotope Laboratories, respectively, and used without further purification. The gases for the reactor studies were H_2 (UHP, 99.99%), He (UHP, 99.99%), ethane (CP grade, 99.99%) and Ar (UHP 99.99%) supplied by Airgas National Welders. The 5wt% Pd/C catalyst (CP-97, SA_{BET} = 615 $m^{2/}g$) was supplied by BASF and reduced *in-situ* at 350ºC. The dispersion and particle size of 5wt% Pd/C was determined by pulsed hydrogen titration of oxygen pre-covered sites utilizing a Micromeritics 2920 AutoChem II Analyzer.

5.2.2 REACTION EVALUATION

The reaction rate experiments were performed in a single pass, packed bed, plug flow reactor system connected to a GC system [146] (See diagram in chapter 2 section 2.4.1). The experiments were carried out under differential (<5%) conversion at 200ºC under atmospheric pressure. Two sets of experiments were conducted: (1) 1.2% PAc/20%H_2/balance He and (2) 1.2% PAc/5%H_2/balance He in a total flow of 50 sccm. This catalyst under these reaction conditions has previously been shown to be free of both external and internal mass transfer effects [146]. The reaction rate was determined based on the formation of product (which is proportional to the rate of acid disappearance) in μmol product formed/min·gcat. The turn over frequency (TOF) was determined based on the reaction rate per active site of the 5wt% Pd/C catalyst. Unlabeled and labeled PAc were kept in separate vapor-liquid equilibrium (VLE) saturators and the concentrations of the both acids (e.g. labeled and unlabeled) in the gas feed were set equal prior to starting the reaction. Once the reaction with unlabeled PAc reached steady-state, the reactor feed was switched to the labeled PAc. This process was cycled until steady state reaction was

attained for each species. In this way, the KIE can be determined as the ratio between the unlabeled and labeled reaction rates (i.e., k_H/k_D).

Measurements of the isotopic composition of the products were conducted by mass spectroscopy. To ensure only the products were analyzed by MS, the PAc (unreacted) was condensed in a cold trap (-55ºC) (As shown in figure 2.11 from chapter 2 section 2.4.1). This was verified by analyzing the gas effluent with gas chromatography to confirm only products such as C_2H_6 and CO were detected. The gas products (35 sccm) were diluted with argon carrier gas before being sampled by a Stanford Research Systems residual gas analyzer (RGA100) mass spectrometer with an electron multiplier. The detailed description of this apparatus and sampling procedure is included in the appendix D.1. The masses 29,30 and 31 were monitored to track various ethane species, while water, nitrogen, oxygen, hydrogen and argon were also monitored to rule out leakage. For the MS study the PAc conversion was increased (~10%) by adjusting the catalyst loading (0.9g). A detailed description of the computational method conducted by Dr. Heyden and Sina Betash is summarized in Appendix D.4.

5.3 Results and Discussion

5.3.1 Kinetic Isotope Effect Measurements

Figure 5.1A shows the results of the reaction rate over time during switching between unlabeled (CH_3CH_2COOH) and labeled (CH_3CD_2COOH) PAc at 200ºC and 1 atm with a reactor feed of 1.2% PAc/20% H_2/balance He. The reaction resulted in differential conversion (<5%) with a 100% selectivity toward C_2H_6, with CO indicating decarbonylation (DCN) as the major reaction pathway as described previously[146]. The reaction rates based on the products formed and TOF are summarized in Table 5.1. The

labeled PAc reaction rate (1.39±0.05 μmol/min·gcat) was calculated from the average of measurements between 45 and 50 hr on stream, while the unlabeled PAc reaction rate (1.61±0.16 μmol/min·gcat) was calculated from the average of measurements between 37 and 44 hrs on stream. Taking the ratio of these two values, the KIE effect was found to be k_H/k_D = 1.16 ±0.07. Given this small value, as a comparison, Figure 5.1B shows the measurement of acid feed concentration (labeled and unlabeled PAc) as a function of time during the same experiment. The feed concentration analysis were conducted every 2.5 hours to verify there was no change. The variability from labeled to unlabeled feed composition is around 3.0% and a mass balance between 0.99-1.01 is obtained. Given that the reaction order with respect to PAc is ~0.5 order under these conditions [146], such variability does not account for the observed rate difference. Nevertheless, this small ratio of k_H/k_D = 1.16 ±0.07, indicates that the isotopic substitution at the α-carbon position had little effect under these conditions.

In our previous DFT study, we performed a sensitivity analysis on HDO of propanoic acid over Pd (111) model surfaces, where our model suggested that by lowering the partial pressures of hydrogen, the influence of the dehydrogenation of α-carbon on the overall TOF will increase. To further explore the KIE effect and trend in its relationship with partial pressure of hydrogen, steady-state measurements at 200ºC and 1 atm total pressure were conducted at lower hydrogen partial pressure. Figure 5.2A shows reaction rate data as a function of time during switching between unlabeled and labeled PAc using a feed consisting of 1.2% PAc/5% H_2/balance He, The labeled PAc reaction rate (0.80±0.09 μmol/min·gcat) was calculated from the average of measurements between 16 and 19 hr on stream, while the unlabeled PAc reaction rate (1.28±0.15 μmol/min·gcat) was calculated

from the average of measurements between 19.5 and 22 hrs on stream. A k_H/k_D ratio of 1.62 ±0.05 is obtained, suggesting that a significant KIE is present at this lower partial pressure of hydrogen. Once again, Figure 5.2B shows the measurement of acid feed concentration as a function of time during the same experiment revealing negligible variation. The significant KIE therefore indicates that the rate controlling step involves dehydrogenation of the α-carbon (i.e., C-H bond breaking). Indeed, a lower partial pressure of hydrogen should allow for the dehydrogenation of the α-carbon to occur to a greater extent, accounting for the increased KIE.

Table 5.1: Deuterium isotope effect for PAc HDO over 5wt% Pd/C, 16.9%, 6.8nm. Reaction conditions: 200ºC and 1 atm, Total flow: 50 sccm. <5% conversion, 100% selectivity C_2H_6. a Rxn rate - μmol/min·gcat. Rxn 1- CH_3CH_2COOH/H_2, Rxn 2= CH_3CD_2COOH/H_2.

	X_{H2}/bal. He:							
	20% H_2/balance He				**5% H_2/balance He**			
Rxn	Feed conc. (*%PAc*)	Rxn rate[a]	*TOF* *(min^{-1})*	k_H/k_D Exp.	Feed conc. (*%PAc*)	Rxn rate[a]	*TOF* *(min^{-1})*	k_H/k_D Exp.
1	1.19± 0.02	1.61± 0.16	0.020± 0.002	1.16± 0.07	1.22± 0.02	1.28± 0.15	0.016± 0.002	1.62± 0.05
2	1.16± 0.03	1.39± 0.05	0.018± 0.002		1.23± 0.01	0.80± 0.09	0.010± 0.001	

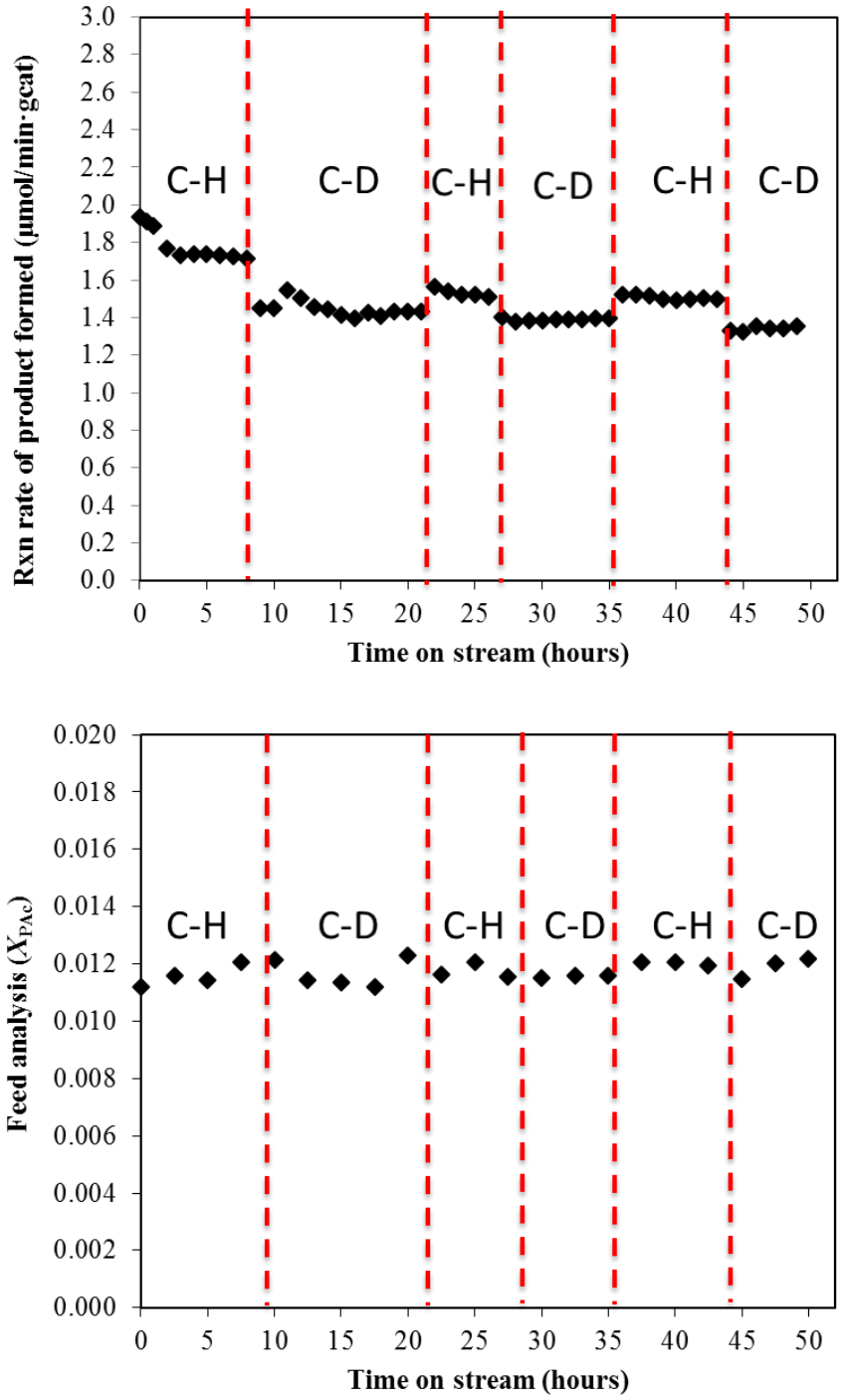

Figure 5.1: Steady-state measurements for the reaction rate of the labeled/unlabeled PAc HDO.~1.2% PAc, 20% H_2/balance He. C-H and C-D denotes unlabeled and labeled reaction rate, respectively.

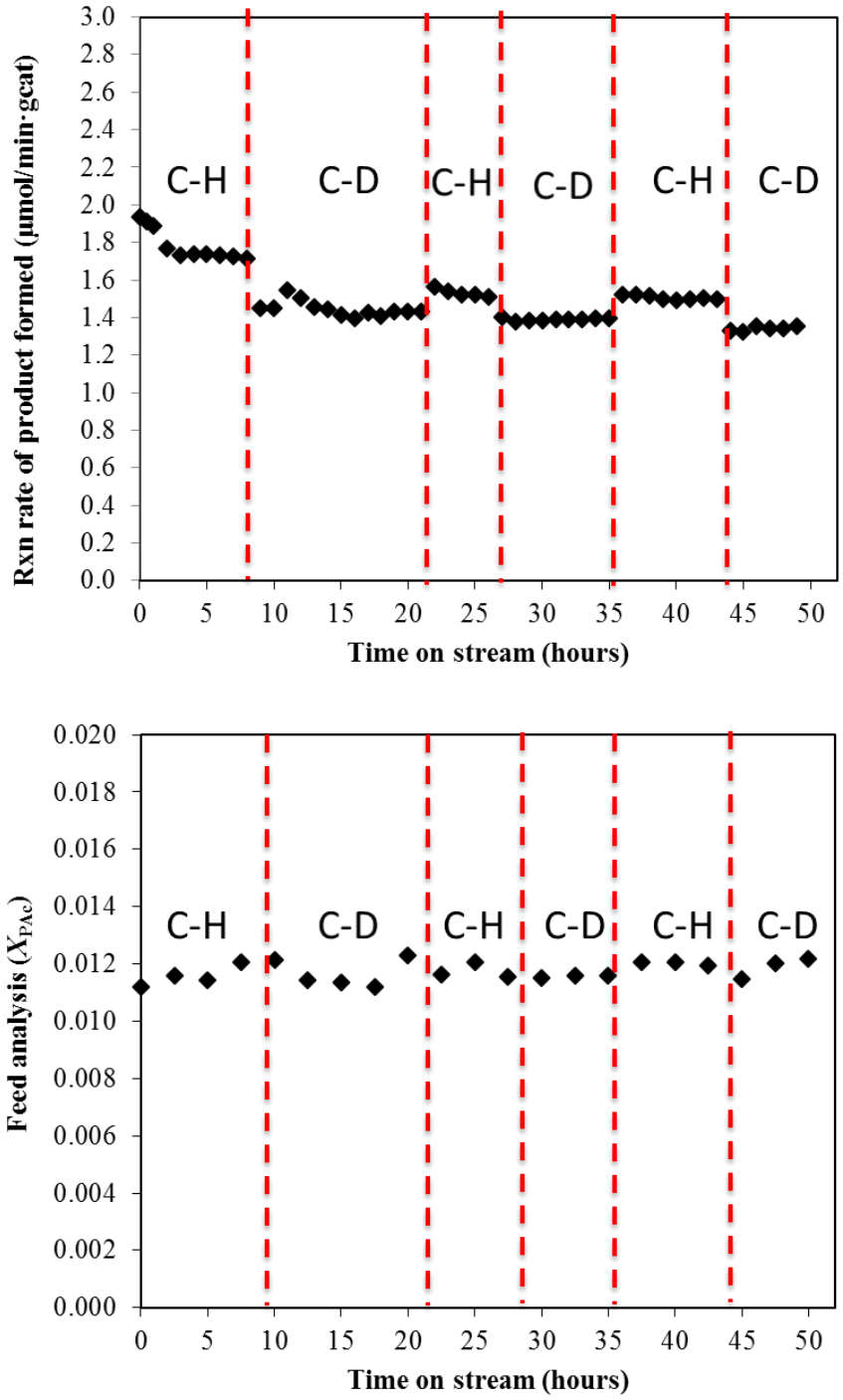

Figure 5.2: Steady-state measurements for the reaction rate of the labeled/unlabeled PAc HDO.~1.2% PAc, 5% H_2/balance He. C-H and C-D denotes unlabeled and labeled reaction rate, respectively.

5.3.2 KINETIC ISOTOPE EFFECT CALCULATIONS

The positive experimental KIE values obtained above point to the kinetic importance of α-carbon dehydrogenation in the HDO of PAc. According to our previous DFT studies[157, 158], we know that the dehydrogenation of the α-carbon is not the only rate-controlling step under the investigated reaction conditions of 200ºC and partial pressures of 0.01 bar of acid and 0.05 bar of H_2. Indeed, the observation that the k_H/k_D ratio varies under different reaction conditions appears to be similar to the changes in the computed degree of rate control[173] of the α-carbon dehydrogenation. Thus, the interpretation of the observed KIE is not straightforward. To initially obtain a meaningful range for the KIE in our system, two limiting theoretical cases were considered. In Section 5.3.2A, an upper limit for the KIE is predicted for the case where α-carbon dehydrogenation is the only rate-controlling step. While labeling PAc could in principle affect other rate-controlling steps through a so-called secondary kinetic isotope effect, this is also shown to be negligible in this system for the limiting case of C-OH bond dissociation being the rate limiting step. Secondly, Section 5.3.2B presents a detailed DFT and microkinetic modeling study to estimate the KIE under reaction conditions for a Pd (111) surface from first principles. A secondary kinetic effect is also calculated and reported in detail in Appendix D.4

5.3.3 UPPER LIMIT FOR THE PRIMARY KINETIC ISOTOPE EFFECT

Assuming that the dehydrogenation of the α-carbon is the only rate controlling step in the HDO of PAc, the ratio of the turn over frequencies of CH_3CH_2COOH and CH_3CD_2COOH can be approximated using transition state theory[174-176] as:

$$\frac{TOF_{CH_3CH_2COOH}}{TOF_{CH_3CD_2COOH}} \approx \frac{k_H}{k_D} \approx \frac{e^{\frac{-(E_a+\Delta ZPE_H)}{K_BT}}}{e^{\frac{-(E_a+\Delta ZPE_D)}{K_BT}}} = e^{\frac{-h}{2K_BT}\nu_H(\frac{\nu_D}{\nu_H}-1)}$$

where E_a is the activation barrier, ΔZPE_H is the zero-point energy correction to the activation barrier for the unlabeled PAc, ΔZPE_D is the zero-point energy correction to the activation barrier for the labeled PAc, k_B is the Boltzmann constant, T denotes the temperature, *h* is the Planck constant, and ν_H and ν_D are the C-H and C-D vibrational frequencies, respectively, in PAc.

The maximum C-H frequency observed in carboxylic acids[177] is 3000 cm^{-1}. In addition,

$$\frac{\nu_D}{\nu_H} \approx \sqrt{\frac{\mu_H}{\mu_D}} \quad , \quad \frac{1}{\mu_H} = \frac{1}{m_H} + \frac{1}{m_{CH_3CHCOOH}} \quad , \; and \; \frac{1}{\mu_D} = \frac{1}{m_D} + \frac{1}{m_{CH_3CDCOOH}}$$

where μ_D and μ_H are the reduced masses for $CH_3CDCOOH$-D and $CH_3CHCOOH$-H, respectively, and m_H, m_D, $m_{CH3CHCOOH}$, $m_{CH3CDCOOH}$ are the molecular masses in g mol^{-1} of H (1), D (2), $CH_3CHCOOH$ (73), and $CH_3CDCOOH$ (74), respectively. Combining equations (10) with equation (9) then yields the the maximum KIE = $\frac{TOF_{CH_3CH_2COOH}}{TOF_{CH_3CD_2COOH}}$ is calculated to be 3.73. This value is considerably (by over a factor of two) than that observed experimentally, suggesting that α-carbon dehydrogenation is not the only rate-controlling step. The DFT and microkinetic modeling study explaining the computational KIE is summarized in appendix D.4. A comparison between the experimental, calculated and computational is summarized in table 5.2.

Table 5.2: Comparison of KIE values based on experimental, calculated and theoretical approach. * based on the Upper Limit for the Primary Kinetic Isotope Effect calculations.

Gas phase comp. 1.2% PAc/5% H_2/balance He		
$\boldsymbol{k_H/k_D}$	k_H/k_D	k_H/k_D
Experimental	*Theoretical(comp.)*	*Calculated**
1.62	1.49	3.73

5.3.4 Extent of Dehydrogenation

Given the confirmation of α-carbon dehydrogenation as an important rate controlling step, the extent of this step under actual reaction conditions was further probed experimentally. Mass spectrometric analysis was performed on the reaction products formed for the HDO of labeled and unlabeled PAc, since GC cannot distinguish between various deuterium-labeled ethane products. Masses corresponding to CH_3CH_3 (m/e = 30), CH_3CDH_2 (m/e = 31), and CH_3CD_2H (m/e = 32) were considered. If one C-D bond is broken at the rate-determining step, the product CH_3CDH_2 should be detected. Similarly, if two C-D bonds are broken at the rate-determining step, the product CH_3CH_3 is detected. Lastly, if there is no C-D bond broken at the rate determining step, the product CH_3CD_2H is detected. The latter, however, was not able to be detected since it overlapped with a background of signal at m/e = 32 arising from oxygen in the MS chamber.

Nevertheless, it is highly unlikely that this species was formed, given that it requires C-C bond breaking to occur to form a CH_3CD_2 fragment before H addition, which is not favorable. Since, according to our DFT calculations, the C-C bond dissociation in deuterated propanoyl (Reaction 3: $CH_3CD_2CO^{***} \rightarrow CH_3CD_2^* + CO^* + *$) has the

activation barrier of 0.99 eV while, with de-deuteration of propanoyl the activation barrier of C-C bond dissociation (Reaction 14: $CH_3CCO^{***} \rightarrow CH_3C^* + CO^* + *$) was lowered to 0.47 eV, suggesting that most likely propanoic acid or propanoyl go through dehydrogenation steps prior to C-C bond dissociations. In this context, if CH_3CD_2 would be a dominant product, no KIE would be observed; however, we observe a clear primary KIE. No H-D exchange between H_2 and CH_3CD_2COOH in the chemisorbed state is assumed.

Analysis of the mass spectrum recorded for the HDO of labeled PAc (Figure D.1 and D.2) shows that both CH_3CDH_2 and CH_3CH_3 are produced (see appendix D.2 for detailed description). As can be seen from Table 5.3, the CH_3CDH_2:CH_3CH_3 ratio is 1:2. Thus, C-C bond rupture in CH_3-CH_2-COOH is favored by a factor of two after both hydrogens of the α-C-H have been broken (see appendix D.3). These results also strongly support the idea that C-H bond-breaking occurs before C-C rupture. Additionally, our microkinetic modeling results suggest that the α-carbon gets fully dehydrogenated, as our main products are predicted to be CH_3CH_3, and the only detuerated product was identified to be CH_3CDH_2 where the ratio of the TOF of formation of CH_3CDH_2 to CH_3CH_3 was estimated to be 0.02.

Table 5.3: Distribution of CH_3CH_2D and CH_3CH_3 during the HDO of labeled PAc a using the m/e = 31 intensity, the other two m/e intenstities arising from CH_3CH_2D were calculated using the published fragmentation pattern of Amenomiya and Pottie.

	Description	*m/e = 29*	*m/e = 30*	*m/e = 31*
1	**Experimental intensities for HDO of labeled PAc**	1.63E-09	9.28E-10	3.51E-10
2	**Calculated intensities of CH_3CH_2D fragments[a]**	1.11E-09	2.56E-10	3.51E-10
3	**CH_3CH_2D fragmentation ratio from literature[b]**	3.17	0.73	1.00
4	**Calculated intensities of CH_3CH_3 fragments[c]**	5.17E-10	6.72E-10	
5	**Calculated CH_3CH_3 fragmentation ratio**	0.77	1.00	
6	**Published CH_3CH_3 fragementation ratio[b]**	0.76	1.00	
7	**Experimental intensities for HDO of unlabeled PAc**	3.09E-10	4.22E-10	
8	**Calculated CH_3CH_3 fragmentation ratio**	0.73	1.00	

5.4 CONCLUSION

The HDO of PAc catalyzed by 5wt% Pd/C was examined and compared with deuterated labeled PAc reaction. A normal KIE 1.62 is observed, indicating that dehydrogenation of the α-carbon is one of the rate-controlling step. This is confirmed by computational DFT calculations where a KIE of 1.49 is obtained. Based on the good agreement between the experimental and computational approach, insights for the depth of dehydrogenation is

measured by mass spectroscopy. Therefore, it is concluded that HDO that occurs mainly via DCN pathway; (C-C) rupture, occurs favorably if both of the α-C-H bonds are broke.

CHAPTER 6

GAS-PHASE, CATALYTIC HYDRODEOXYGENATION OF PROPANOIC ACID, OVER CARBON SUPPORTED TRANSITION STATE METALS: METAL ACTIVITY AND SELECTIVITY TRENDS

6.1 INTRODUCTION

Catalytic biomass conversion to fuels and chemicals is considered one of the important avenues to help to mitigate the expected shortage of fossil carbon resources and the environmental impacts of their use [152, 180, 181]. A limiting factor is the search for new biomass conversion catalysts that are both technologically and economically viable for this application. The catalytic HDO of bio-oils and fatty acid has been reported extensively by many authors [10, 42, 44-51, 102, 104-109, 128-133]. These bio-oils contains large amounts of carboxylic acids (e.g., acetic acid, propanoic acid) that decrease stability, are highly corrosive, and are challenging to deoxygenate [128]. Most studies have focused primarily on measurements of activity and selectivity, while a few have examined more fundamental kinetic parameters such as reaction rate orders and activation energies [182]. Many of these studies [183] have been conducted in large fatty acids (>C12), with much less attention [111, 151] given to HDO of small fatty acids (e.g., acetic and propanoic) found in pyrolysis oils derived from lignocellulosic biomass. Recent work from Joshi and Lawal on HDO of acetic acid over NiMo catalyst in a microreactor [184] revealed that vapor phase

acetic acid showed higher conversion (at 200-450ºC) than liquid phase acetic acid. Additionally, work from Zhu et al. on the aqueous-phase HDO of propanoic acid over ZrO_2-supported Ru and Ru-Mo catalysts exhibited good activity and selectivity towards methane and ethane [185]. However, very few studies on the gas-phase catalytic HDO of these small acids over group VIII noble metals have been reported [78, 111, 146].

In our previous report the catalytic activity and selectivity for the HDO of propanoic acid (PAc) were studied on group VIII noble metals supported on SiO_2 [146]. Here we extend these investigations to the HDO of PAc carbon-supported group VIII noble metals, including the activity and product selectivity as a function of temperature and the reaction rate orders with respect to the reactants.

6.2 Experimental Methods

6.2.1 Chemicals, Catalyst preparation and characterization

Propanoic acid (CH_3CH_2COOH, 99%) was purchased from Alfa Aesar, while H_2 (UHP grade) and helium (UHP grade) were supplied by Airgas National Welders. The catalysts consisted of: Pd, Pt, Rh, Ru, Ir, Ni, Ag, Au and Cu supported on carbon (CP-97, surface area 615 m^2/g, purchased from BASF). 5wt% Pd, 5wt% Pt and 2wt% Rh/C were purchased from BASF and used as received. 2.2wt% Ru/C was synthesized by strong electrostatic adsorption (SEA), where the pH of the metal salt complex solution (500 ppm of $Ru(NH_3)_6Cl_3$, 98% Sigma Aldrich) was controlled based on the potential of zero charge (PZC) of the carbon [87]. 2wt% Ir, Ni, Au, Ag and Cu/C were synthesized by conventional incipient wetness (IW) method. The salt precursors were: iridium(III) chloride (99.8%, Sigma Aldrich), nickel(II) chloride hexahydrate (>98%, Sigma Aldrich), gold(I) potassium cyanide (99.9% Alfa Aesar), silver nitrate (99.9%, Alfa Aesar) and Copper(II) nitrate

hydrate (99% Sigma Aldrich). After SEA or impregnation, the catalysts were dried overnight, and pre-treated at different conditions in 20% H_2/balance He (as described in Table 1). The final treatment stage prior to reaction involved *in-situ* reduction in 20% H_2/balance He for 2 hours at temperature ranging from 350-400ºC.

The catalysts were characterized by chemisorption (H_2 titration of O_2 pre-covered catalyst) with a Micromeritics 2920 AutoChem II Analyzer to determine metal dispersions. The catalyst (0.10 g) were reduced (at the conditions in Table 6.1) by flowing 20% H_2/balance He, for 2 hrs, followed by purging with Ar for 1 hr to remove the physisorbed hydrogen. After cooling to 40 ºC in flowing Ar, the catalysts were exposed to 10% O_2/He for 30 min followed by purging with Ar for 30 min. Titration with pulses of 10% H_2/Ar was then employed until no further H_2 uptake occurred. The dispersion and particle size are summarized in Table 6.1.

Atomic absorption spectroscopy (AAS) experiments were conducted on a Perkin Elmer 3300, to determine the actual metal loadings of catalysts. An acetylene/air flame was used for all analyses. For each metal, a calibration curve was prepared utilizing standards previously prepared. Samples of catalyst was placed in aqua regia and digested in an oven at 120ºC for 5-7 hours, followed by cooling and dilution with 10% HCl/0.5% $LaCl_3$ solution up to a volume of 25 mL. An aliquot of the solution was separated in a 12 mL vial and set up for the AAS experiment. For 2.2wt% Ru/C, the metal loading was analyzed by inductively coupled plasma (ICP) on a Perkin Elmer Optima 2000. The sample metal salt complex solution was analyzed before and after the SEA, the difference in concentration, allow us to determine the metal loading of Ru/C. Details of the procedure were described previously [146].

Table 6.1: Physical and chemical properties of M/carbon. [a] Dispersion and particle size obtained by chemisorption (O_2-H_2 titration). – dispersion and particle size not obtained.

Wt%	Metal	Reduction cond. (ºC)	Dispersion[a] (%)	Particle size (nm)
5	Pd	350	17.0	6.8
5	Pt		25.0	4.5
2	Rh		8.0	13
2.2	Ru		27.0	4.8
	Ir		7.0	14
	Ni		5.3	19.2
2	Ag	400	-	-
	Au		-	-
	Cu		-	-

6.2.2 CATALYST EVALUATION

All activity and kinetics measurements for the HDO of PAc over M/carbon were carried out between 200-400ºC and atmospheric pressure. The reaction rate orders and TOF were determined at 200ºC. The screening experiments were carried out in a single pass, packed bed, plug flow reactor system. The catalysts were reduced *in-situ* at a total flow of 50 sccm H_2 for 2 hours. The feed stream consisted of: 1.1% PAc, 20% H_2, balances He. In order to determine the reaction rate orders, the kinetic experiments were conducted at PAc and H_2 concentrations ranging from X_{PAc} ~ 0.0020-0.017 and X_{H2} ~ 0.20-0.99. A detailed description of the reactor system have been described previously [146]. The

conversion and selectivity for a given catalyst was defined according to the following equations from chapter 3 section 3.2.4. Internal/external mass transport limitations studies were performed over 5wt% Pd/C at the described conditions (200ºC, 1 atm) and have been reported previously [146]. No internal and external mass transport limitations was found for the catalyst. Since the same carbon support (CP-97) is used for all catalyst, the same mass transport conditions is assumed.

6.3 Results and Discussion

6.3.1 Temperature effect on activity and selectivity

Before analyzing the HDO of PAc on various M/C catalysts, the activity and selectivity of the carbon support were explored in the temperature range 200-400ºC. The support showed no activity until 300ºC where some activity (~1.0% conv.) to ethane was observed. Higher conversion (10-23%) was observed when temperature reached 350ºC-400ºC, with the selectivity mainly toward ethane (78%). At the higher temperatures (400ºC), other minor products were detected such as: propylene/propane (12% sel.), n-butane (7%) and propionaldehyde (EtCHO - 3% sel.). The M/C (M =Pd, Pt, Rh, Ir, Ru, Ni, Ag, Au, Cu) catalysts were then investigated under the same conditions.

Comparisons with 5wt% Pd/C were made and results are reported in previous work in chapter 3, section 3.3.3. The conversion-temperature light-off curves are summarized in Figure 6.1, with a temperature profile ranging between 200-400ºC for all the catalysts. The selectivities towards various types of products are summarized in Figure 6.2 for each temperature studied. They are classified based on the types of main products formed, with C1 (methane-through eventual cracking) and C2 (mainly ethane) generated from

decarbonylation (DCN) and decarboxylation (DCX) pathways, while C3 (mainly propane) and propionaldehyde (EtCHO) are formed from hydrogenation.

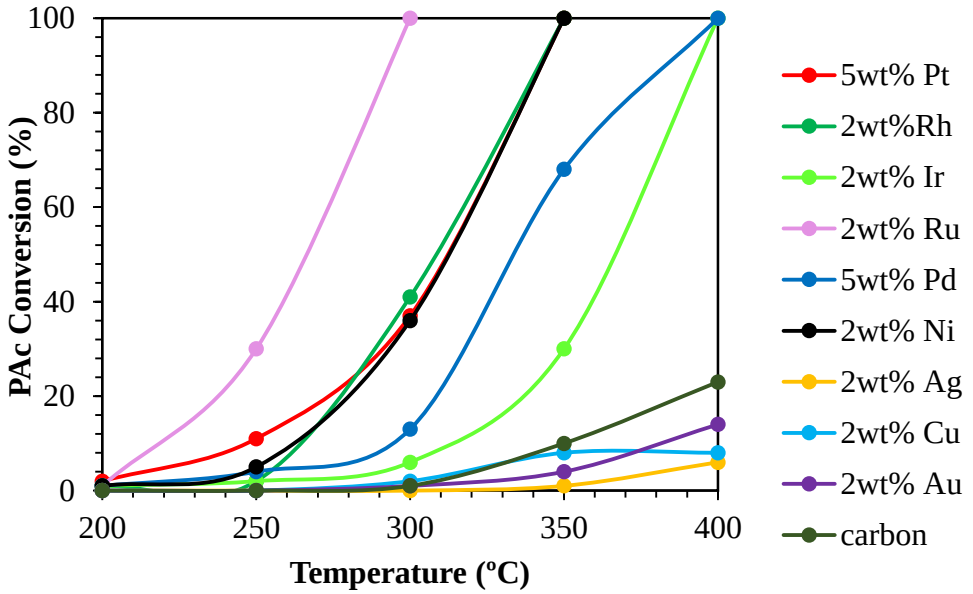

Figure 6.1: Conversion of PAc based on product formed (%) as a function of temperature. Reaction conditions: 1.2% PAc, 20% H_2/balance He. Total flow = 50sccm.

The activity and selectivity of 5wt% Pt/C are very similar to that of Pd/C, with complete conversion reached at 350ºC (Fig. 1). At 200ºC only C2 and CO are observed, but as the temperature increases to 300 and 350ºC, traces of C1 and C3 (7% and 3%, respectively) were detected. The results indicate mainly the DCN reaction, however at 300 and 350ºC, the DCX reaction pathway is observed based on the formation of CO_2.

Analogous to Pt and Pd, the 2wt% Rh/C was very selective toward C2 up to 250ºC. But as the temperature increased (300-350 ºC), the product distribution switched to favor C1 (sel. 89%) with complete conversion at 350ºC. The large formation of C1 is likely due to cracking of ethane or methanation at the higher temperatures. However, no methanation experiments were conducted for this catalyst. It is noted that at the higher temperatures (>300ºC), DCX is the main reaction pathways based on the formation of CO_2. An analysis

was conducted to verify if water-gas shift (WGS) reaction was present. Calculations based on the WGS equilibrium constant of K_{eq} ~ 38.1, 19.9 and 11.5 at 300, 350 and 400 ºC[121], respectively, allowed to determine the maximum amount of CO_2 produced by WGS. At 300ºC and 350ºC only 4% and 2%, respectively, of the CO_2 observed accounts for WGS. Thus, at 300-350ºC, the formation of CO_2 is primarily due to DCX with negligible WGS reaction.

DCX reactions are highly desired since in principle there is no overall consumption of hydrogen. Previous work for the HDO of PAc carried out over Rh/SiO_2, (see Chapter 3 Section 3.3.2) showed that at 300-350ºC only the formation of C2 hydrocarbons was detected (no C1-methane was observed). Thus, for rhodium over the carbon support, the HDO of PAc reaction is more prone to cracking and/or methanation at the temperature range 300-350ºC. For the 2wt% Ir/C catalyst a high selectivity toward C2 (sel. 100%) at 200ºC was observed. As the temperature increased up to 400ºC, the product distribution changed toward C1 (sel. 73%), which is also attributed to cracking and/or methanation. However, in this case, DCN is the main reaction pathway up to 400ºC where complete conversion is reached.

For the reactions with 2.2wt% Ru and 2wt% Ni over carbon, at 200ºC, the main products are C1 (sel. 35% for Ru and 32% for Ni) and C2 (sel. 64% s for Ru and 68% for Ni). However very low activity (1% conversion) is observed. As the temperature increases, both catalyst, showed preference to produce C1. For Ru, complete conversion was reached at 300ºC where the main product is C1 (sel. 91%). For Ni, complete conversion was reached at 350ºC producing only C1 (sel. 100%). Moreover, at 200ºC, small traces of C3 (~1%) was detected, revealing that some hydrodeoxygenation/hydrogenation is occurring

for the formation of C3. Methanation experiments conducted in previous work (conditions: 1% CO/20% H_2/balance He.) over Ru and Ni/SiO_2 indicated that between 250-350ºC, a 5-18% conversion to produce C1 was obtained (see appendix B.3). Additionally, in terms of activity and selectivity at 200ºC, Ru/SiO_2 also favored the formation of C1 (sel. 72%). In contrast to Ru/C, where C1 is the main product, at 350ºC, the formation of C1 over Ru/SiO_2 decreases significantly to 38%. Moreover, the low activity of Ni/C is also consistent with our previous study over Ni/SiO_2, where a low activity is observed at 200ºC (<1% conv.). Conversely, for the silica supported Ni, as the temperature increases to 350ºC, C2 (sel. 71%) and C3 (sel. 9%) are the main products, where only traces of C1 (sel. 9%) are observed.

Based on this, it can be concluded that over carbon-support, cracking and methanation reactions are more inclined to happen over the temperature range. Chen et al. studied the HDO of PAc in the aqueous phase over Ru/C [185]. Likewise, they observed significant amounts of methane and ethane. As the temperature was increased, the selectivity toward C1-C3 increased. Diffuse Reflectance Infrared Fourier Transform Spectroscopy (DRIFTS) studies conducted for PAc over Ru/C between 200-210ºC, showed a band at 3017 cm^{-1} assigned to adsorbed CH_4 appeared. Moreover, they performed methanation experiments, and found high methanation activity of CO on the Ru catalyst. Consequently, it is evident that aqueous or gas phase HDO of PAc over Ru/C favors methanation reactions. Similar to the Ni/C experiments, Murzin et al. showed that the liquid-phase deoxygenation of stearic acid over 16wt% Ni/Al_2O_3 at 300ºC and 6 bar favored cracking reactions as compared to other catalysts[133].

For the case of 2wt% Ag, Au and Cu, no activity was observed at 200ºC. For Au and Cu some activity is observed by 300ºC, where the main product formed was C2 (sel. 76% for Au and 70% for Cu) with <2% conversion. Interestingly, a significant amount of EtCHO is also observed at 300ºC (sel. 24% for Au and 29% for Cu). At 400ºC the conversion for Au and Cu reaches 14% and 8%, respectively. The selectivity remained mainly to C2 (sel. 91% for Au and 94% for Cu), and the selectivity of EtCHO decreased significantly (sel. 6% for Au and 3% for Cu), indicating EtCHO underwent DCN to produce C2. Traces of C1 (sel. 3% for Au and 4% for Cu) formed from cracking were also observed, however, this activity is inherent to the carbon support (see light-off curves, Figure 1). As described above, based on the product distribution of the carbon support (Figure 2), at 300ºC, the selectivity toward C2 and EtCHO is 83% and 16%, respectively with a low conversion (1%). As the temperature increases to 400ºC, a conversion of 23% is reached, indicating, once again, that the products formed over 2wt% Au/C and Cu/C are mainly based on the activity of the support. For the reaction over 2wt% Ag/C, no activity was observed up to 350ºC (1% conv.), where C2 (sel. 85%) corresponded to the main product. Minor products were also observed such as C1 (sel. 4%), C3 (sel. 8%) and EtCHO (sel. 2%). At 400ºC the conversion increased to 10% where C2 (sel. 85%) remained the main product. Once more, the conversion is less than 23% (carbon support conversion), indicating that the activity comes mainly from the support.

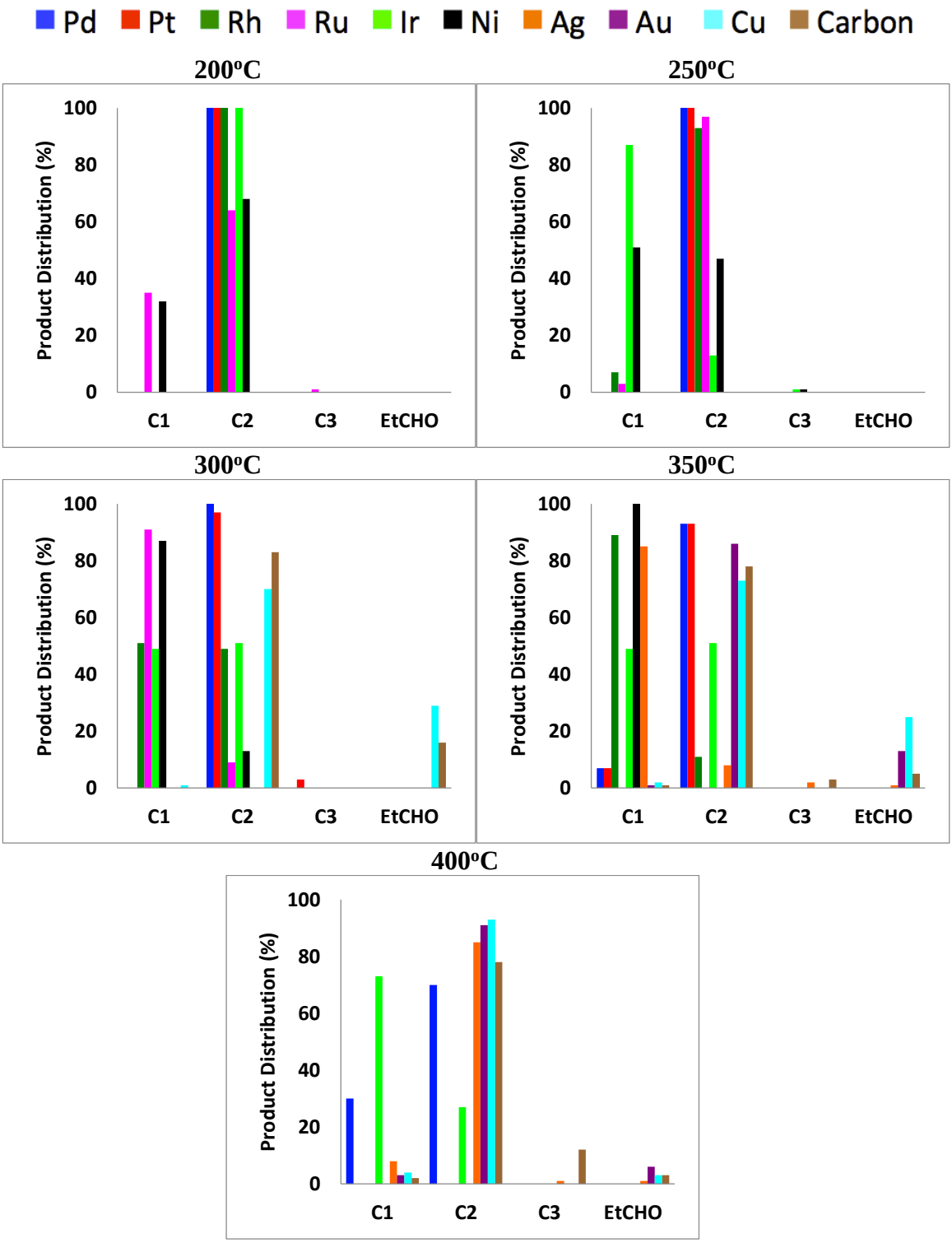

Figure 6.2: Product distribution of all catalysts between 200-400°C. C1 denotes methane, C2 denotes ethylene and ethane, C3 denotes propane and EtCHO denotes propionaldehyde.

To investigate and compare the intrinsic activity of each catalyst, experiments were conducted at 200 ºC and 1 atm under differential conversion. Table 6.2 summarizes the reaction product distribution (selectivity), turnover frequencies (TOF, molecules•site^{-1}min^{-1}) and reaction rate order with respect to PAc and H_2 (see following section). It was observed, that at 200ºC, the best activity for the HDO of PAc was achieved with 2wt% Rh/C. The catalyst perfomance followed the sequence: Rh=Pt > Ir > Ru=Ni=Pd, where no activity was detected for Au, Ag and Cu at 200ºC.

Similar screening studies have been conducted by Xu and Olcay where the activity trends of the aqueous-phase HDO of acetic acid (AAc) were measured over transition metal catalysts including: Ru, Pt, Pd, Rh, Ir, Ni and Cu[187]. The study was carried out at temperatures ranging 110-290 ºC and 5.17 MPa pressure. Their investigation indicated that the TOF of AAc decreased in the order: Ru > Rh ≈ Pt > Pd ≈ Ir > Ni > Cu where ethanol is the main product. The activity trend is very similar to our study, except that of Ru (showed to be the most active). Based on their computational calculations (DFT), the difference in the activity could be due to the intrinsic reactivity[188] of the metals to dissociate AAc to acetate (CH_3COO^-) and acetyl (CH_3CO). Their findings indicated that the rate-limiting step depends on the acetyl formation which was favorable in all catalysts except for Cu. The catalytic activity was empirically correlated to the acetyl binding energy to the surface of metals. The higher the binding energy with the metal, the higher the TOF. In addition, Cu, Ag and Au belong to the same element group (IB) that has been shown to have very poor activity for deoxygenation[187]. Our previous work on the HDO of PAc over 5wt% Pd/C, has demonstrated that the formation of propanoyl (which requires C-OH bond

cleavage) is in fact a significant rate-limiting step, thus, the propanoyl binding is somewhat important.

Along these lines, Dumesic and co-workers conducted DFT theory studies of EtCHO and acetone hydrogenation over Pt(111)[209]. They observed a lower rate for the hydrogenation EtCHO over Pt as compared to acetone. The lower rate was attributed to the formation of strongly absorbed propanoyl species (removal of α-H atom). If this is the case, the propanoyl species would then block Pt(111) surface sites. In comparison to our work, if the catalyst under investigation, has a strong adsorption of propanoyl species on the metal surface, it would be difficult for the intermediate species to transform and undergo the desired chemical reaction. The adsorption energy must be high enough to attract the reactant to the surface, but not so high that would impede the reaction product to desorb.

Table 6.2: Reaction rate conditions observed at 200ºC and 1 atm pressure. Conversions and preferred reaction pathways are (1-2%) and DCN, respectively, for all catalysts. Reaction conditions: 1.2% PAc, 20% H_2/balance He. Total flow = 50sccm. Au, Ag and Cu showed no activity at 200ºC

Metal/carbon	Product distribution, selectivity (%)				TOF (min^{-1})	Reaction rate order	
	C1	C2	C3	EtCHO		XPAc	XH_2
Pd					0.0102	0.44	0.06
Pt	0	100	0	0	0.0371	0.56	0.01
Rh					0.0375	0.39	0.01
Ru	35	64	1	0	0.0134	0.38	0.02
Ir	0	100	0	0	0.0219	0.49	0.03
Ni	32	68	0	0	0.0129	0.20	-0.22

6.3.2 KINETIC STUDIES OF M/CARBON

The reaction rate orders were determined based on the power rate law model. The reaction orders were obtained from the slope of ln reaction rate vs. ln mole fractions of PAc and H2 (XPAc and XH2, respectively). Figure 6.3 shows the plots for M/carbon catalysts (M = Pd, Pt, Rh, Ir, Ru, and Ni). For most catalysts, except for Ni, the reaction rate orders in PAc and H2 are approximately 0.5 and 0, respectively, over the range of concentrations examined. The reaction rate order with respect to PAc and H_2 is consistent with the HDO of PAc conducted previously over Pd supported over C, SiO_2 and TiO_2 described in Chapter 3.

At 200ºC decarbonylation is the dominant deoxygenation pathway based on the formation of CO for all the catalyst. The experimental observation is consistent with the computational studies of Heyden[121] for the DCX and DCN of PAc over Pd(111) model surfaces. Heyden's computations indicated the most kinetically-favorable pathway was decarbonylation and the rate controlling steps included dehydroxylation of PAc (C-OH bond cleavage) to produce propanoyl (CH_3CH_2CO), and α carbon dehydrogenation to form C_2 hydrocarbons. Further analysis have been explained in previous studies in chapter 3. The rate-controlling step is dependent upon the ability to remove the hydrocarbon pool (CH_3CH_x) from the surface. For H_2, the reaction order of zero implies a high coverage of hydrogen on the Pd surface, relative to PAc reaction intermediates. For Ni/C a reaction rate order of 0.15 and -0.18 with respect to PAc and H_2 is observed. The negative reaction rate order with respect to H_2 indicates that hydrogen adsorbs strongly and competitively at the surface, which impedes PAc to absorb and react. Thus, competitive adsorption between

PAc and H_2 is taking place, inhibiting PAc to react at the surface. This could be one reason for the reaction rate order of PAc with respect to be between ~0-0.5.

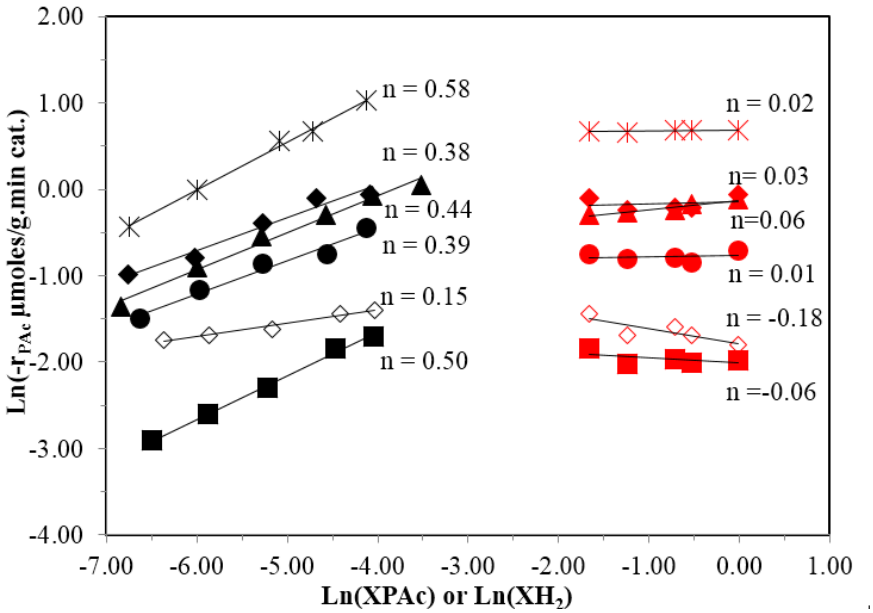

Figure 6.3: Reaction rate order with respect to PAc(black symbols) and H2(red symbols) for: (▲)Pd, (*)Pt, (●)Rh, (♦)Ru, Ni(◊) and (■)Ir. Reaction conditions: 200ºC and 1atm, total flow = 50 sccm. Mass catalyst = 0.20g.

6.4 CONCLUSION

Group VIII noble metals catalyst supported on carbon were screened for HDO of PAc as a bio-oil model compound. The screening was performed in a temperature range between 200 and 400ºC at 1atm pressure. The HDO of PAc proceeded mainly through: (1) direct hydrogenation, DCN and DCX over Pd, Pt, (2) DCN and methanation over Rh, Ir, Ru and Ni and (3) at higher temperatures (>300ºC), hydrogenation to form aldehyde and DCN over Au, Ag, and Cu. Rh/C showed the highest activity (based on the TOF) for the HDO of PAc. For all catalysts, except Ni, the reaction rate order with respect of PAc and hydrogen is half and zero order, respectively. Ni/C showed a reaction rate order with respect of PAc and hydrogen of 0.2 and -0.2, respectively. This indicate that the presence of hydrogen inhibits the reaction rate.

CHAPTER 7

CONCLUSION AND PROPOSED FUTURE WORK

7.1 CONCLUSION

The investigations herein set out to explore the hydrodeoxygenation (HDO) of biomass-derived molecules for upgrading pyrolysis bio-oil into valuable transportation biofuel. Propanoic acid (PAc) is one of the constituents of pyrolysis bio-oil, and served as a model compound for this investigation. Researches are currently focusing their attention in this area on developing novel catalytic approaches that will allow high activity and selectivity without significant deactivation of the catalyst. The specific aim of this work was therefore to investigate heterogeneous catalysis using group VIII noble metals for the HDO of PAc. The reaction mechanisms of different types of catalysts are discussed in detail. We examined the reaction in a conventionally continuous plug-flow reactor operated between 200-400ºC under atmospheric pressure. The different deoxygenation routes were discussed including decarbonylation (DCN), decarboxylation (DCX) and hydrogenation. The activity and selectivity as a function of reaction temperature with noble metals including: Pd, Pt, Rh, Ru, and Ni supported over SiO_2 was studied. The results showed that Pd was the most active catalyst, as the TOF followed the order: Pd > Ru > Pt > Rh > Ni. Pd, Pt and Rh catalysts proceed mainly through DCN/DCX reaction pathways. For Ru and Ni catalysts, while decarbonylation and decarboxylation pathways were predominant at lower temperatures (e.g., 200-250ºC), at higher temperatures (>300 ºC) diethyl ketone was formed. A support effect (i.e. high acidity) played an important role

when the reaction was carried out over SiO_2 and Ru and Ni (>300ºC), since ketonization of PAc was observed. The kinetics of Pd over different supports (carbon, SiO_2 and TiO_2) were examined. The activity based on the TOF decreases in the following order: Pd/SiO_2 > Pd/TiO_2 > Pd/C. For the Pd based catalysts a reaction rate order in PAc and H2 were found to be approximately 0.5 and 0, respectively, regardless of the support. The apparent activation energies studied in a temperature range of 200-240 ºC, were 16.7 ± 0.6, 19.3 ± 1.6 and 11.7 ± 0.7 kcal/mole for Pd/C, Pd/TiO_2 and Pd/SiO_2 catalysts, respectively.

In addition to studying group VIII noble metals over SiO_2, their activity and selectivity were examined over carbon supports. Similarly, the metal under study included: Pd, Pt, Rh, Ru, Ir, Ni, Ag, Au and Cu. The catalysts were screened at the same conditions described previously. The carbon supported catalysts exhibited mainly DCN and DCX to produce C1 and C2 hydrocarbons. As expected no ketonization products were observed, attributed to the support inactivity. In this case, Rh/C exhibited the highest activity and involved mainly DCN reaction pathway. The catalytic activity at 200ºC in terms of TOF decreased in the sequence Rh≥ Pt > Ir > Pd~Ru ~Ni, with no activity found for Au, Ag, and Cu. Interestingly, the same reaction rate order with respect to PAc and H_2, was found for the M/carbon catalysts (except for Ni/C). The latter exhibited a reaction rate order of 0.2 and -0.2 with respect to PAc and H_2, respectively.

Additionally, investigation of particle size effects in the HDO of PAc on Pd/SiO_2 was conducted. Strong electrostatic adsorption (SEA) was used to prepare catalysts with Pd nanoparticles ranging between 1.9 to 12.4 nm. Characterization techniques such as chemisorption, XRD and STEM were used in order to corroborate the particle size of each catalyst. The reaction proceeded mainly via DCN and hydrogenation to produce ethane

(C_2H_6) and propionaldehyde (EtCHO). It is concluded that the reaction is largely structure-insensitive, since the TOF remained underwent only modest changes. The product distribution increased toward EtCHO as the particle size increased, indicating hydrogenation is favored on single crystal Pd(111) and Pd(100) planes versus corners and edges. For decarbonylation to produce C_2H_6, reaction rate orders with respect to PAc (~0.5) and H2 (~0) were observed. In contrast, the reaction rate order with respect to PAc (~1.0) and H2 (~0.3) was different for hydrogenation to produce EtCHO. These differences had implications regarding the rate-controlling steps for the HDO of PAc.

Moreover, studies to elucidate the reaction mechanism and determine the rate-controlling step were conducted. The HDO of labeled propanoic acid-2,2-D2 catalyzed by 5wt% Pd/C was reported. The experiments were carried out to determine if the dehydrogenation of the α-C-H is in fact involved in the rate-controlling step. A normal kinetic isotope effect (KIE) was observed between the labeled and unlabeled PAc at 200ºC, 1 atm with concentrations of 1.2% PAc/5% H_2/balance He. A detailed evaluation of experimental results in comparison with theoretical (DFT) models is given. A KIE of kH/kD = 1.62 was observed and compared with computational DFT calculations were a kH/kD = 1.49 was obtained, consistent with the experimental results. Thus, the rate-controlling is largely dependent on the extent of dehydrogenation of the α-C-H. Overall, these research efforts have been undertaken in order to strengthen the understanding of the key factors that lead to the improvement of catalyst for the HDO of biomass-derived molecules, which has implications in the development of commercial catalytic processes.

7.2 PROPOSED FUTURE WORK

Future investigation for the HDO of fatty acids (upgrading of pyrolysis bio-oil) embrace significant challenges such as the creation of a robust catalyst. Understanding of the relationship between the physical properties of catalysts and their activity is crucial for the development of new/improved compositions. A catalyst that withstands coking, poisoning, high concentration of acids and water and can be readily regenerated without losing significant activity is highly desired. Moreover, a detailed understanding of the reaction mechanism is vital for the design and development of a suitable catalyst that can operate in harsh reaction conditions and that can be upscale for commercial purposes. Operating at steady-state in the presence of high partial pressures of hydrogen is not cost-effective, thus the reaction should give significant activity and selectivity at low partial pressures of hydrogen (or preferably in the absence of hydrogen). Hence, the questions that we should be asking is, why the reaction proceed in a certain manner? And, how can we modify the catalyst to obtain the desired results? To study the kinetics of deoxygenation of this fatty acids remains a challenge. However, conducting experiments similar to ours, in a fixed bed reactor is highly recommended, since it allows the researcher to perform experiments to investigate the effect of temperature, pressure, contact time and concentration of reactant in a straightforward manner.

Similar HDO studies conducted over short chain fatty acids is highly suggested. Acetic acid HDO reactions should be addressed and compare with our previous studies. Along these lines, future work should consider the study of novel and complex bimetallic catalysts. Including advanced preparation of bimetallic catalysts and atomic level characterization such as PdRe and PtRu bimetallic. Different metal oxide supports should

be considered such as TiO_2, ZrO_2 and Al_2O_3. Moreover, solid acid catalysts such as zeolites attracts a great degree of academic interest in the area of deoxygenation of fatty acids, since they have shown good stability and activity [1]. Moreover, studies of kinetics and mechanism to derive reactions network should be performed using characterization techniques such as Fourier transform infrared (FTIR) spectroscopy and XAFS. Lastly, isotopic labeling experiments to elucidate the reaction mechanism for the HDO of fatty acids is recommended. Once, a suitable catalysts is obtained, the catalytic HDO of fatty acids experiments with actual biomass should be conducted.

REFERENCES

1. S. National Academy of, E. National Academy of, M. Institute of and P. National Academies, *What you need to know about energy*, National Academies Press, Washington, D.C., 2008.
2. D. A. Simonetti and J. A. Dumesic, *Cataly Rev*, 2009, **51**, 441-484.
3. D. Kubicka, I. Kubicková and J. Čejka, *Catalysis Reviews*, 2013, **55**, 1-78.
4. D. C. Department Of Energy Washington, Defense Technical Information Center, Ft. Belvoir, 2002.
5. G. W. Huber, S. Iborra and A. Corma, *Chemical Reviews*, 2006, **106**, 4044-4098.
6. D. L. Klass, Elsevier.
7. E. Furimsky, *Applied Catalysis A: General*, 2000, **199**, 147-190.
8. E. Furimsky, *Catalysis Reviews*, 1983, **25**, 421-458.
9. M. Snare, P. Maki-Arvela, I. L. Simakova, J. Myllyoja and D. Y. Murzin, *Russ J Phys Chem B+*, 2009, **3**, 1035-1043.
10. I. Kubicková, M. Snåre, K. Eränen, P. Mäki-Arvela and D. Y. Murzin, *Catalysis Today*, 2005, **106**, 197-200.
11. P. Mäki-Arvela, M. Snåre, K. Eränen, J. Myllyoja and D. Y. Murzin, *Fuel*, 2008, **87**, 3543-3549.
12. M. Snåre, I. Kubicková, P. Mäki-Arvela, D. Chichova, K. Eränen and D. Y. Murzin, *Fuel*, 2008, **87**, 933-945.

13. W. F. Maier, W. Roth, I. Thies and P. V. Schleyer, *Chem Ber-Recl*, 1982, **115**, 808-812.

14. S. Lestari, P. i. Mäki-Arvela, H. Bernas, O. Simakova, R. Sjöholm, J. Beltramini, G. Q. M. Lu, J. Myllyoja, I. Simakova and D. Y. Murzin, *Energy & Fuels*, 2009, **23**, 3842-3845.

15. I. Simakova, O. Simakova, P. Maki-Arvela, A. Simakov, M. Estrada and D. Y. Murzin, *Appl Catal a-Gen*, 2009, **355**, 100-108.

16. P. Mäki-Arvela, J. Kuusisto, E. M. Sevilla, I. Simakova, J. P. Mikkola, J. Myllyoja, T. Salmi and D. Y. Murzin, *Applied Catalysis A: General*, 2008, **345**, 201-212.

17. D. Y. Murzin, B. Rozmyslowicz, P. Maki-Arvela, S. Lestari, O. A. Simakova, K. Eranen, I. L. Simakova and T. O. Salmi, *Top Catal*, 2010, **53**, 1274-1277.

18. G. W. Huber, J. N. Chheda, C. J. Barrett and J. A. Dumesic, *Science*, 2005, **308**, 1446-1450.

19. R. A. van Santen, in *Catalysis for Renewables*, Wiley-VCH Verlag GmbH & Co. KGaA, 2007, pp. 1-19.

20. A. Sivasamy, K. Y. Cheah, P. Fornasiero, F. Kemausuor, S. Zinoviev and S. Miertus, *ChemSusChem*, 2009, **2**, 278-300.

21. A. Corma, S. Iborra and A. Velty, *Chemical Reviews*, 2007, **107**, 2411-2502.

22. J. N. Chheda, G. W. Huber and J. A. Dumesic, *Angewandte Chemie International Edition*, 2007, **46**, 7164-7183.

23. T. V. Choudhary and C. B. Phillips, *Applied Catalysis A: General*, 2011, **397**, 1-12.

24. D. Vlachos, J. Chen, R. Gorte, G. Huber and M. Tsapatsis, *Catalysis Letters*, 2010, **140**, 77-84.

25. I. M. S. Richard Malcolm Brown, *Cellulose:molecular and structural biology : selected articles on the synthesis, structure, and applications of cellulose*, 2007.

26. S. Dumitriu, *Polysaccharides: Structural Diversity and Functional Versatility* CRC Press (2 edition), 2004.

27. E. Adler, *Wood Science and Technology*, 1977, **11**, 169-218.

28. F. Ma and M. A. Hanna, *Bioresource Technology*, 1999, **70**, 1-15.

29. J. Speight, *Chemistry and Technology of Petroleum*, Marcel Dekker, New York, 1991.

30. A. V. Bridgwater and D. G. B. Boocock, *Developments in thermochemical biomass conversion*, Blackie Academic & Professional, London; New York, 1997.

31. P. P. Nunes, D. Brodzki, G. Bugli and G. Djegamariadassou, *Rev I Fr Petrol*, 1986, **41**, 421-431.

32. Y. S. Prasad and N. N. Bakhshi, *Appl Catal*, 1985, **18**, 71-85.

33. E. Furimsky, *Applied Catalysis*, 1983, **6**, 159-164.

34. J. C. Serrano-Ruiz and J. A. Dumesic, *Energy & Environmental Science*, 2011, **4**, 83-99.

35. Q. Zhang, J. Chang, T. Wang and Y. Xu, *Energy Conversion and Management*, 2007, **48**, 87-92.

36. S. Patai, *The Chemistry of Carboxylic acids and esters*, New York, 1969.

37. S. Nishimura, *Handbook of heterogeneous catalytic hydrogenation for organic synthesis*, New York, 2001.

38. N. E. S. K. Peter C. Vollhardt, ed. Mcmillan, 2003, p. 1203.

39. R. D. Rieke, D. S. Thakur, B. D. Roberts and G. T. White, *J Am Oil Chem Soc*, 1997, **74**, 333-339.

40. E. Furimsky, *Fuel*, 1978, **57**, 494-496.

41. D. H. R. Barton and S. W. McCombie, *Journal of the Chemical Society, Perkin Transactions 1*, 1975, 1574-1585.

42. D. Y. Murzin, M. Snare, I. Kubickova, P. Maki-Arvela, K. Eranen and J. Warna, *Chem Eng J*, 2007, **134**, 29-34.

43. P. i. MÃ¤ki-Arvela, I. Kubickova, M. SnÃ¥re, K. ErÃ¤nen and D. Y. Murzin, *Energy & Fuels*, 2006, **21**, 30-41.

44. S. Lestari, P. Mäki-Arvela, I. Simakova, J. Beltramini, G. Lu and D. Murzin, *Catalysis Letters*, 2009, **130**, 48-51.

45. H. Bernas, K. Eränen, I. Simakova, A.-R. Leino, K. Kordás, J. Myllyoja, P. Mäki-Arvela, T. Salmi and D. Y. Murzin, *Fuel*, 2010, **89**, 2033-2039.

46. S. Lestari, I. Simakova, A. Tokarev, P. Mäki-Arvela, K. Eränen and D. Murzin, *Catalysis Letters*, 2008, **122**, 247-251.

47. E. W. Ping, J. Pierson, R. Wallace, J. T. Miller, T. F. Fuller and C. W. Jones, *Applied Catalysis A: General*, 2011, **396**, 85-90.

48. I. Simakova, O. Simakova, P. Mäki-Arvela, A. Simakov, M. Estrada and D. Y. Murzin, *Applied Catalysis A: General*, 2009, **355**, 100-108.

49. S. J. Tauster, S. C. Fung and R. L. Garten, *J Am Chem Soc*, 1978, **100**, 170-175.

50. T. C. Chang, J. J. Chen and C. T. Yeh, *Journal of Catalysis*, 1985, **96**, 51-57.

51. S. J. Tauster, *Accounts of Chemical Research*, 1987, **20**, 389-394.

52. J. G. Immer, M. J. Kelly and H. H. Lamb, *Applied Catalysis A: General*, 2010, **375**, 134-139.

53. N. S *Bulletin of the Catalysis Society of India*, 2003, **2**, 107-121.

54. A. T. Madsen, E. H. Ahmed, C. H. Christensen, R. Fehrmann and A. Riisager, *Fuel*, **In Press, Corrected Proof**.

55. L. Boda, G. Onyestyák, H. Solt, F. Lónyi, J. Valyon and A. Thernesz, *Applied Catalysis A: General*, 2010, **374**, 158-169.

56. P. Do, M. Chiappero, L. Lobban and D. Resasco, *Catalysis Letters*, 2009, **130**, 9-18.

57. R. G. Mallinson, T. T. Pham, L. L. Lobban and D. E. Resasco, *Journal of Catalysis*, 2009, **266**, 9-14.

58. D. E. Resasco, T. Danuthai, S. Jongpatiwut, T. Rirksomboon and S. Osuwan, *Appl Catal a-Gen*, 2009, **361**, 99-105.

59. D. E. Resasco, T. Sooknoi, T. Danuthai, L. L. Lobban and R. G. Mallinson, *Journal of Catalysis*, 2008, **258**, 199-209.

60. P. Mäki-Arvela, J. Hájek, T. Salmi and D. Y. Murzin, *Applied Catalysis A: General*, 2005, **292**, 1-49.

61. K. S. Kim and M. A. Barteau, *Journal of Catalysis*, 1990, **125**, 353-375.

62. M. A. Langell, C. L. Berrie, M. H. Nassir and K. W. Wulser, *Surf Sci*, 1994, **320**, 25-38.

63. X. D. Peng and M. A. Barteau, *Surf Sci*, 1990, **233**, 283-292.

64. T. Yokoyama and N. Yamagata, *Applied Catalysis A: General*, 2001, **221**, 227-239.

65. R. Pestman, R. M. Koster, J. A. Z. Pieterse and V. Ponec, *Journal of Catalysis*, 1997, **168**, 255-264.

66. R. Pestman, A. van Duijne, J. A. Z. Pieterse and V. Ponec, *Journal of Molecular Catalysis A: Chemical*, 1995, **103**, 175-180.

67. J. C. Kuriacose and S. S. Jewur, *Journal of Catalysis*, 1977, **50**, 330-341.

68. M. Jayamani and C. N. Pillai, *Journal of Catalysis*, 1984, **87**, 93-97.

69. C. A. Gaertner, J. C. Serrano-Ruiz, D. J. Braden and J. A. Dumesic, *Journal of Catalysis*, 2009, **266**, 71-78.

70. G. L. Haller and D. E. Resasco, in *Adv Catal*, eds. H. P. D.D. Eley and B. W. Paul, Academic Press, 1989, vol. Volume 36, pp. 173-235.

71. H. G. Manyar, C. Paun, R. Pilus, D. W. Rooney, J. M. Thompson and C. Hardacre, *Chemical Communications*, 2010, **46**, 6279-6281.

72. R. Pestman, R. M. Koster, J. A. Z. Pieterse and V. Ponec, *Journal of Catalysis*, 1997, **168**, 255-264.

73. H. Benaissa, P. N. Davey, Y. Z. Khimyak and I. V. Kozhevnikov, *Journal of Catalysis*, 2008, **253**, 244-252.

74. T. Okuhara, N. Mizuno and M. Misono, in *Advances in Catalysis*, eds. W. O. H. D.D. Eley and G. Bruce, Academic Press, 1996, vol. Volume 41, pp. 113-252.

75. I. Yuranov, L. Kiwi-Minsker, V. Barelko and A. Renken, *Reaction Kinetics and the Development of Catalytic Processes*, 1999, **122**, 191-198.

76. T. A. Nijhuis, M. T. Kreutzer, A. C. J. Romijn, F. Kapteijn and J. A. Moulijn, *Chemical Engineering Science*, 2001, **56**, 823-829.

77. R. L. Augustine, in *Heterogeneous catalysis for the synthetic chemist* ed. M. Dekker, New York 1996, pp. 153-178.

78. W. Rachmady and M. A. Vannice, *Journal of Catalysis*, 2000, **192**, 322-334.

79. T. A. Montzka, S. Swaminathan and R. A. Firestone, *The Journal of Physical Chemistry*, 1994, **98**, 13171-13176.

80. E. G. Palacios, G. Juárez-López and A. J. Monhemius, *Hydrometallurgy*, 2004, **72**, 139-148.

81. M. A. N. Santiago, M. A. Sánchez-Castillo, R. D. Cortright and J. A. Dumesic, *Journal of Catalysis*, 2000, **193**, 16-28.

82. M. Neurock and V. Pallassana, *Journal of Catalysis*, 2002, **209**, 289-305.

83. R. J. F. C. H. Bartholomew, *Fundamentals of Industrial Catalytic Processes*, 2nd edn., 2005.

84. C. Perego and P. Villa, *Catalysis Today*, 1997, **34**, 281-305.

85. T. E. Feltes, L. Espinosa-Alonso, E. d. Smit, L. D'Souza, R. J. Meyer, B. M. Weckhuysen and J. R. Regalbuto, *Journal of Catalysis*, 2010, **270**, 95-102.

86. R. John, in *Catalyst Preparation*, CRC Press, 2006, pp. 297-318.

87. J. R. Regalbuto, *Catalyst Preparation: Science and Engineering*, 2006, 297-318.

88. S. Lambert, N. Job, L. D'Souza, M. F. R. Pereira, R. Pirard, B. Heinrichs, J. L. Figueiredo, J.-P. Pirard and J. R. Regalbuto, *Journal of Catalysis*, 2009, **261**, 23-33.

89. L. Jiao and J. R. Regalbuto, *Journal of Catalysis*, 2008, **260**, 329-341.

90. J. T. Miller, M. Schreier, A. J. Kropf and J. R. Regalbuto, *Journal of Catalysis*, 2004, **225**, 203-212.

91. C. O. Paul A. Webb, in *Analytical Methods in fine particle technology* Micromeritics Instruments Corp, Georgia, USA, First edn., 1997.

92. M. Fadoni and L. Lucarelli, in *Studies in Surface Science and Catalysis*, ed. A. Dąbrowski, Elsevier, 1999, vol. Volume 120, Part A, pp. 177-225.

93. W. C. Conner and J. L. Falconer, *Chem Rev*, 1995, **95**, 759-788.

94. A. C. Menzies, *Analytical Chemistry*, 1960, **32**, 898-904.

95. A. T. e. P. Anatoliĭ Ivanovich Samchuk, in *Analytical chemistry of minerals*, VNU Science Press BV, 1987, p. 168.

96. B. ASSOC, *Annual Energy Review 2010*, 1949-2010, 384.

97. D. G. Lima, V. C. D. Soares, E. B. Ribeiro, D. A. Carvalho, É. C. V. Cardoso, F. C. Rassi, K. C. Mundim, J. C. Rubim and P. A. Z. Suarez, *Journal of Analytical and Applied Pyrolysis*, 2004, **71**, 987-996.

98. A. V. Bridgwater, *Chemical Engineering Journal*, 2003, **91**, 87-102.

99. J. Michael Robinson, C. E. Burgess, M. A. Bently, C. D. Brasher, B. O. Horne, D. M. Lillard, J. M. Macias, H. D. Mandal, S. C. Mills, K. D. O'Hara, J. T. Pon, A. F.

Raigoza, E. H. Sanchez and J. S. Villarreal, *Biomass and Bioenergy*, 2004, **26**, 473-483.

100. A. Rabl, A. Benoist, D. Dron, B. Peuportier, J. Spadaro and A. Zoughaib, *The International Journal of Life Cycle Assessment*, 2007, **12**, 281-281.

101. A. V. Bridgwater, D. Meier and D. Radlein, *Organic Geochemistry*, 1999, **30**, 1479-1493.

102. J. C. Serrano-Ruiz, A. Pineda, A. M. Balu, R. Luque, J. M. Campelo, A. A. Romero and J. M. Ramos-Fernández, *Catalysis Today*, 2012, **195**, 162-168.

103. B. J. O'Neill, E. I. Gürbüz and J. A. Dumesic, *Journal of Catalysis*.

104. C. A. Henao, D. Braden, C. T. Maravelias and J. A. Dumesic, in *Computer Aided Chemical Engineering*, eds. M. C. G. E.N. Pistikopoulos and A. C. Kokossis, Elsevier, 2011, vol. Volume 29, pp. 1723-1727.

105. R. M. West, E. L. Kunkes, D. A. Simonetti and J. A. Dumesic, *Catalysis Today*, 2009, **147**, 115-125.

106. J. Q. Bond, D. Wang, D. M. Alonso and J. A. Dumesic, *Journal of Catalysis*, 2011, **281**, 290-299.

107. S. G. Wettstein, J. Q. Bond, D. M. Alonso, H. N. Pham, A. K. Datye and J. A. Dumesic, *Applied Catalysis B: Environmental*, 2012, **117–118**, 321-329.

108. J. N. Chheda and J. A. Dumesic, *Catalysis Today*, 2007, **123**, 59-70.

109. M. Chia and J. A. Dumesic, *Chemical Communications*, 2011, **47**, 12233-12235.

110. M. Chiappero, P. T. M. Do, S. Crossley, L. L. Lobban and D. E. Resasco, *Fuel*, 2011, **90**, 1155-1165.

111. M. A. Alotaibi, E. F. Kozhevnikova and I. V. Kozhevnikov, *Applied Catalysis A: General*, 2012, **447–448**, 32-40.

112. R. Pestman, R. M. Koster, A. vanDuijne, J. A. Z. Pieterse and V. Ponec, *Journal of Catalysis*, 1997, **168**, 265-272.

113. R. Pestman, A. Vanduijne, J. A. Z. Pieterse and V. Ponec, *J Mol Catal a-Chem*, 1995, **103**, 175-180.

114. M. Renz, *Eur J Org Chem*, 2005, 979-988.

115. J. P. Ford, J. G. Immer and H. H. Lamb, *Top Catal*, 2012, **55**, 175-184.

116. A. T. Madsen, E. H. Ahmed, C. H. Christensen, R. Fehrmann and A. Riisager, *Fuel*, 2011, **90**, 3433-3438.

117. W. F. Maier, W. Roth, I. Thies and P. V. R. Schleyer, *Chemische Berichte*, 1982, **115**, 808-812.

118. P. Mäki-Arvela, M. Snåre, K. Eränen, J. Myllyoja and D. Y. Murzin, *Fuel*, 2008, **87**, 3543-3549.

119. R. Van Hardeveld and F. Hartog, *Surface Science*, 1969, **15**, 189-230.

120. G. C. Bond, *Surface Science*, 1985, **156, Part 2**, 966-981.

121. J. Lu, S. Behtash and A. Heyden, *The Journal of Physical Chemistry C*, 2012, **116**, 14328-14341.

122. G. W. Roberts, *Chemical reactions and chemical reactors*, John Wiley & Sons, Hoboken, NJ, 2008.

123. D. A. Bulushev and J. R. H. Ross, *Catalysis Today*, 2011, **163**, 42-46.

124. P. G. Smirniotis, *Angewandte Chemie International Edition*, 2007, **46**, 1007-1007.

125. P. B. Weisz and C. D. Prater, in *Adv Catal*, eds. V. I. K. W.G. Frankenburg and E. K. Rideal, Academic Press, 1954, vol. Volume 6, pp. 143-196.

126. M. E. Davis and R. J. Davis, *Fundamentals of chemical reaction engineering*, 1st ed. edn., McGraw-Hill, Dubuque, Iowa, 2002.

127. J. A. Lopez-Ruiz and R. J. Davis, *Green Chemistry*, 2013.

128. T. N. Pham, D. Shi and D. E. Resasco, *Applied Catalysis B: Environmental*, 2014, **145**, 10-23.

129. B. J. O'Neill, E. I. Gürbüz and J. A. Dumesic, *Journal of Catalysis*, 2012, **290**, 193-201.

130. K. Jacobson, K. C. Maheria and A. Kumar Dalai, *Renewable and Sustainable Energy Reviews*, 2013, **23**, 91-106.

131. M. Mohammad, T. Kandaramath Hari, Z. Yaakob, Y. Chandra Sharma and K. Sopian, *Renewable and Sustainable Energy Reviews*, 2013, **22**, 121-132.

132. E. Furimsky, *Catalysis Today*, 2013, **217**, 13-56.

133. M. Snåre, I. Kubičková, P. Mäki-Arvela, K. Eränen and D. Y. Murzin, *Industrial & Engineering Chemistry Research*, 2006, **45**, 5708-5715.

134. C. R. Henry, C. Chapon, S. Giorgio and C. Goyhenex, in *Chemisorption and Reactivity on Supported Clusters and Thin Films*, eds. R. Lambert and G. Pacchioni, Springer Netherlands, 1997, vol. 331, pp. 117-152.

135. P. E. Strizhak, *Theor Exp Chem*, 2013, **49**, 2-21.

136. C. P. Vinod, *Catalysis Today*, 2010, **154**, 113-117.

137. B. R. Cuenya, *Thin Solid Films*, 2010, **518**, 3127-3150.

138. F. Zaera, *Prog Surf Sci*, 2001, **69**, 1-98.

139. J. M. Martínez de la Hoz and P. B. Balbuena, *The Journal of Physical Chemistry C*, 2011, **115**, 21324-21333.

140. M. Boudart, *Chemical Reviews*, 1995, **95**, 661-666.

141. S. Lambert, C. Cellier, P. Grange, J.-P. Pirard and B. t. Heinrichs, *Journal of Catalysis*, 2004, **221**, 335-346.

142. J. B. Butt and C. L. M. Joyal, *Journal of the Chemical Society, Faraday Transactions*, 1990, **86**, 2911-2917.

143. N. Marín-Astorga, G. Pecchi, J. L. G. Fierro and P. Reyes, *Catalysis Letters*, 2003, **91**, 115-121.

144. A. Borodziński, *Catalysis Letters*, 2001, **71**, 169-175.

145. A. Binder, M. Seipenbusch, M. Muhler and G. Kasper, *Journal of Catalysis*, 2009, **268**, 150-155.

146. Y. K. Lugo-José, J. R. Monnier and C. T. Williams, *Applied Catalysis A: General*, 2014, **469**, 410-418.

147. O.-L. Pérez, D. Romeu and M. J. Yacamán, *Journal of Catalysis*, 1983, **79**, 240-241.

148. N. D. Spencer, R. C. Schoonmaker and G. A. Somorjai, *Nature*, 1981, **294**, 643-644.

149. A. V. Zeigarnik, R. E. Valdés-Pérez and O. N. Myatkovskaya, *The Journal of Physical Chemistry B*, 2000, **104**, 10578-10587.

150. J. Lu, S. Behtash, M. Faheem and A. Heyden, *Journal of Catalysis*, 2013, **305**, 56-66.

151. H. Zhong and W. Xianqin, in *Novel Materials for Catalysis and Fuels Processing*, American Chemical Society, 2013, vol. 1132, pp. 301-329.

152. D. Carpenter, T. L. Westover, S. Czernik and W. Jablonski, *Green Chemistry*, 2014, **16**, 384-406.

153. P. i. Mäki-Arvela, B. Rozmysłowicz, S. Lestari, O. Simakova, K. Eränen, T. Salmi and D. Y. Murzin, *Energy & Fuels*, 2011, **25**, 2815-2825.

154. E. W. Ping, R. Wallace, J. Pierson, T. F. Fuller and C. W. Jones, *Microporous and Mesoporous Materials*, 2010, **132**, 174-180.

155. R. W. Carr, in *Comprehensive Chemical Kinetics*, ed. W. C. Robert, Elsevier, 2007, vol. Volume 42, pp. 43-99.

156. G. B. Marin and G. S. Yablonsky, *Kinetics of chemical reactions : decoding complexity*, Wiley-VCH, Weinheim, Germany, 2011.

157. S. Behtash, J. Lu, M. Faheem and A. Heyden, *Green Chemistry*, 2014, **16**, 605-616.

158. J. M. Lu, S. Behtash, M. Faheem and A. Heyden, *Journal of Catalysis*, 2013, **305**, 56-66.

159. J. M. Lu, S. Behtash and A. Heyden, *Journal of Physical Chemistry C*, 2012, **116**, 14328-14341.

160. Y. K. Lugo-Jose, J. R. Monnier and C. T. Williams, *Applied Catalysis a-General*, 2014, **469**, 410-418.

161. V. Pallassana and M. Neurock, *Journal of Catalysis*, 2002, **209**, 289-305.

162. H. Olcay, L. J. Xu, Y. Xu and G. W. Huber, *Chemcatchem*, 2010, **2**, 1420-1424.

163. J. L. Davis and M. A. Barteau, *Surface Science*, 1991, **256**, 50-66.

164. J. L. Davis and M. A. Barteau, *Langmuir*, 1989, **5**, 1299-1309.

165. K. Tamaru, in *Catalysis*, eds. J. R. Anderson and M. Boudart, Springer Berlin Heidelberg, 1991, vol. 9, pp. 87-129.

166. M. Neurock, *AIChE Journal*, 1994, **40**, 1085-1087.

167. J. Happel, *Isotopic assessment of heterogeneous catalysis*, Academic Press, 1986.

168. J. Sommer and S. Walspurger, *ChemInform*, 2007, **38**, 1-29.

169. G. C. Bond, J. J. Philipson, P. B. Wells and J. M. Winterbottom, *Transactions of the Faraday Society*, 1966, **62**, 443-454.

170. H. Eyring and M. Polanyi, *Zeitschrift Fur Physikalische Chemie-Abteilung B-Chemie Der Elementarprozesse Aufbau Der Materie*, 1931, **12**, 279-311.

171. J. Bigeleisen and M. G. Mayer, *The Journal of Chemical Physics*, 1947, **15**, 261-267.

172. F. J. Winkler, *Angewandte Chemie*, 1981, **93**, 220-220.

173. C. Stegelmann, A. Andreasen and C. T. Campbell, *Journal of the American Chemical Society*, 2009, **131**, 13563-13563.

174. D. G. Truhlar, B. C. Garrett and S. J. Klippenstein, *Journal of Physical Chemistry*, 1996, **100**, 12771-12800.

175. D. G. Truhlar, W. L. Hase and J. T. Hynes, *Journal of Physical Chemistry*, 1983, **87**, 2664-2682.

176. H. Eyring, *Journal of Chemical Physics*, 1935, **3**, 107-115.

177. R. A. Tomasi, *A Spectrum of Spectral Problems: Supplement*, Sunbelt R & T, Incorporated, 1994.

178. Y. Amenomiya and R. F. Pottie, *Canadian Journal of Chemistry*, 1968, **46**, 1735-1739.

179. Y. Amenomiya and R. F. Pottie, *Canadian Journal of Chemistry*, 1968, **46**, 1741-1746.

180. M. Stöcker, *Angewandte Chemie International Edition*, 2008, **47**, 9200-9211.

181. C. Bessou, F. Ferchaud, B. Gabrielle and B. Mary, *Agronomy for Sustainable Development (EDP Sciences)*, 2011, **31**, 1-79.

182. D. Lee, S. I. Cho, G. J. Kim, H. Kim and I. M. Lee, *Journal of Industrial and Engineering Chemistry*, 2007, **13**, 1067-1075.

183. J. Fu, X. Lu and P. E. Savage, *Energy & Environmental Science*, 2010, **3**, 311-317.

184. N. Joshi and A. Lawal, *Chemical Engineering Science*, 2012, **84**, 761-771.

185. L. Chen, Y. Zhu, H. Zheng, C. Zhang and Y. Li, *Applied Catalysis A: General*, 2012, **411–412**, 95-104.

186. R. R. Davda, J. W. Shabaker, G. W. Huber, R. D. Cortright and J. A. Dumesic, *Appl. Catal. B-Environ.*, 2003, **43**, 13-26.

187. H. Olcay, L. Xu, Y. Xu and G. W. Huber, *ChemCatChem*, 2010, **2**, 1420-1424.

188. J. D. Hoeschele, J. E. Turner and M. W. England, *Science of The Total Environment*, 1991, **109–110**, 477-492.

189. C.-L. Lee, C.-M. Tseng, R.-B. Wu and S.-C. Syu, *Journal of The Electrochemical Society*, 2009, **156**, D348-D350.

190. E. Steinhauser, *Circuit World*, 2010, **36**, 4-8.

191. A. A. Kiss, A. C. Dimian and G. Rothenberg, *Advanced Synthesis & Catalysis*, 2006, **348**, 75-81.

192. M. Ibrahim, A. Nada and D. E. Kamal, *Indian J Pure Ap Phy*, 2005, **43**, 911-917.

193. C. D. Wagner and G. E. Muilenberg, *Handbook of x-ray photoelectron spectroscopy: a reference book of standard data for use in x-ray photoelectron spectroscopy*, Perkin-Elmer Corp., Physical Electronics Division, 1979.

194. H. Kumar, S. Ghosh, D. K. Avasthi, D. Kabiraj, N. P. Lalla, T. Shripathi and J. C. Pivin, *Vacuum*, 2010, **85**, 139-144.

195. J.-R. Song, L.-X. Wen, Z.-M. Xia and J.-F. Chen, *Fuel Process Technol*, 2007, **88**, 443-449.

196. D. Liu, Y. M. López-De Jesús, J. R. Monnier and C. T. Williams, *Journal of Catalysis*, 2010, **269**, 376-387.

197. T. Shaochun, V. Sascha, Z. Zhou, R. Hua and M. Xiangkang, *Nanotechnology*, 2012, **23**, 255606.

198. X.-F. Yang, A. Wang, B. Qiao, J. Li, J. Liu and T. Zhang, *Accounts of Chemical Research*, 2013, **46**, 1740-1748.

199. K. Punyawudho, D. A. Blom, J. W. Van Zee and J. R. Monnier, *Electrochimica Acta*, 2010, **55**, 5349-5356.

200. G. Bergeret and P. Gallezot, in *Handbook of Heterogeneous Catalysis*, Wiley-VCH Verlag GmbH & Co. KGaA, 2008.

201. G. Kresse and J. Hafner, *Physical Review B*, 1993, **48**, 13115-13118.

202. G. Kresse and J. Hafner, in *Physical Review B*, 1993, vol. 47, pp. 558-561.

203. G. Kresse and J. Furthmuller, *Computational Materials Science*, 1996, **6**, 15-50.

204. G. Kresse and D. Joubert, *Physical Review B*, 1999, **59**, 1758-1775.

205. J. P. Perdew and W. Yue, *Physical Review B*, 1986, **33**, 8800-8802.

206. J. P. Perdew and Y. Wang, *Physical Review B*, 1992, **45**, 13244-13249.

207. F. Jensen, *Introduction to computational chemistry*, Wiley, 1999.

208. G. Buzzi-Ferraris, *"BzzMath: Numerical libraries in C++", Politecnico di Milano: WWW.CHEM.POLIMI.IT/HOMES/GBUZZI*.

209. R. Alcalá, J. Greeley, M. Mavrikakis, J.A. Dumesic, J. A. *The Journal of Chemical Physics* **2002,** *116* (20), 8973-8980.

APPENDIX A: SUPPLEMENTARY INFORMATION FOR CHAPTER 2

FROM SECTION 2.3.5

The spectra for Pd/SiO_2 and SiO_2 were collected every 5 minutes up to 100 and 105 min respectively. Figure A.1 and A.2 depicts the PAc adsorption spectra for collected every 30 min. Propanoic acid is characterized by the –COOH (carboxylic acid group). This group exhibits a sharp C=O band and a broad O-H stretching band between 1800-1630 cm^{-1} and 3650-2500 cm^{-1}, respectively. For Pd/SiO_2, the main spectral characteristics of propanoic acid are a broad band at 1734 cm^{-1}corresponding to C=O symmetric stretching and at 1500 cm^{-1} corresponding to C-H vibration. For the adsorbed acid on the SiO_2 support, a prominent C=O stretch is located between 1750-1680 cm^{-1}. The position could be assigned to the dimeric and monomeric acid species [164]. The peaks at 1559 and 1466 cm^{-1} are assigned to ν_{as}(OCO) and ν_s(OCO) of the carboxylate group, respectively. The prominent absorption bands on SiO_2 could provide insight about the carboxylate intermediates that are crucial for the ketone formation. Ibrahim et al. published an FTIR spectroscopic study on carboxylic acid and observed a C=O stretching band of propanoic acid at 1740.1 cm^{-1} [192].

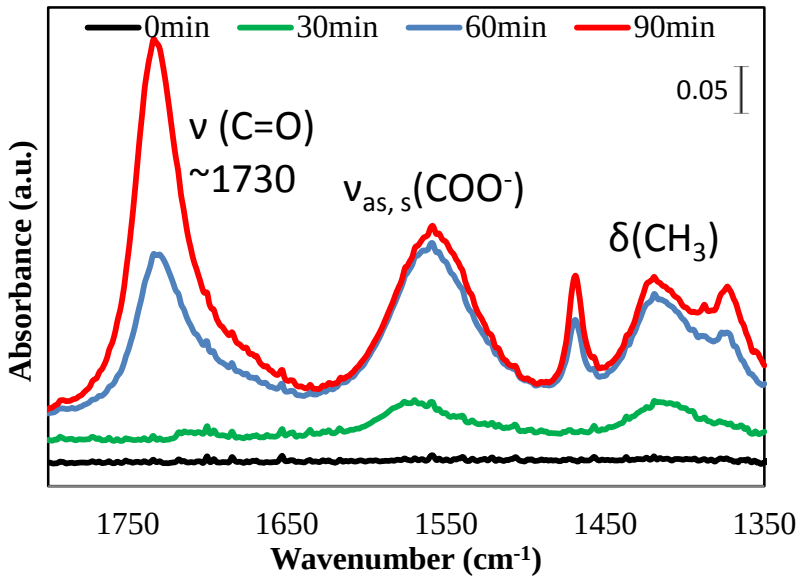

Figure A.1: FTIR adsorption for 1.86wt% Pd/SiO_2, 0.10% PAc, 20% Hydrogen, balance Helium Total flow rate = 50 sccm.

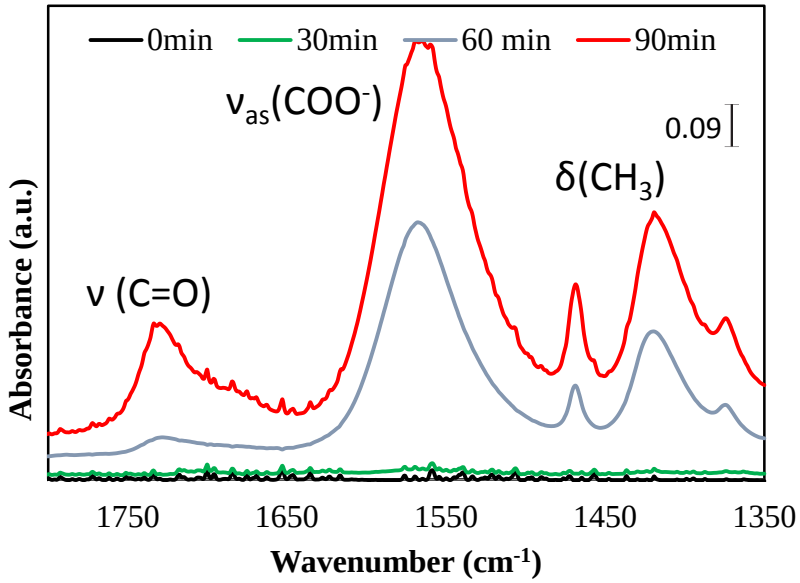

Figure A.2: FTIR adsorption for SiO2, 0.10% PAc, 20% Hydrogen, balance Helium Total flow rate = 50 sccm.

FROM SECTION 2.4.1

Gas chromatography calibration curves of feed and products analyzed. Flame ionization detector (FID) and Thermal conductivity detector (TCD).

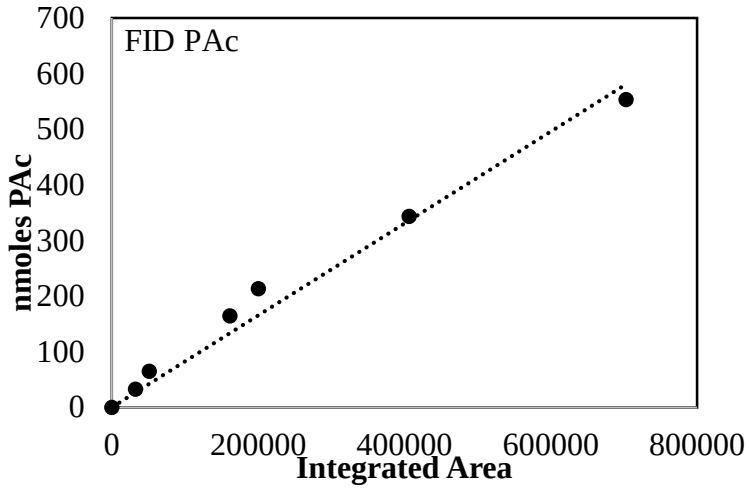

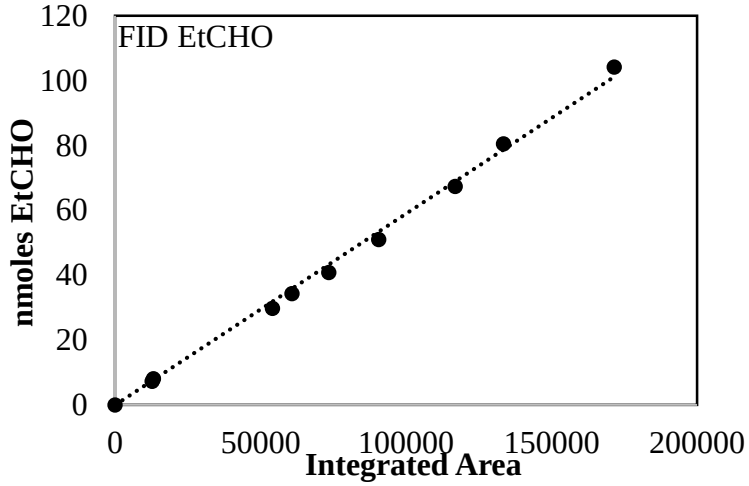

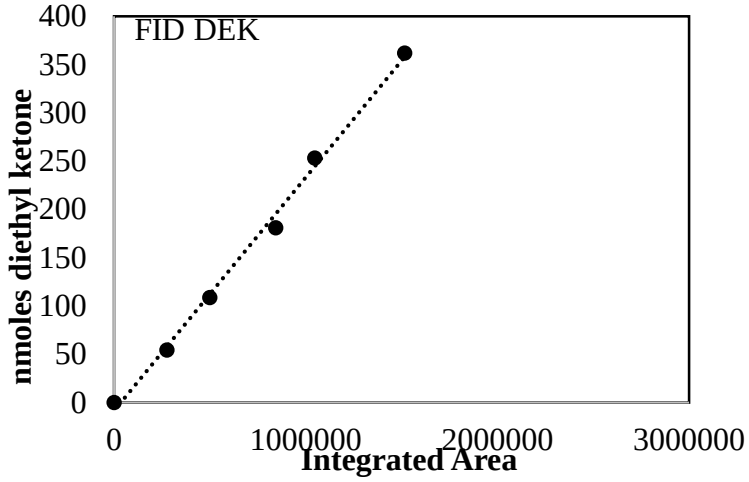

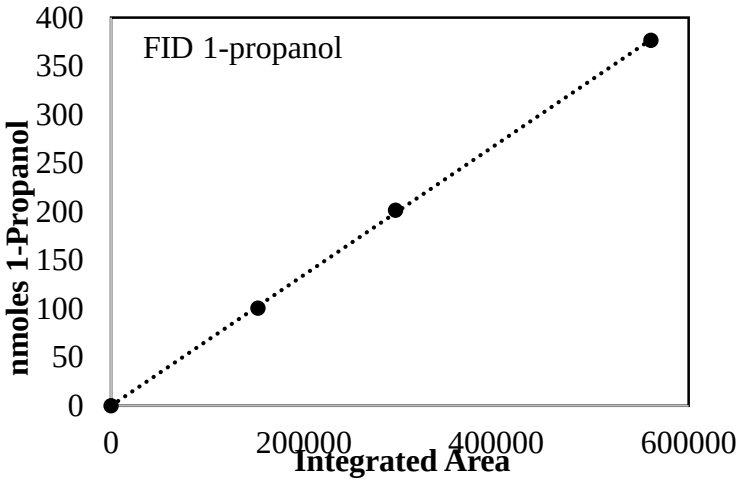
FID 1-propanol
nmoles 1-Propanol
400
350
300
250
200
150
100
50
0
0
200000
400000
600000
Integrated Area

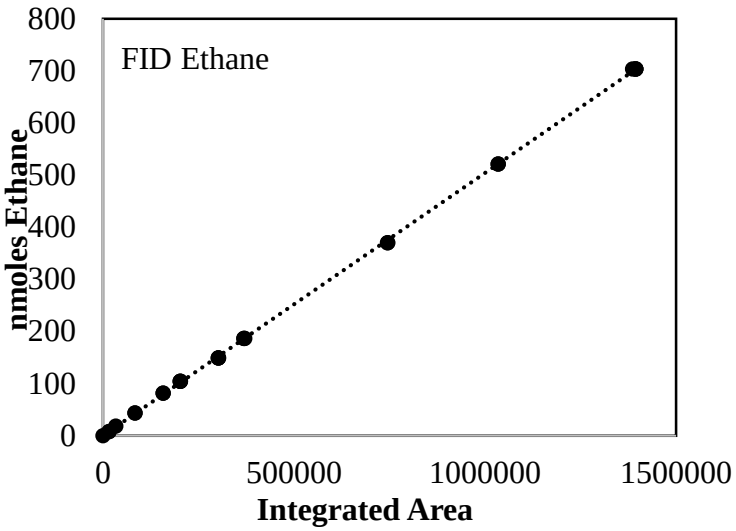
FID Ethane
nmoles Ethane
800
700
600
500
400
300
200
100
0
0
500000
1000000
1500000
Integrated Area

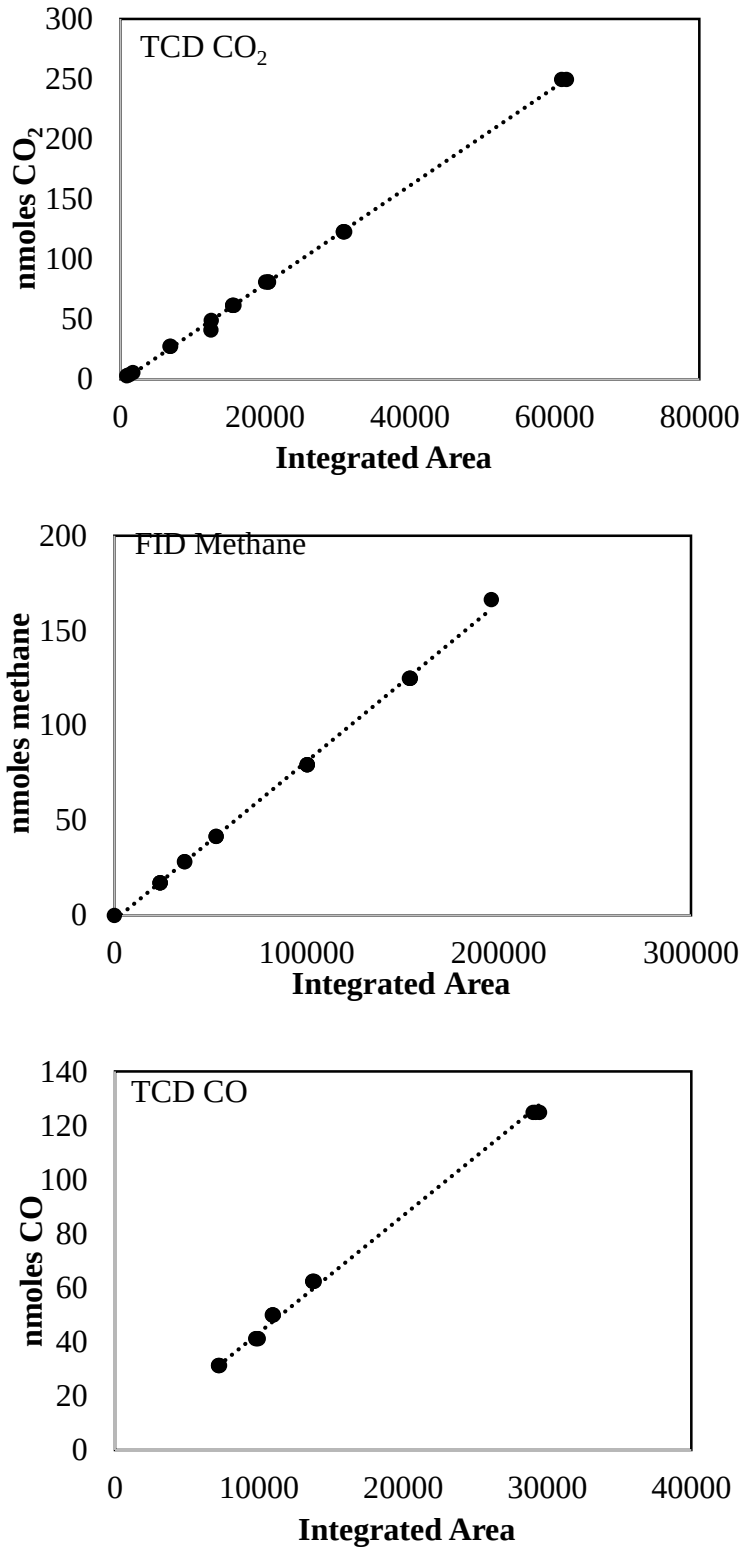

Figure A.3: Calibration curves for PAc, EtCHO, 1-propanol, DEK, ethane, methane, CO2 and CO.

Table A.1: Calibration parameters (retention time and response factor) based on the FID and TCD columns.

Compound	R.T (min)	R.F HP-PlotQ (L=30(m) ID=0.320(mm))
Methane	1.91	8.82E-04
Ethylene	2.58	6.26E-04
ethane	2.91	5.04E-04
propylene	5.39	3.79E-04
propane	5.69	3.63E-04
1-butene	8.61	2.81E-04
n-butane	8.97	2.84E-04
EtCHO	10.46	5.90E-04
1-propanol	11.86	3.96E-04
DEK	15.76	1.67E-04
Propanoic acid	17.53	8.22E-04
CO	1.87	1.82E-03
CO_2	2.19	1.70E-03

APPENDIX B: SUPPLEMENTARY INFORMATION FOR CHAPTER 3

B.1 XPS STUDIES ON NI/SIO$_2$

In order to determine the oxidation state of the Ni metal, X-ray photoelectron spectroscopy (XPS) measurements for were conducted utilizing a Kratos AXIS Ultra DLD XPS system equipped with a monochromatic Al Kα source. The energy scale of the system is calibrated using an Au foil with Au4f scanned for the Al radiation and a Cu foil with Cu2p scanned for Mg radiation resulting in a difference of 1081.70 ± 0.025 eV between these two peaks. The binding energy is calibrated using an Ag foil with Ag3d$_{5/2}$ set at 368.21 ± 0.025 eV for the monochromatic Al X-ray source. The monochromatic Al Kα source was operated at 15 keV and 120 W. The pass energy was fixed at 40 eV for the detailed scans. A charge neutralizer (CN) was used to compensate for the surface charge. The analyses were performed on the catalyst as received (room temperature) and *in-situ* reduction up to 400 ºC. The biding energies (eV) of the Si 2P curve were referenced to SiO_2 at 103.3 eV. Figure B.1 shows the Ni 2p XPS spectra obtained at room temperature for the as prepared catalyst and the catalyst after pre-treatment under 100% H_2 (400 ºC, 2 hours). The of Ni2p3/2 biding energies for the as prepared Ni/SiO_2 are 856.6 eV and 861.0 eV, indicating a peak distinctive of nickel oxide Ni_2O_3/SiO_2 and Ni^{2+} $2p_{3/2}$ [193-195]. Upon reduction up to 400ºC, the biding energy is 852.0 eV suggesting that Ni is mainly metallic Ni^0, with no evidence of the satellite peak.

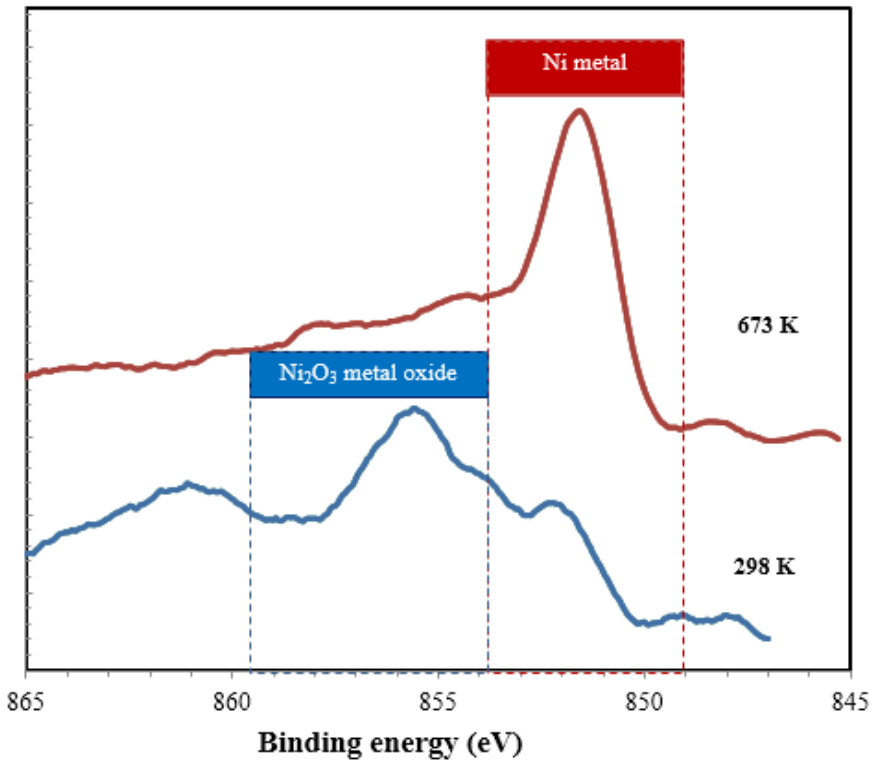

Figure B.1: Ni/SiO_2 2p XPS spectra as received and pre-treated, 100% H_2 for 2 hours up to 400 ºC.

B.2 TEMPERATURE PROGRAMMED OXIDATION/REDUCTION (TPO/TPR)

Temperature programmed oxidation and reduction experiments were performed on supported Ru, and Ni catalysts. The experiments were carried out using a flow system coupled to an Inficon Transpector 2 (model: TSPTT300) mass spectrometer pumped by a Pfeiffer (model: MVP 015-2) vacuum pump. The catalyst in the oxidized form is first reduced *in-situ* with pure hydrogen (5 K/min), and then cooled to room temperature under inert argon flow. The total flows of the reactive gases were 50 sccm. The catalyst was then exposed to 1% O_2/He in a temperature rise program and the signal output of O_2 was monitored. The TPO experiments were carried out at room temperature or at mild temperatures up to 100 ºC. Afterward, the sample is exposed to argon for 30 minutes.

Then, the sample is exposed to 1% H_2/Ar up to the reduction temperature or until a H_2O peak or H_2 uptake is detected by the mass spectrometer. The TPO/TPR studies were conducted on SiO_2 supported Ru and Ni catalysts as shown in Figure B.2. After TPO to 100 ºC, the catalyst is exposed to TPR showing formation of water by hydrogen reaction of oxygen pre-covered catalyst. The maximum rate of reduction was around 170 ºC and is consistent with prior reports [196]. Consumption of H_2 at this temperature is attributed to the water formation from reduction of surface oxygen. The nickel catalyst exhibited a maximum reduction peak at 250 ºC. For this sample, the observed region H_2 uptake peak was broad, starting at ~ 200 ºC and continuing through 400 ºC.

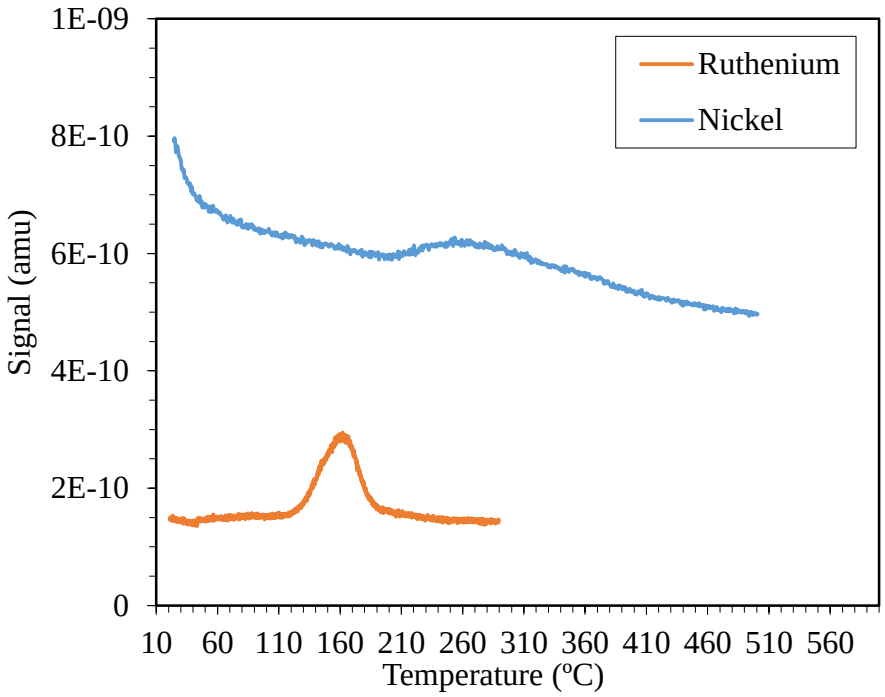

Figure B.2: TPR spectra for 1.6 wt% Ru, and 1.8 wt% Ni over SiO_2 (mass = 0.10 g) 1% H_2/Ar, total flow = 50 sccm, at 5 ºC /min.

B.3 METHANATION STUDIES OVER SiO_2-SUPPORTED RU AND NI

Methanation reaction experiments were conducted with 1.0% CO, 20% H_2, balance He mixtures with a total flow of 50 sccm at atmospheric pressure. The reaction conditions were the same as for the HDO of PAc, in order to allow comparison. Tables B.1 and B.2 summarize the conversion and selectivity for the methanation reactions.

Table B.1: Methanation over Ru/SiO_2. 1% CO, 20% H_2, balance Helium. Total flow = 50 sccm, 1 atm pressure.

Temperature	**Conversion**	Selectivity (%)				
(ºC)	**(%)**	**CO_2**	**CH_4**	**C_2H_4**	**C_2H_6**	**C_3H_6**
200	0.2	61.0	39.0	0.0	0.0	0.0
250	5.5	0.0	84.0	5.0	5.0	6.0

Table B.2: Methanation over Ni/SiO_2. 1% CO, 20% H_2, balance Helium. Total flow = 50 sccm, 1 atm pressure.

Temperature	**Conversion**	Selectivity (%)				
(ºC)	**(%)**	**CO_2**	**CH_4**	**C_2H_4**	**C_2H_6**	**C_3H_6**
200	0.0	0.0	0.0	0.0	0.0	0.0
250	1.2	0.0	100.0	0.0	0.0	0.0
300	9.5	17.0	83.0	0.0	0.0	0.0
350	18.0	12.0	88.0	0.0	0.0	0.0

APPENDIX C: SUPPLEMENTARY INFORMATION FOR CHAPTER 4

C.1 EXTERNAL/INTERNAL MASS TRANSPORT LIMITATIONS

The absence of mass transport limitations under the conditions in the current study was confirmed. The diagnostic test for determining whether internal mass transport limitations were significant involved measurements using different mesh sizes of the catalyst. As shown in Figure C.1, no change in the reaction rate for the different mesh sizes was observed for both Pd-2 and Pd-6, suggesting the absence of internal mass transfer limitations. These results are also consistent with previous calculations based on the Weisz-Prater criterion reported previously [146]. The absence of external mass transport limitations was confirmed by varying total flow rate (sccm) and measuring the reaction rate (Figure C.2). The minimum flow rate where no external mass transport limitations were detected was 200 sccm. Therefore, all experiments were conducted at 200 sccm to ensure working under the kinetic regime.

In addition to the above tests, the effect of metal loading on activity was compared for the 4 (Pd-2) and 2.6 wt% Pd/SiO_2 (Pd-3), since they have similar particle size of 2 and 2.1 nm, respectively. As expected, the TOFs for Pd-2 and Pd-3 were in close agreement (0.46 and 0.51 min^{-1}, respectively). This indicates that the specific activity per Pd surface atom is independent on the weight loading (%) of the metal, confirming once again the absence of external and internal mass transfer limitations.

For the cased of 5wt% Pd/C an external mass transport limitation experiment was conducted. By changing the flow rate from 50 to 200 sccm. Based on the results, figure C.3, no significant change in the reaction rate was detected in the range of flow rate. This suggest that the activity experiments were under the kinetic regime. No particle size (mesh size) experiments were conducted for 5wt% Pd/C.

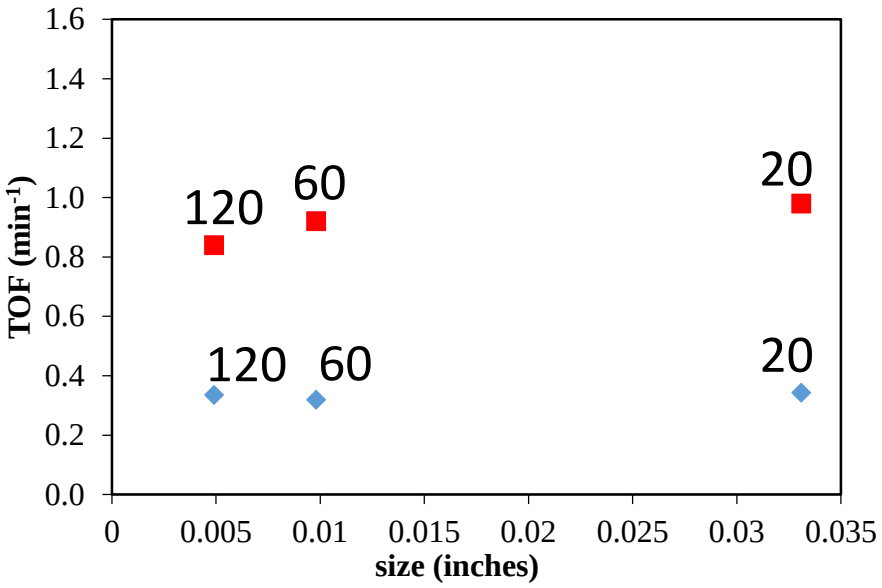

Figure C.1: TOF vs. different mesh sizes of 4wt% Pd/SiO_2 (♦ Pd-2) and 1.9wt% Pd/SiO_2 (■ Pd-6) for HDO of PAc at 200 ºC and 1 atm. ~1.0 % PAc, 20% H2/He, catalyst mass 200 mg , total flow 200 sccm, (20-120 mesh sizes).

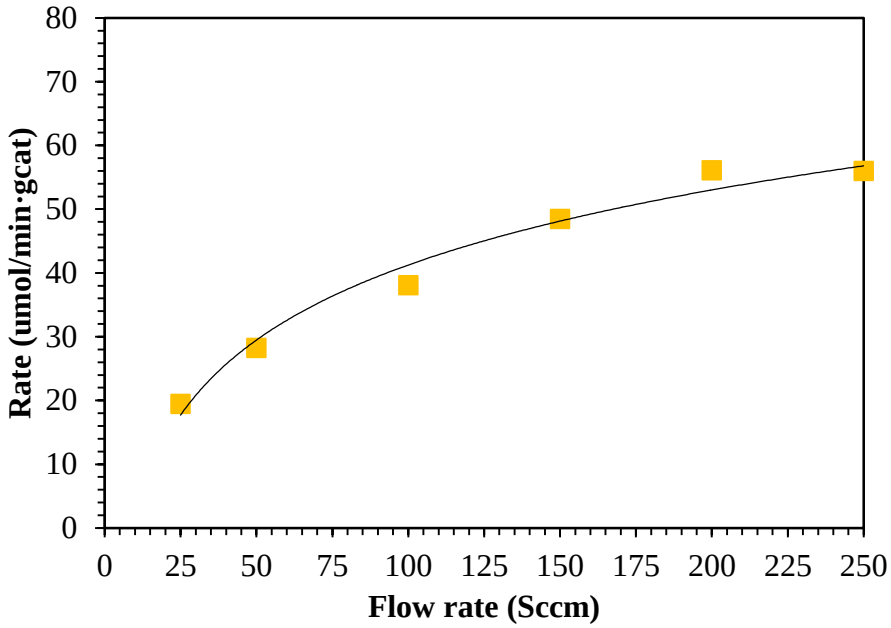

Figure C.2: Reaction rate vs. flow rate (sscm) for 4wt% Pd/SiO_2.

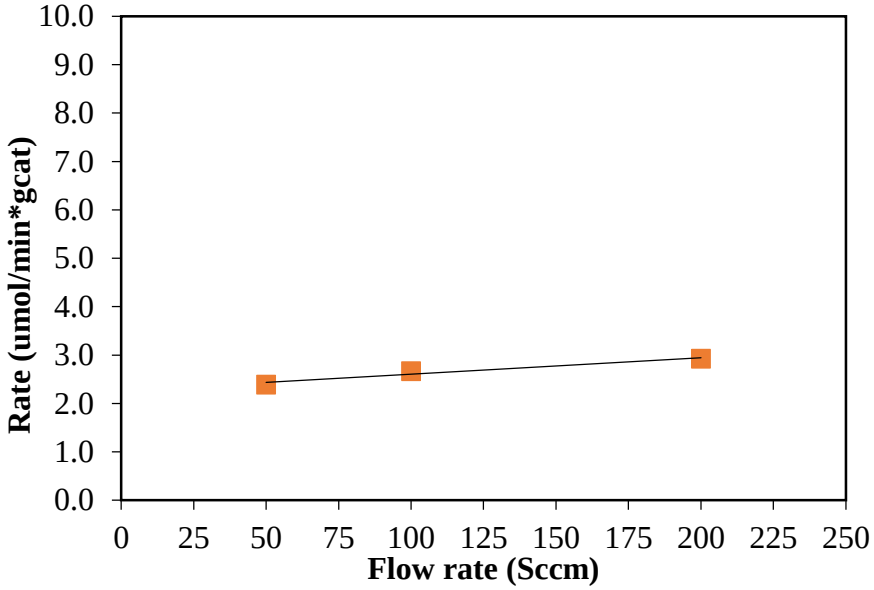

Figure C.3: Reaction rate vs. flow rate (sscm) for 5wt% Pd/C.

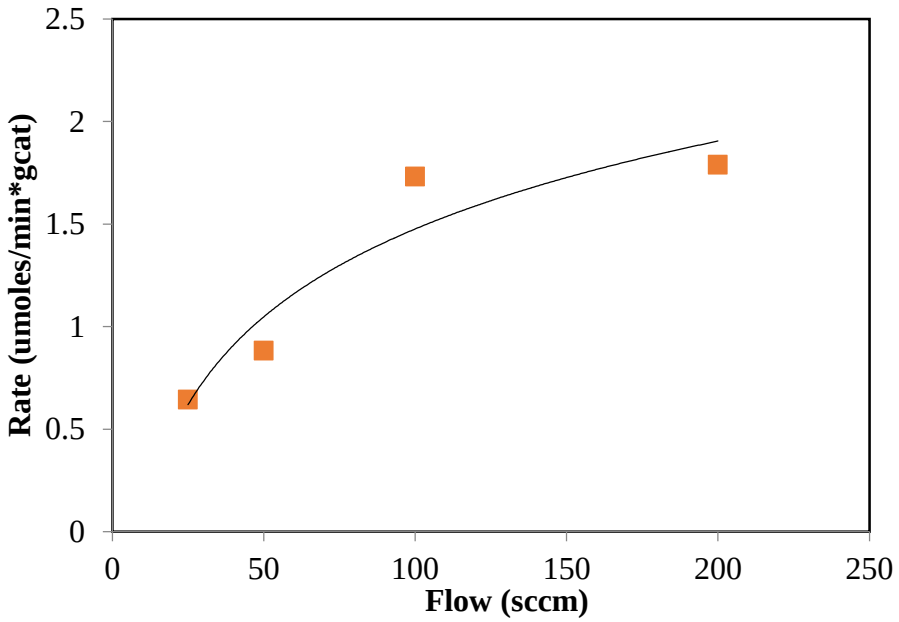

Figure C.4: Reaction rate vs. flow rate (sscm) for 2.3wt% Pd/TiO_2.

C.2 X-RAY DIFFRACTION

The X-ray diffraction (XRD) patterns were recorded using a Rigaku Ultima IV diffractometer system with a D/tex Ultra detector with Cu Kα radiation (λ = 1.54 Å). Data were collected from 10-80º 2θ with a step size of 0.04º and a scan rate of 1º/min. Particle size was estimated using the Scherrer equation with LaB6 (NIST SRM 660a) as a reference for instrumental broadening. The XRD particle sizes were estimated for Pd-2, Pd-6 and Pd-10 for both the fresh and spent catalyst by using the Scherrer equation which is defined as:

$$d = \frac{K\lambda}{\beta \cos(\theta)}$$

Where d is the particle diameter, λ is the wavelength of the incident radiation, θ is the Bragg angle, β is the full width at half maximum (FWHM) of the diffracted peak, and K is the shape factor of the particle which is designated to be 1.0 for spherical particles, but could have values as low as 0.73 for triangular shaped particles.

Figure C.4 shows the diffraction patterns for both fresh and spent Pd-2, Pd-6 and Pd-10. For each catalyst, three diffraction peaks were detected at 2θ = 40.1º, 46.7º, and 68.2º, which are indexed to the (111), (200), and (220) crystalline facets, respectively, of face-centered cubic (fcc) Pd according to the JCPDS card No. 05-0681 [197]. The broad peak at 2θ = 21º arises from the amorphous silica support. No significant peaks were detected for either the fresh or spent Pd-2 samples, indicating a particle size less than 2 nm and that there was no significant sintering. This is largely consistent with the chemisorption and STEM results. However, for Pd-6 and Pd-10, the particle sizes estimated by the Scherrer equation were 50-70% larger than the Sauter mean diameter estimated by STEM. The difference was even larger in the case of the chemisorption results for the Pd-6 samples. It should be noted that as the particle sizes increases, it is possible that the larger fraction of more sintered particles will result in narrower diffraction peaks, especially in a catalyst with very inhomogeneously distributed metal particles [198]. Indeed, discrepancy between chemsisorption, STEM and XRD have been observed by Punyawudho et al. [199] and Lambert et al. [141].

One of the reasons for these differences is also that XRD is a bulk technique that measures a volume-weighted mean diameter through the Scherrer equation [200]. In contrast, chemisorption is a surface-based approach and yields a surface-weighted mean diameter. In the case of STEM, to compare with chemisorption, the Sauter mean was used, $\overline{D}3,2 = \frac{\sum_i (Di^3)}{\sum_i (Di^2)}$ where Di is the diameter of the ith particle (Table C.1). However, for comparison with XRD, the de Broukere mean diameter $\overline{D}4,3 = \frac{\sum_i (Di^4)}{\sum_i (Di^3)}$ is a more appropriate

comparison. Table C.1 shows that the STEM-derived de Broukere mean compares very well with the XRD particle size based on the Scherrer equation.

Table C.1: Comparison of particle size Pd/SiO_2 over three different methods. b and a denotes before and after the reaction.

Catalyst Id.	Pd loading (wt%)	Sauter		de Brouckere	
		d_{pd} (nm) O_2-H_2 titr.	d_{Pd} (nm) TEM	d_{Pd} (nm) XRD	d_{Pd} (nm) TEM
Pd-2b	2.0	2.0	2.7	<2.0	2.2
Pd-2a		-	2.8	<2.0	2.7
Pd-6b	1.9	3.8	5.1	12.1	11.2
Pd-6a		-	8.0	12.9	13.8
Pd-10b	3.3	12.4	12.1	14.7	16.2
Pd-10a		-	13.4	18.9	20.5

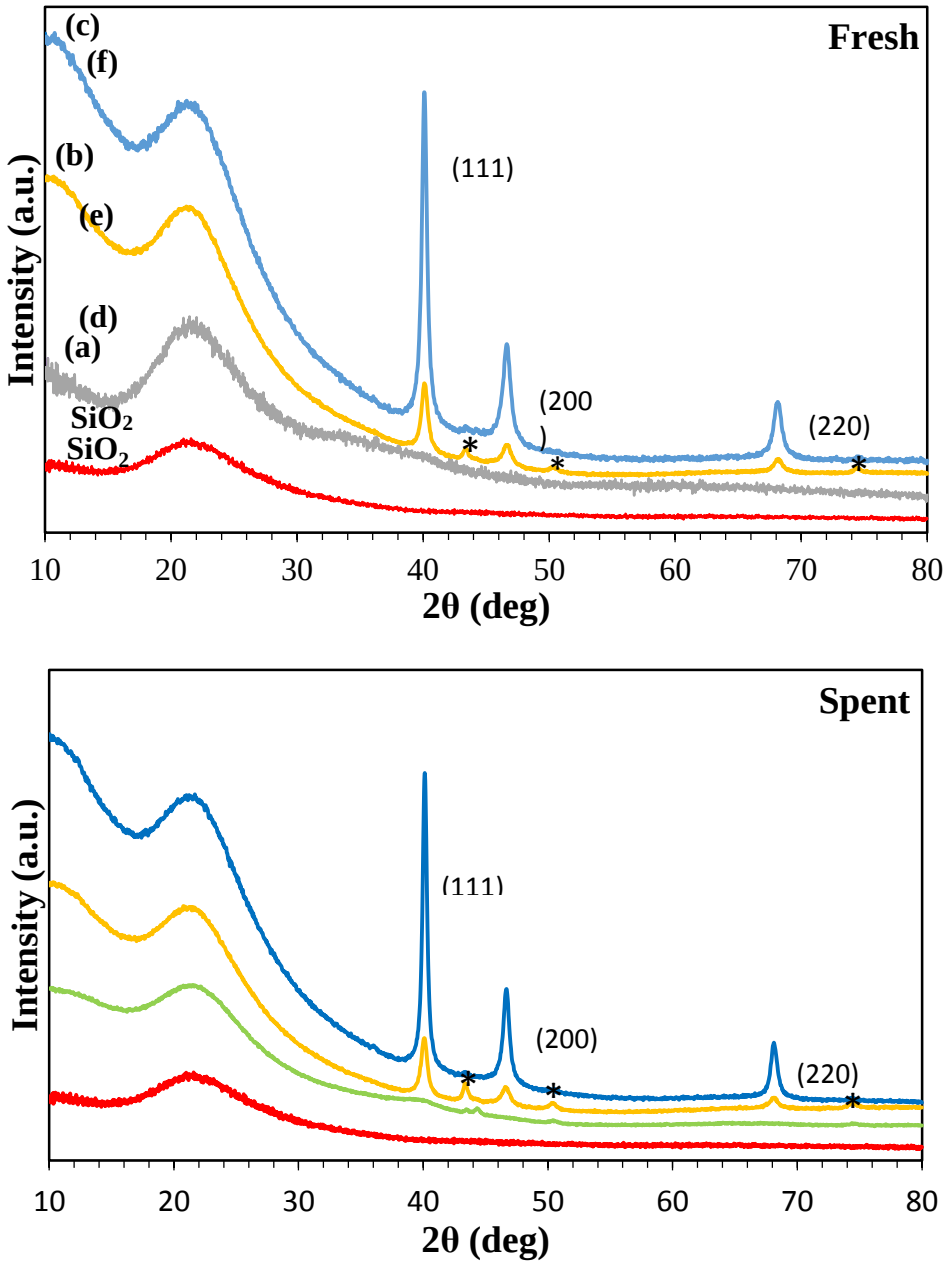

Figure C.4: X-ray diffraction pattern for Pd/SiO_2, before: Pd-2 (a), Pd-6 (b), Pd-10 (c), and after the reaction: Pd-2 (d), Pd-6 (e) and Pd-10 (f). * Steel slide (background holder).

APPENDIX D: SUPPLEMENTARY INFORMATION FOR CHAPTER 5

D.1. STANFORD RESEARCH SYSTEMS RGA100 MASS SPECTROMETER SPECIFICATIONS

The PAc products were diluted with argon carrier gas at approximately 35 ccm as measured by a digital flowmeter (ADM 2000, Agilent technologies). Sampling was done with a transfer capillary column of 25 micrometer i.d. (SGE) mounted onto the stainless steel (SS) stream tubing with a SS tee (Swagelok) and a reducing fitting with a bored Vespel-graphite ferrule (SGE). The other end of the capillary was mounted with VCR fittings and Vespel-graphite ferrule onto a vacuum chamber built with SS Conflat flange (CF250) parts (Duniway). The capillary was mounted at the top of the vacuum chamber in a cross configuration to provide accurate sampling with the gas analyzer to the left, the turbomolecular pumping station (Pfeiffer model TSH071E) beneath, and a Pirani/cold cathode full-range gauge (Pfeiffer model PKR251) to the right. The RGA used was a Stanford Research Systems RGA100 with an electron multiplier and accompanying software. The sampling rate was 3 sec for pressure vs. time measurements and the rate of intensity vs amu scans was 8 sec per 0-63 amu. Typical pressures in the chamber were 3-5 x 10^{-7} torr. Fragmentation patterns experiments for C_2H_6 were conducted to determine the relative intensities (see supporting information).

D.2. FRAGMENTATION PATTERN FOR C_2H_6

Figure D.1 shows the fragmentation pattern obtained by MS for proof and verification of the product distribution obtained by the labeled PAc experiment. The experimental conditions were carried out at 100% ethane in a total flow of 35 sccm. The total pressure was 4.5E-06 torr. The experimental data was compared with the theoretical fragmentation pattern obtained by the SRS library of the RGA software (table D.1). Additionally, the mass spectrum recorded for the HDO of labeled PAc is shown in figure D.2. Mass spectrum of 29, 30 and 31 are shown with the argon background as reference. The change in relative intensity (as compared to the background) can be seen for mass 29, 30 and 31 (fragmentation of CH_3CH_3 and CH_3CDH_2).

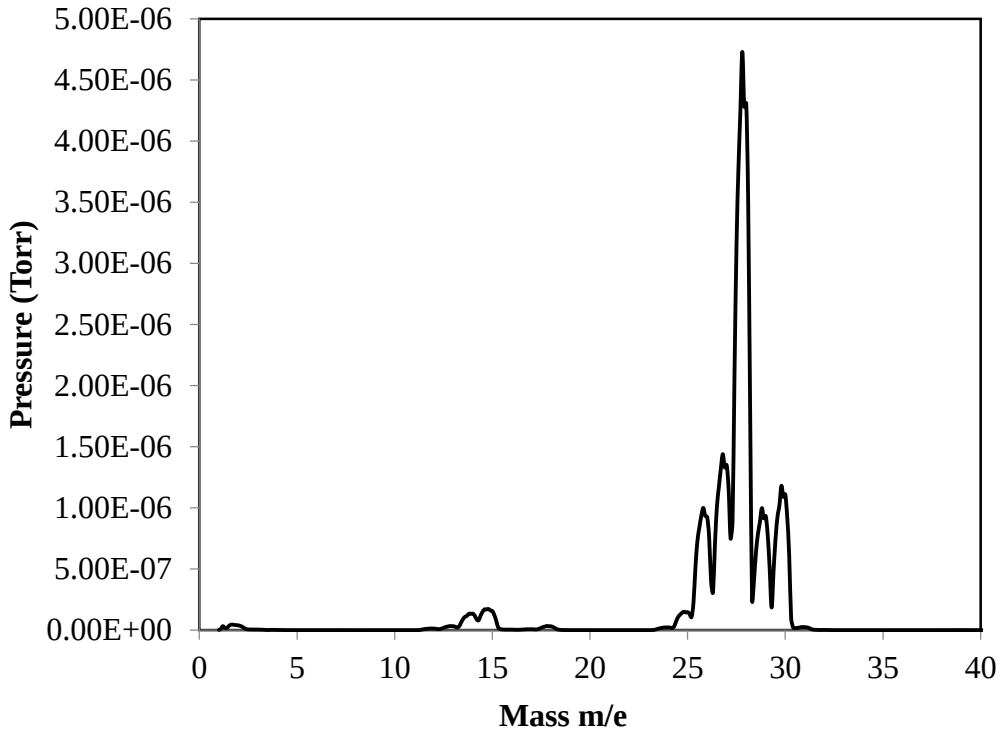

Figure D.1: Mass spectrometer for C_2H_6 rel. intensities

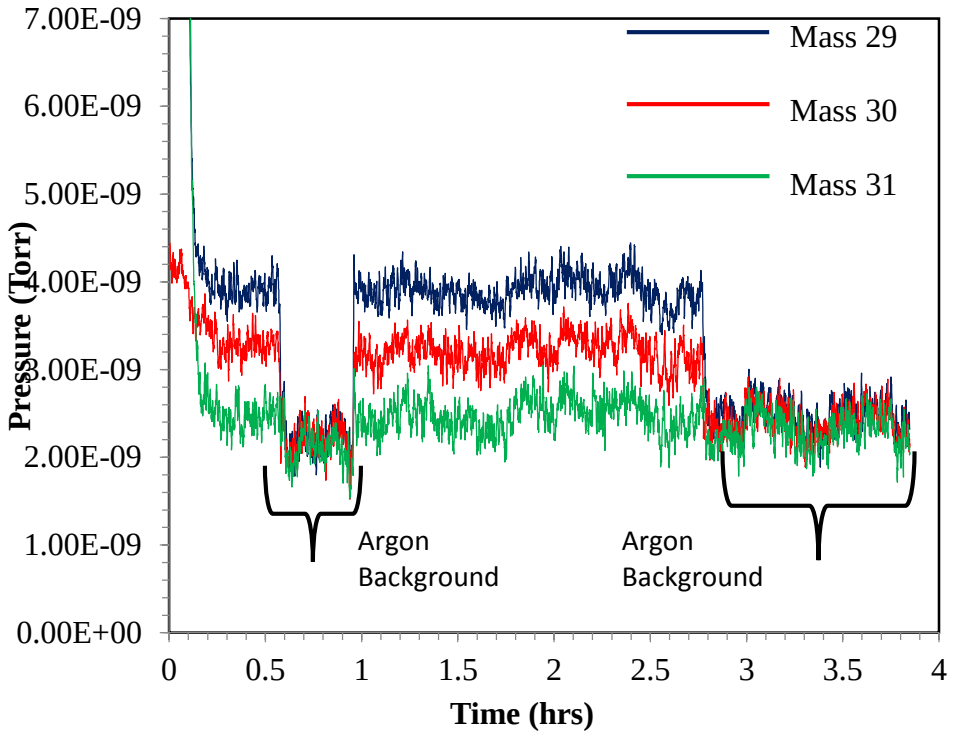

Figure D.2: Relative intensities for mass: 29,30 and 31 for the labeled PAc reaction. Using Argon as background. Ptotal = 4.0E-06.

Table D.1: Fragmentation pattern comparison between experimental and theoretical, taking as reference the published work from Amenominya and Pottier.

Peak	SRS Library	Experiment
	Theoretical %	Observed %
14	1.2	1.5
15	1.4	1.7
25	1.4	1.6
26	10.9	10.2
27	15.6	14.9

28	47.3	47.5
29	9.9	10.3
30	12.3	12.2

D.3. DESCRIPTION/ANALYSIS OF THE MASS SPECTRUM RECORDED FOR THE HDO OF LABELED PAC

The description below is to explain in detail table 5.3 from section 5.3.4. he experimental peak intensities for m/e = 29,30 and 31 are summarized in row 1. The calculated peak intensities for m/e = 29, 30 are determined using the unique m/e = 31 value of 3.51×10^{-10} as the reference peak for CH_3CH_2D. Thus, based on the published work m/e = 29, 30, and 31 fragmentation ratios obtained (row 3). Subtraction of the experimental intensities from the calculated values, gives the m/e = 29,30 values in Row 4, corresponding to a C_2 hydrocarbon product different from CH_3CH_3. If we assume that CH_3CD_2H is not formed as a C_2 product (CH_3CD_2H can only be formed if C-C bond breaking occurs to form a CH_3CD_2 fragment before H addition), then the only other C_2 product must be CH_3CH_3. The 29/30 ratio (Row 5) is calculated as 0.77, which is very close to the published value of 0.76 from Amenomiya (Row 6 that is consistent with CH_3CH_3 and CH_3CH_2D being the only C_2 products formed from the HDO of labeled PAc (CH_3CD_2COOH). Further corroboration is seen for the HDO of unlabeled PAc (CH_3CH_2COOH) in the two bottom rows. In this case the 29/30 ratio is 0.73, which is very near the values of 0.77 and 0.76 from the published work.

D.4 COMPUTATIONAL METHOD

All density functional theory calculations have been conducted with the Vienna Ab Initio Simulation Package (VASP).[201-203] The Kohn-Sham valence states are expanded in a plane wave basis sets with an energy cut-off of up to 400 eV. The interaction between core electrons is described with the projector-augmented wave (PAW)[203, 204] method. The exchange correlation energy is calculated within the generalized gradient approximation (GGA) using the functional form proposed by Perdew and Wang, which is known as Perdew-Wang 91 (PW91).[205-207] Similar pseudopotentials were used for hydrogen and deuterium atoms with only the mass modified for deuterium atoms.

The lattice constant obtained from the optimization of the fcc-Pd bulk is 3.953 $\AA$, which is in reasonable agreement with the experimental value of 3.891 $\AA$. The surface Brillouin zone is sampled with $4\times4\times2$ Monkhorst-pack k-point grid. Pd (111) is modeled by a 4-layer slab with a (3×4) surface unit cell and the palladium layers separated by a 15 $\AA$ vacuum. The bottom two layers were fixed to their bulk configuration during all calculations while the top two layers were free to relax in all directions. Adsorption energies of all intermediates were calculated at their most stable geometry by the following equation:

$$E_{ads} = E_{slab+adsorbate} - E_{slab} - E_{adsorbate}(g) \qquad (1)$$

where $E_{\text{slab+adsorbate}}$ is the total energy of the adsorbed intermediate on the Pd slab, E_{slab} is the total energy of the Pd slab and $E_{\text{adsorbate}}$(g) is the total energy of the adsorbate in the gas phase.

Transition states were obtained from our previous DFT studies[157-159] on PAc and finally, vibrational frequency calculations have been performed to obtain the frequency modes for all labeled intermediates and transition state structures.

The zero-point energy correction for all the structures was taken into account by using the following equation:

$$\Delta E_{ZPE} = \sum_i \frac{1}{2} h\nu_i \quad (2)$$

where h is the Plank constant and ν_i is the vibrational frequency of mode i.

D.4.1 MICROKINETIC MODELING

For surface reactions, the forward rate constant (k_{for}) of each reaction is calculated as:

$$k_{for} = \frac{k_B T}{h} \frac{q_{TS,vib}}{q_{IS,vib}} e^{\frac{-E_{a\_for}}{k_B T}} \quad (3)$$

where k_B is the Boltzmann constant, T denotes the reaction temperature, h is the Planck constant, E_{a_for} stands for the zero-point-energy-corrected activation barrier for the forward reaction derived from DFT calculations, and $q_{TS,vib}$ and $q_{IS,vib}$ are the (harmonic) vibrational partition functions for the transition state and the initial state, respectively, i.e., q_{vib} is calculated as:

$$q_{vib} = \prod_i \frac{1}{1 - e^{\frac{-h\nu_i}{k_B T}}} \quad (4)$$

where ν_i is the vibrational frequency of each vibrational mode of the adsorbed intermediate derived from our DFT calculations.

The reverse rate constant (k_{rev}) is calculated similarly and the thermodynamic equilibrium constant K is given by:

$$K = \frac{k_{for}}{k_{rev}} \quad (5)$$

For an adsorption reaction A(g)+*→A*, the equilibrium constant K is defined as:

$$K = \frac{(q_{vib})_{A^*}}{(q_{vib} q_{rot} q_{trans})_{A(g)}} e^{\frac{-\Delta E_{ads}}{k_B T}} \quad (6)$$

where $(q_{vib})_{A*}$ is the vibrational partition function of adsorbed A, and q_{vib}, q_{rot}, q_{trans} stand for vibrational, rotational, and translational partition functions, respectively. ΔE_{ads} represents the zero-point corrected adsorption energy, R is the ideal gas constant, and T denotes temperature.

For an adsorption reaction A(g)+*→A*, the forward rate is given by collision theory with a sticking probability of 1.

$$k_{for} = \frac{1}{N_0\sqrt{2\pi m_A k_B T}} \quad (7)$$

where N_0 is the number of sites per area (1.478×10^{19} m^{-2}) and m_A denotes the molecular weight of A.

The reverse rate constant is again given as:

$$k_{rev} = \frac{k_{for}}{K} \quad (8)$$

With the forward and reverse rate constants defined, we solve the full set of steady-state rate equations to obtain the surface coverage of all possible reaction intermediates and the fraction of free sites using the BzzMath library[208] developed by Buzzi-Ferraris. No assumptions were made regarding rate-limiting steps.

D.4.2 DFT AND MICROKINETIC MODELING STUDY

Our previous[157-159] study analyzed the elementary reaction steps involved in the DCN and DCX of PAc on Pd (111) from first principles. To computationally investigate the activity of labeled PAc, the adsorption and TS geometries obtained previously for unlabeled PAc[157-159] were used. DFT frequency calculations were performed for all intermediates involved in the HDO of labeled PAc to obtain the frequencies of the labeled intermediates needed to compute the zero-point energy corrections and vibrational partition functions of the labeled species. Figure D.3 shows the reaction network for the elementary

steps of the reaction. The calculated free energies of reaction (ΔG_{rxn}) and free energies of activation ($G^{\ddagger}$) for all the labeled elementary reactions, as well as the reaction parameters for the corresponding unlabeled reactions, are listed in Appendix _

Previously, it was found[157, 158] that the dehydrogenation of the α-carbon of PAc ($CH_3CH_2COOH^* + 2^* \rightarrow CH_3CHCOOH^{**} + H^*$) is one of the rate-controlling steps. At 200ºC, this step has a free energy of reaction, ΔG_{rxn}, of -0.02 eV and a free energy of activation of 0.70 eV. The correspondent labeled reaction, i.e., the de-deuteriation of the α-carbon of labeled PAc (Reaction 2: $CH_3CD_2COOH^* + 2^* \rightarrow CH_3CDCOOH^{**} + D^*$), has a free energy of reaction, ΔG_{rxn}, of -0.01 eV and a free energy of activation of 0.77 eV indicating that the overall turnover frequency (TOF) of labeled PAc will be slightly slower than that of unlabeled PAc as the barrier of this step was increased by nearly 0.1 eV.

To investigate the overall effects of changes in the reaction parameters on the TOFs, previously developed microkinetic models for the HDO of PAc over Pd (111) [47] were applied to labeled and unlabeled PAc under the reaction conditions identical to the above experimental study (Section 5.2.2). Accordingly, simulations were carried out at 200ºC and partial pressures of H_2 and PAc of 0.05 (5% H_2) and 0.01 (1% PAc) bar, respectively. The partial pressures of H_2O, CO_2 and CO were set to 10^{-3}; however, the analysis shows that the microkinetic modeling result is insensitive to the partial pressures of these intermediates in the range of 10^{-4} to 10^{-2} bar. In doing so, the partial pressures of these products are fixed, which is necessary since the model does not contain a reaction network for the water-gas shift reaction. Finally, the primary kinetic isotope effect, KIE = $\frac{TOF_{CH_3CH_2COOH}}{TOF_{CH_3CD_2COOH}}$ was calculated to be 1.49 under the experimental reaction conditions. This value is in very good agreement with our experimental result of 1.62 under the same

reaction conditions. Table 5.2 summarizes and compare the KIE obtained based on the computational, calculated and experimental approach.

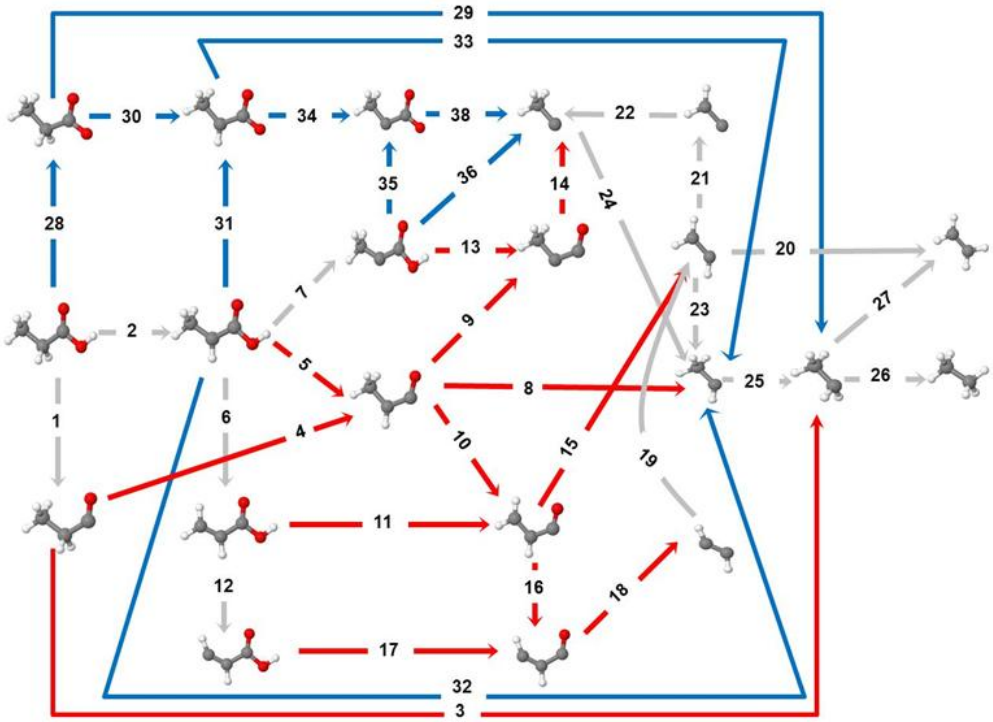

Figure D.3: Network of elementary reaction steps considered in the hydrodeoxygenation of PAc over Pd (111). Elementary reactions involved in the DCX mechanism are shown with blue color arrows, DCN reactions are illustrated with red color arrows, and those reactions involved in both mechanisms such as dehydrogenation reactions and removal of the hydrocarbon pool are shown with gray color arrows.

APPENDIX E: REACTOR DESIGN AND SET-UP

E.1. CONTINUOUS PLUG-FLOW REACTOR DESIGN AND SETUP

The gas-phase reactor located in 3B29 was designed and constructed with the supervision of Dr. John Monnier. The reactor followed a similar design as the one located in 3B21. The reactor main assembly consist of: A VLE system (100 mL) coupled with a chiller to maintain the temperature constant, 6 MFC (2 H_2, 2 He, 1 O_2, 1 C_3H_6-model 5850E) connected to a 5-channel Sierra power supply (± 15 VDC), one split-tube furnace (1 5/8" I.D x 6" O.D x 15" long) and a Valco switching valve box connected to a gas chromatography. The Valco switching valve include 6 ports (1/8"), 1 auto valve (standard electric actuator-110 VAC) and 2 manual valve. The GC system HP 5890 series II includes: dual detector FID and TCD, dual inlet split/splitless, PC preloaded with Chemstation software, flat screen monitor, keyboard, mouse and cables. Below is a description and pictures showing the valve actuator set-up:

Valco actuator model: E2L6UWE

- Position indication
- Manual or remote control
- 110 VAC or 230 VAC (two position also available in 24 VDC CE-certified version)
- No power demand on the chromatograph

The swtiching box in the load/inject mode can operate automatically by any data system with momentary contact closures or 5 VDC negative true logic outputs. A complete system, the actuator includes interface cable power cord, and manual controller assembly with position indication.

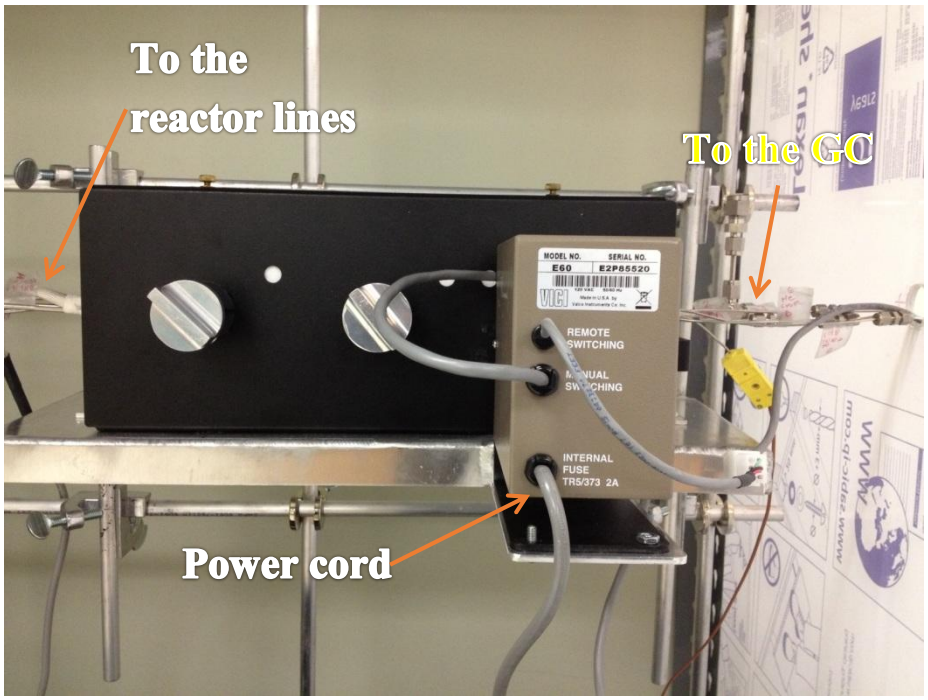

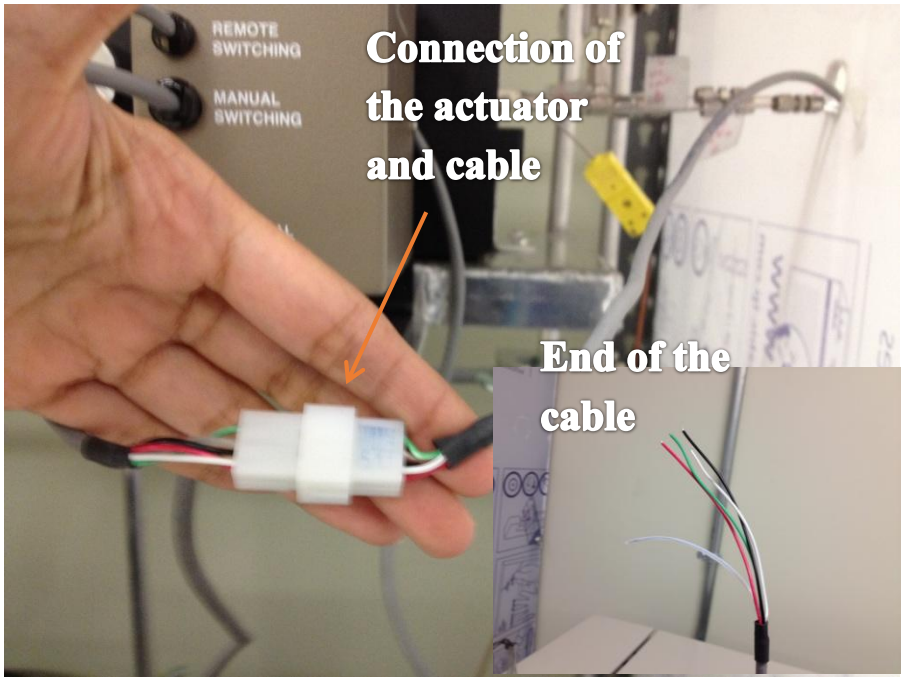

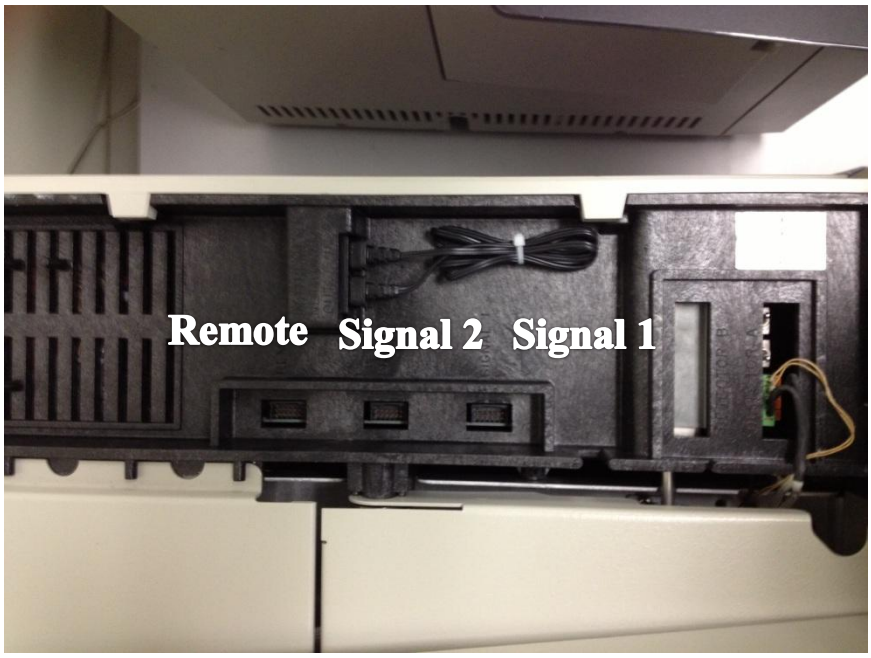

To control and operate the system's temperature, 4 temperature controllers where auto tuned: one for the inside of the valve box, one for the reactor furnace and two extras. The temperature controllers where operated by a 1/16" dual control outputs for pulsed 10 VDC at 20 mA with a relay SPDT 3A at 120/3A at 240 VAC. The reactor consist of a 3/8" SS tube with an 0.065" thickness (0.31" I.D). The catalyst sample was supported inside the reactor with a inner SS tube (~0.25" I.D). All the SS lines where heated up to 120ºC, and consist of 1/8" I.D. The SS lines connected from the valco box to the GC consist of 1/16" I.D.

The temperature controllers' box were constructed in the machine shop and followed the blueprint and picture indications bellow:

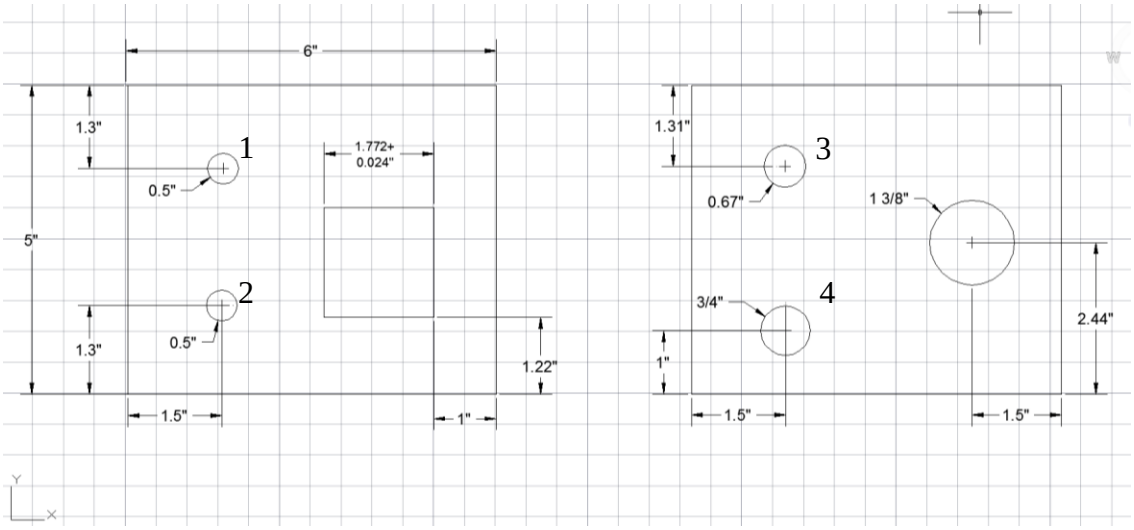

Figure E.1: blueprint of temperature controller box.

Drilled to clean pieces with diameter:

1. Fuse holder = 0.447”
2. Switch toggle SPST = 0.455”
3. Temp Connecto K = 0.601”
4. Power cable = ¾ to 0.8”

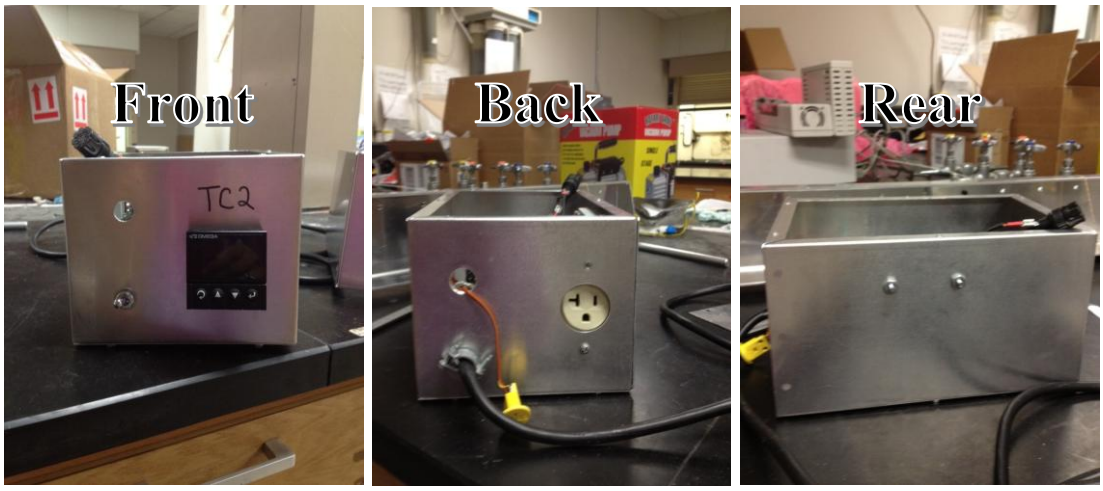

The hood and outside frame were designed similar to the reactor located at UOP lab. The metal frame for the hood consist of metal racks (78” x 72” x 30”). The inside

frame consist or vertical (4’) and horizontal (5’ 10”) rods connected to foot lab-frame and clamp holder talons. The side and slide doors are of 1/4" Clear Lexan from Sabic polymershapes. One panel for each side and 3 panels for the slide doors in the front. Figure E.2 shows an schematic of the enclosed hood. Table E.1 shows the cost for the equipment of the reactor system. All the SS fittings and valves were purchased from Swagelok.

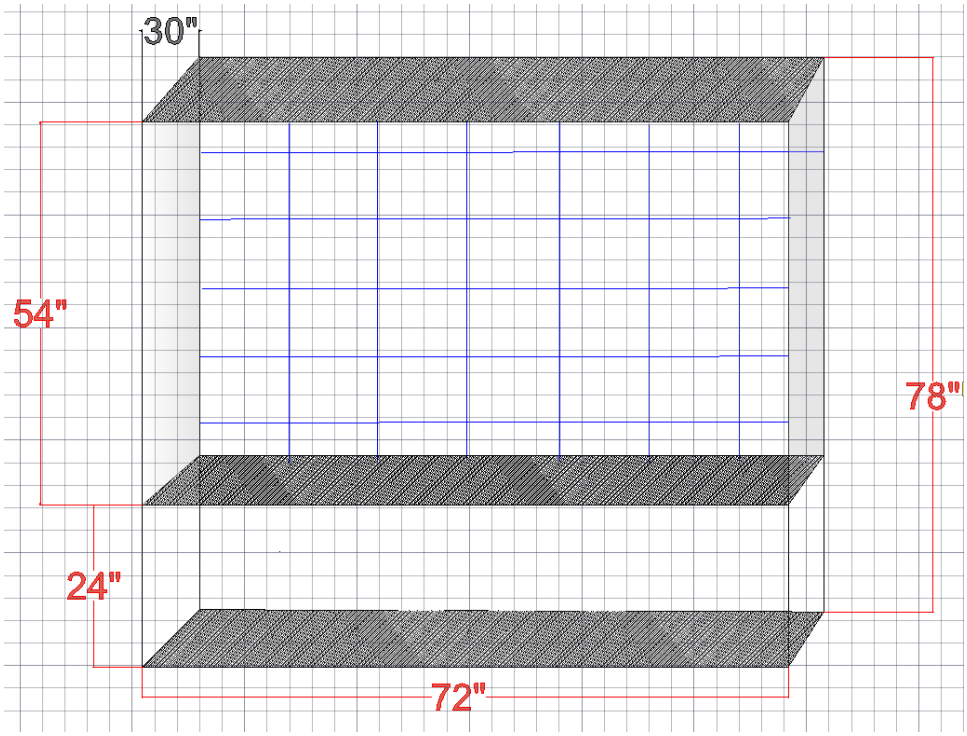

Figure E.2: Enclosed hood assembly

Table E.1: Cost of reactor's equipment

Equipment	Price $
GC (including ship&hand)	7300.0
temp controller	1704.2
temp controller design holes	105.0
furnace	2156.5
power supply	1330.0
MFC	4500.0
cables(6')	95.0
MFC rack	87.5
Plates for Valco box	175.0
valco switching box	2690.0
1/8" ferrule	20.0
1/16" ferrule	18.0
nuts, tees, reducer for Valve Box Swagelok	120.56
shelves	232.7
3/4" sanded wood (finished one side)	32.5
1/2" sanded wood	55.3
paint	15.2
screws, washers, nuts, receptacles, varnish	77.1
lexan glas	241.8
lexan glass for windows	330.0
aluminun rods	69.8

clamp holder Talon Jumbo	87.5
Lab Frame feet	167.7
elect tape and insulation cloth	24.7
nuts, screws, 5/16 screw,caulk, etc	36.6
hook connector	235.6
swagelok parts SS-ORS2	134.5
swagelok SS-600-R-4 and SS-401-PC	34.02
screws, for aluminum channel	32.7
parts for building hood+ exhaust fan	75.5
miscellaneous	36.6
aluminun channels 1/4"	116.2
Porous plot Q columns	1698.0
tubing (1/8"), ID 0.085"	400.0
tubing (1/16"), ID 0.040"	171.6
Chiller	Loaned
heating tape	569.5
Variacs	718.0
swagelok valves, Tee, reducer, nuts,ferrule	4432.6
wires, power	
20 amp circuit for GC	600.0
circuits broaded (325 amp, 4)	
Ventilation system	30.0
Total	30927.4

Assembly of 4 circuits to connect the GC and reactor system:

A) Each with 120 V
B) Each with 25 amp/circuit
C) Circuits have a twisted blade duplex
    1) Outside the hood
        a. 1 circuit, 2 duplex, one duplex with twisted blade and one duplex with normal blade
    2) Inside the hood
        a. 3 circuits each with 2 duplex, with twisted blade.

E.2 STANDARD OPERATION PROCEDURE

Chemical name/class:	**Propanoic Acid $C_3H_6O_2$/8 Hydrogen/2.1**	**CAS #:**	**79-09-4 1333-74-0**
PI:	**Dr. Christopher Williams**	**Date:**	**10/02/2012**
Building:	**Swearingen**	**Room #:**	**3B29**

1. **Circumstances of Use:**

0.1-1.0% Propanoic Acid, 20% hydrogen (UHP) balance Helium (~79.9-79.0%) is to be used for Hydrodeoxygenation of monometallic or bimetallic catalysts between transitional metals (i.e. Pd, Ru, Pt and Re) at temperature (200-400°C) inside an airtight stainless steel tube.

2. **Potential Hazards:**

Propanoic Acid is corrosive/irritant (health-3), Hydrogen is highly flammable

3. **Engineering Controls:**

- Brooks mass flow controllers (6), normally closed, coupled with Sierra power supply, bipolar, and connected to Swagelok 3-way valve and pressure gauge.
- Exhaust gases are released through a vent line (stainless steel) directed to the fume hood with adequate ventilation.
- An exhaust fan connected to an elephant trunk (directed to the fume hood) is placed at top of the hood in case of accidental leaks.
- Controlling gas release ranges from 10-100 SCCM Max using regulators and mass flow controllers.
- Temperature controllers are connected to the furnace, heating tape and Valco switching valves (see figure). The furnace will operate between 200-400 ºC (max. temp 500ºC); the Valco switching box will be maintained at 100ºC. The heating tape utilized for the lines that connect the switching box to the gas chromatograph will be maintained at 100ºC.
- Variable Autotransformer 120V 10amp hydrogen cell vibratory (Variac) will be connected to the heating tapes to:
    - Heat the lines that go from the Vapor/liquid equilibrium saturator (VLE) to the reactor and switching box.
    - Heat the lines that connect the exit of the switching box to the reactor and outlet of reactor back to the switching box.
    - The lines will be maintained at < 150ºC, by controlling the Variac voltage up to ~60V.
- Pressure gauge (3) will be connected to measure the pressure in the VLE, the entrance of the reactor and the loop capacity pressure (inside the switching box).

- The pressure is mainly atmospheric and is used to record the pressure drop, which might be generated in the catalyst bed.

- The VLE is connected to a water bath that operates at temperature ranging from 0-70ºC (the water bath/refrigerator is filled with ethylene-glycol).
- In case of blackout, the MFC will be normally closed and will not deliver any gases, the temperature controllers will stop operation and will not heat again unless it is started over.
- The furnace and the GC will cease operation, and an uninterruptable power supply is not required.
- When the power gets back, the system will not continue and the operator is responsible of resuming the work.

4. **Normal operating procedure:**

- The VLE (usually capacity of 500 mL), is filled (1/2 of the volume) with Propanoic acid (PAc). The water bath is kept at 40ºC.
- Helium gas (~20 sccm) flows into the VLE, where specific amount in PAc is swept to the vapor phase by vapor/liquid equilibrium thermodynamics.
- Specific concentration of hydrogen and diluent helium (~30 sccm), is mixed with the sweep helium (containing PAc), before the reactor inlet.
- The reaction is carried out in a plug-flow stainless steel (1/4") reactor, where the catalyst bed is maintained at the center coupled with a thermocouple to monitor the catalyst's bed temperature.

- The product and the feed (reactant) are analyzed by a GC, HP 5890 series II, coupled with a FID and TCD detector and Split/splitless injection port.
- The valve switching box controls and directs the flow, depending on what type of analysis (feed/product) and in what detector will be analyzed.
- The effluent gases go directly to vent.

5. **Work Practice Controls:**

- The gas cylinders will be placed close to the walls chained into a 2 X 4 piece of wood (screwed to the wall).
- All fittings will be checked before starting each experiment for any possible leaks.
- The power supply should be operational before opening the valve of the MFC.
- The reactor should be pressurized to check for any leaks, prior starting the experiments.
- The temperature of the lines and the valve switching box should be monitored regularly.
- Carrier helium should be flowing through the GC columns at all times; therefore, the helium tank pressure should be checked constantly.
- All the experiments will be carried out in an enclosed hood, with the appropriate ventilation system.

6. **Personal protective equipment (PPE):**

Standard lab gloves when operating the furnace at room temperature.

Heat resistant gloves to handle the furnace at high temperature during experiment.

Use of standard safety glasses and lab coats.

7. **Transportation and Storage:**

- Gas cylinders are securely fastened in the wall close to the reactor.
- When empty, cylinder valve will be properly tightened / closed and Airgas staffs will be notified to pick up.
- The empty hydrogen tank will be place on the flammable gases enclosure (located at the basement outside of Swearingen building).

8. **Waste Disposal:**

Propanoic acid waste is disposed in the proper container located in 3B19.

9. **Exposures/Unintended contact:**

- Eye contact: Check for and remove any contact lenses. Immediately flush eyes with plenty of water for at least 15 minutes, occasionally lifting the upper and lower eyelids. Get medical attention immediately.
- Skin Contact: Immediately flush skin with plenty of water for at least 15 minutes while removing contaminated clothing and shoes. To avoid the risk of static discharges and gas ignition, soak contaminated clothing thoroughly with water before removing it. Wash clothing before reuse. Clean shoes thoroughly before reuse. Get medical attention immediately.

- Inhalation: Call medical doctor or poison control center immediately. Move exposed person to fresh air. If not breathing, if breathing is irregular or if respiratory arrest occurs, provide artificial respiration or oxygen by trained personnel. Loosen tight clothing such as a collar, tie, belt or waistband.

10. **Emergency/Release Procedure:**

- Remove all persons from the contaminated area.
- Call USC police at 7-4215 if needed.
- Contact EHS for further assistance.

11. **Training of personnel:**

All personnel are required to complete the General Lab Safety class offered by EHS. In-house, hazard-specific and procedure-specific training on this particular setup is required for any person who will perform this procedure.